

Syracuse University

SURFACE

Dissertations - ALL

SURFACE

May 2019

TOWARDS PROBING THE STRONG FIELD GRAVITY USING BINARY BLACK-HOLE RINGDOWNS

Swetha Bhagwat
Syracuse University

Follow this and additional works at: <https://surface.syr.edu/etd>



Part of the [Physical Sciences and Mathematics Commons](#)

Recommended Citation

Bhagwat, Swetha, "TOWARDS PROBING THE STRONG FIELD GRAVITY USING BINARY BLACK-HOLE RINGDOWNS" (2019). *Dissertations - ALL*. 1049.

<https://surface.syr.edu/etd/1049>

This Dissertation is brought to you for free and open access by the SURFACE at SURFACE. It has been accepted for inclusion in Dissertations - ALL by an authorized administrator of SURFACE. For more information, please contact surface@syr.edu.

ABSTRACT

In this thesis, we study black hole ringdowns as a probe to understand the strong-field classical gravity. When two black holes merge, they form a single distorted black hole that then radiates gravitational waves and settles into a final stable Kerr state. The signal produced during this process is called the ringdown and can be modelled as perturbations on the space-time of the final Kerr black hole. Ringdowns contain information about the strong field dynamics close to the black holes and thus, can be used to test our understanding of gravity. There are three specific questions that we explore in this thesis: First, at what point after the merger of two black holes can one use a perturbative description to model the space-time? This tells where in the gravitational wave signal of a binary black hole merger can one start a ringdown-based test. Second, how likely are we to realistically find a signal that allows us to perform a ringdown-based test given the current and future gravitational wave observatories. And finally we discuss, how should the data analysis be carried out in order to extract information from the ringdown of an observed GW signal?

**TOWARDS PROBING THE STRONG FIELD
GRAVITY USING BINARY BLACK-HOLE
RINGDOWNS**

By

Swetha Bhagwat

B.S-M.S, Indian Institute of Science Education and Research (IISER), Pune

DISSERTATION

SUBMITTED IN PARTIAL FULFILLMENT OF THE REQUIREMENTS

FOR THE DEGREE OF

DOCTOR OF PHILOSOPHY IN PHYSICS

Syracuse University

May 2019

Copyright © Swetha Bhagwat 2019

All rights reserved.

ACKNOWLEDGEMENTS

First and foremost, I would like to thank my advisor, Prof. Duncan Brown, whose constant support and guidance has played a vital part throughout my PhD studies. I would truly like to thank Prof. Stefan Ballmer for the many insightful conversations that helped me understand numerous concepts in Physics. I am also very grateful to Prof Josh Goldberg for spending the time to help me understand various aspect of spacetime geometry that I was grappling with at different places in my projects. I am grateful to the members of sugwg group - Laura, Larne, Soumi, Ben, Prayush, Chris, Steven, Daniel, Fabian, Eric and David for their company and for helping me out at various points in my studies. Their help and support were crucial for my PhD studies.

I would next like to thank Suraj Shankar, for not only being a very supportive friend (and being a very cheerful company during all the adventures and misadventures we had!) but also for constantly impressing me about how well connected different branches of physics are and for talking frequently about overviews of problems in different branches of physics. Some of these conversations have been very refreshing and stimulating. I also want to thank Francesco, Gizem and Cem for many beautiful moments we shared. I am very grateful to Raghav, Nouman, Arvind, Jerome, Fabian and Preeti for their company and for the many enjoyable and enlightening discussions on various topics and also for being there for me at different points during my PhD. The five years I spent in Syracuse has been very enjoyable because of you guys. Cheers to all the games nights, tea evenings, cemetery walks, snow ball fights, Broadway and landmark theater shows, long drives (thanks Beasty), spic Macay concerts, movie nights, long discussions over coffees at Kubal and countless dinners we had together. It was a true pleasure sharing my PhD time with you all and I am looking forward to continue hearing from you. Cheers!

As peculiar as it sounds, I very greatly admired the beautiful fall and winter of Syracuse; seeing seasons change was greatly inspiring for me. I would particularly thank Gizem for being a very sportive company to take long walks in beautiful but fierce snow storms. Special

thanks to all of you for accompanying me in the many trips to the lakes, waterfalls and the state parks and helping me explore the beautiful nature of upstate New York. I will absolutely treasure it. I should also acknowledge ‘my dear swing’ and ‘my tree’ where I spent hours each time I had to think about how to proceed in my projects.

This acknowledgement will be incomplete without thanking Masha, who has been my collaborate as well as a good friend. Working on the ‘Kerness’ project with her was a lot of fun despite getting stuck so many times. I would also like to thank Prof Mark Scheel, Prof Saul Teukolsky, Prof. Geoffery Lovelace and Prof. Badri Krishnan for guiding me at various points. I would also like to thank my master’s thesis advisors Prof. Sanjeev Dhurandhar and Prof. Sanjit Mitra for having me visit Iucaa every year for all of the five years during my PhD and for giving me constructive advice thought out.

Last but probably the most important, I would like to thank my parents and my brother for always being there for me whenever I needed them. Thank you very much for always understanding me and being supportive of every decision I take. I would also like to thank Amruta and Payal for giving me their unconditional friendship and support through all these years.

Contents

List of Tables	xi
List of Figures	xxiv
1 Introduction	1
1.1 Overview	1
1.2 On the discovery of GW150914	4
1.3 On ringdown and scales of perturbation	4
1.4 On choosing the start time of binary black hole ringdown	5
1.5 On spectroscopic analysis of stellar mass black-hole mergers	5
1.6 On the detectability of the subdominant mode in a binary black hole ringdown	6
2 On the discovery of GW150914	8
2.1 An overview on the search and the best-fit template	8
2.2 On the detection of GW150914	9
2.3 Direct comparison of the data and best fit template	11
2.4 Parameters of GW150914 inferred using SEOBNRv3 waveform family	16
3 On ringdown and the scales of perturbation	19
3.1 The binary black hole ringdowns and the quasi-normal-modes	19
3.2 Ringdown as a probe for strong field gravity	20
3.3 Intuition on scales of perturbation and start time of ringdown	21
3.3.1 Model 1: Two point masses	21
3.3.2 Model 2: Final black hole as a rotating tri-axial ellipsoid	23
3.3.3 On the scales of perturbation in a GW150914-like ringdown using our toy models	24

4	On choosing the start time of binary black hole ringdown	28
4.1	Introduction	28
4.2	Theory	30
4.2.1	Characterizing strong-field Kerrness	30
4.2.2	Connecting strong-field information to \mathcal{S}^+	36
4.2.3	Inferring perturbation amplitudes via Kerrness	41
4.2.4	Outline of method	45
4.2.5	Measuring Kerrness on the horizon	45
4.3	Numerical implementation	46
4.3.1	Description of simulation	46
4.3.2	Implementation of Kerrness measures	47
4.3.3	Map from source to \mathcal{S}^+ - implementation	49
4.4	Results	54
4.4.1	Horizon behavior and multipolar analysis on BBH ringdown	54
4.4.2	Measuring and mapping Kerrness onto the waveform	56
4.4.3	Estimating and mapping the perturbation amplitude onto the waveform	66
4.4.4	Implication of the start time on data analysis	72
4.4.5	Comparison with GW150914 testing GR chapter	77
4.5	Conclusion	79
5	On spectroscopic analysis of stellar mass black-hole mergers	82
5.1	Introduction	82
5.2	Methods	84
5.3	Results and Implications	91
5.4	Conclusion	93
6	On detectability of the subdominant mode in a binary black hole ringdown	98
6.1	Introduction	98
6.2	Theory	100
6.2.1	Parameter Estimation	100
6.3	Methods	101
6.3.1	The Ringdown Injections	101
6.3.2	Details on Parameter Estimation	103
6.4	Results	104
6.5	Discussions and Implications	111

7 Conclusion	113
A On KERR-NUT spacetime	116
A.1 Kerr-NUT parameters	116
Bibliography	136

List of Tables

1	The parameters of the best-fit-template for GW150914 trigger reported by the PyCBC search pipeline obtained by analyzing the data containing GW150914 trigger. These values are used in our study presented in section 2.3	11
2	The time at which SNR timeseries peaks in each of the detector. The detector data is match filtered against a single time-domain template constructed using SEOBNRv2 waveform family. The template corresponds to a BBH system with the parameters set to the best-fit-template parameters reported by the PyCBC search.	13
3	The parameters of GW150914 estimated by the LIGO collaboration using the fully precessing EOB templates. This table contains the first two columns presented in Table 1 of [1]. In this Table the median value of each of the parameters is quoted along with the 90% credible intervals.	18
4	The shift in the time axis performed to align the news functions extracted from different radii in Fig. 10. The alignment has been done such that the overlap between the news function extracted from different worldtube radii with the extraction from $R = 128 M$ is maximized.	53
5	The spread in the time for given % of the peak value of Kerrness measures computed using all the measures. The combined % time refers to the value of the dashed lines in Fig. 19 and corresponds to the time at which all the measures have at least decayed to the indicated % relative to the time at which the peak amplitude of news function occurs.	62

6	Summary of our results. The first column counts the number of cycles from the peak of the news function. The second column presents the drop in SNR with start time chosen in the data analysis. SNR is normalized to have 100% when the data analysis starts at the peak of the waveform ($h(t)$) i.e., at $3839 M$. The third column shows the concomitant percentage decrease in the Kernness measures from the peak value (similar to Fig. 19). Further, in the last column we present the perturbation amplitude inferred by the crossing times computed with Type D 1 and D 2 measures (similar to middle panel of Fig. 23.)	75
7	The above table shows the results we obtain from a Monte-Carlo simulation of 10^6 stellar mass binary black-hole mergers uniformly distributed in component mass, orientation and in volume defined by a sphere of radius 1500 Mpc. We categorize each event into one of the set defined below and tabulate the fraction of signals that fall into each set. Set 1: $l = m = 2$ mode could not be detected, Set 2: $l = m = 2$ could be detected but no other sub-dominant mode could be detected, Set 3: $l = m = 3$ sub-dominant mode can be measured, Set 4: $l = m = 4$ sub-dominant mode can be measured, Set 5: Both $l = m = 3$ and $l = m = 4$ sub-dominant modes can be measured, Set 6: failed measurability of sub-dominant mode due to resolvability criterion.	95
8	The above table has information similar to Table 1 but with sets defined differently. Here, Set 1: $l = m = 2$ mode could not be detected, Set 2: $l = m = 2$ could be detected but $l = 2, m = 1$ sub-dominant mode could be detected, Set 3: $l = 2, m = 1$ sub-dominant mode is both detected and resolved, Set 4: $l = 2, m = 1$ sub-dominant mode is detected but not resolved . Here again, we tabulate the number of events out of 10^6 Monte-Carlo simulated binary black-hole mergers that fall in each of these sets.	95
9	Using our results in Table 1 and the optimistic (pessimistic) rates of binary black-hole mergers, predicted based on the recent discoveries of binary black-hole mergers [2], at $240 \text{ Gpc}^{-3} \text{ yr}^{-1}$ ($13 \text{ Gpc}^{-3} \text{ yr}^{-1}$), we present the rate of events that would allow measurability of $l = m = 3$ or $l = m = 4$ sub-dominant mode with current and future ground-based detectors. We present this combined ($l = m = 3$ or $l = m = 4$) rate, because de-tuning the detector around the frequency band $300 - 500 \text{ Hz}$ for a ringdown oriented search benefits both of these modes.	96

10	Using our results in Table 2 and the optimistic (pessimistic) rate of binary black-hole mergers, predicted based on the recent discoveries of binary black-hole mergers [2], at $240 \text{ Gpc}^{-3} \text{ yr}^{-1}$ ($13 \text{ Gpc}^{-3} \text{ yr}^{-1}$), we present the rate of events that would allow measurability of single sub-dominant modes.	97
11	The list of prior used to perform two mode RD PE. In this Table, we list the choice of priors used in our study. Note that these priors are non-informative in the sense that we do not favour any particular configuration. However, the bounds of the parameter space contain some information in itself. Further, the prior on A_{22} is set to be log-uniform and not uniform to ensure a better sampling of the smaller amplitudes.	104
12	Testing the presence of the second mode. From looking at the posterior plots present in Figures 34, 35, 36 and 37, we infer the cases in which we can detect the presence of the second mode.	104

List of Figures

1	Direct comparison of the detector data with the best fit template. The data from the H1 and L1 have been minimally filtered and appropriately shifted to align with each other. The best-fit template corresponding to each of the detector timeseries is overlaid on the data. The inlay panels display the details of the filters used to condition the data. We see that with very minimal data conditioning, the data from the two detectors as well as the template aligns well, validating the presence of an astrophysical signal.	14
2	Figure 1 from GW150914 detection paper [3] . This Figure is taken from the GW150915 detection paper [3] by the LIGO collaboration. The top two panels of this Figure displays a more refined version of the plot we produce in our preliminary study presented in Figure 1. The bottom panel is a frequency-time plot, revealing a clear chirping in the data signal.	15
3	r_{eff} marked on the GW strain. This plot presents the GW waveform corresponding to the best-fit template parameters reported by the PyCBC search pipeline for the event GW150914. The solid waveform is the + polarization and the dotted one is the \times polarization of the GW strain $h(t)$. The waveform is zoomed-in on the last few cycles. The lines indicate to the value of r_{eff} at different times of the evolution. The dotted lines correspond to separation vector before merger of the BBH system and the solid line correspond to un-physical separation, that provide the scale of perturbation during the merger-ringdown phase of the BBH evelotion. We use the units where $G = c = 1$	26

4	The distortion parameter δ as a function of time. This plot depicts the evolution of the distortion parameter δ defined in Equation 3.20. The scale of the perturbation is comparable to the intrinsic scale of the system roughly when $\delta = 1$. We see that about 0.005 sec after the peak of the waveform, the value of $\delta \sim 1$. Note that by convention used in the waveform family the merger is set at $t = 0$ (see Figure 3). We assert that any perturbative analysis should start later than this time.	27
5	The set of conditions for a slice to be locally isometric to Kerr. The nodes refer to the resulting type of spacetime when the conditions on each edge, given by their name and equation in the text, are met. For example, a spacetime must meet all four of the conditions specified in the edge from Algebraically Special to Petrov Type D to belong to the type D subset of algebraically special spacetimes. In numerical applications, the failure of these Kerrness conditions to be met gives a set of respective Kerrness measures, where larger measures denote greater deviation from Kerr. For each measure, we give N_d , the number of numerical derivatives beyond the first derivatives of the metric needed to evaluate it, which corresponds to the numerical noise level in the measure, with higher derivative powers giving more numerical noise.	31
6	Prescription for connecting the strong-field information to the asymptotic frame dynamics. The colored cylinder represents the region of spacetime that is evolved by the Cauchy code. The vertical green line within the cylinder indicates the direction of coordinate time. The horizontal lines represent time slices. The details of the location of time slices depend on the gauge choice. The pink boundary of the cylinder depicts the worldtube from where the CCE is performed. The purple lines with unit slope illustrate the null characteristics along which the information on the worldtube is propagated to (the solid blue line) \mathcal{I}^+ . In our procedure of associating information in the source frame with the asymptotic frame, we identify all the points along a characteristic by an equivalence. The solid green line in the cylinder acts as a source to the waveform feature at τ_0 observed at \mathcal{I}^+	37

7	Envelope function from Eq. (4.21), for two choices of width and falloff parameters, $\{W, F\}$. We show how the envelope parameters affect an extraction radius of $R = 5M$ (marked by the dashed black line). For our chosen values of $\{W = 6M, F = 8\}$, the envelope is at ~ 1 and $R = 5M$, while for $\{W = 3M, F = 8\}$, the envelope affects the perturbation amplitude at $R = 5M$. We have checked that using a smaller envelope does not change the qualitative behavior of our results.	41
8	Behavior of absolute Kerrness measures with perturbation amplitude ε . We compute this on an $l = m = 2$ QNM perturbed Kerr BH with the same mass and spin as the final remnant in the BBH simulation we consider in this chapter. We average each measure on a coordinate 2-sphere of $R = 5M$. Note that we do not plot Type D 4 due to the high level of numerical noise in the measure, but it behaves similarly to Type D 3. The behavior is initially quadratic with ε for all measures. At larger amplitudes $\varepsilon \geq 5 \times 10^{-3}$, Type D 2, D 3, D 4 and Kerr 1 show higher-power dependence, and hence non-linearity. We show this $\varepsilon_{\text{crit}} \sim 5 \times 10^{-3}$ by a dashed vertical line. The lines between the points are only used to visually connect them (rather than being fits).	42
9	Convergence of Kerrness measures on a numerical BH in Kerr-Schild coordinates with dimensionless spin $\chi = (0.2, 0.3, 0.4)$. We observe exponential convergence towards the theoretical value of zero with numerical resolution. For each measure ζ , we present $\ \zeta\ /\ \zeta_0\ $, the L2 norm over the spatial slice normalized by the L2 norm of the lowest resolution. The resolution is expressed $\sqrt[3]{N}$, where N is the number of spectral collocation points in the domain.	48

- 10 The $l = m = 2$ mode of the news function seen at \mathcal{S}^+ extracted from worldtube boundaries of $R = 5M, 32M, 64M, 80M, 96M$ and $128M$. The horizontal axis corresponds to the time stamps associated with the news function corresponding to CCE from $R = 128M$. The **top panel** shows the real part and the **bottom panel** shows the imaginary part of the news function. The alignment of news functions has been done such that the overlap is maximized. The transformation that changes the gauge from a non-inertial to an inertial observer has not been applied to any of the extractions. All of the extractions beginning with $R = 32M$ seem to agree with one another (to the point of overlapping with the $R = 128M$ line). Notice that the amplitude of the news function extracted from $R = 5M$ deviates from the other extractions, especially in the first cycle. Nevertheless, the phase evolution between the news function from extraction radii seem to agree. The primary goal of this figure is to compare the extracted waveforms at $R = 5M$ and $R = 128M$. Thus we have bolded and boxed these lines. 50
- 11 The phase discrepancy between the news function extracted from a worldtube radius of $R = 5M$ and $R = 128M$. The news functions are aligned to maximize the overlap. The **top panel** presents the phase evolution of the news function for each extraction radius. The **bottom panel** shows the fractional difference defined as $\phi_{128} - \phi_5$. Notice that the phase difference is significant at the very beginning but quickly decreases to an acceptable level for our analysis. We notice that the phase difference oscillates about 1 radian, indicating the level of error we introduce by - a) not performing the final gauge transformation, b) imposing no-ingoing condition for CCE. 51

- 12 Settling of the post-merger AH as a function of coordinate time. The **top panel** shows the areal mass quickly attaining a constant value and the minimum and maximum radii R of the horizon exponentially settling to final values. Each quantity ζ is presented as $|\zeta - \zeta_{\text{final}}|/\zeta_{\text{final}}$ where ζ_{final} is the value at the final time of the simulation. The **bottom panel** shows the behavior of the initially excited AH mass multipoles, labeled by the l_{eff} given in Eq. (4.24) at the final time. The initially excited quadrupole moments ($l_{\text{eff}} \sim 2$) are shown by the dashed lines, while the initially excited hexadecupole moments ($l_{\text{eff}} \sim 4$) are shown by the solid lines. As discussed in the text, two of the quadrupole moments and four of the hexadecupole moments, as well as the $l \sim 1$ and $l \sim 3$ moments immediately vanish due to symmetry. Thus, we do not plot them in this figure. The excited multipoles either exponentially decay or reach constant values consistent with the values expected for Kerr [4]. 55
- 13 Behavior of absolute Kerrness measures with coordinate time on BBH post-merger spacetime. The measures are averaged on a variety of concentric nested coordinate 2-spheres of radii R around the BH, as indicated by the colors. Larger values *within each subplot* mean that the 2-sphere is farther from being locally isometric to Kerr. For measures that involve higher-order numerical derivatives, we present the results only at radii where they are at least somewhat well resolved. All plots, however, include $R = 5M$, the radius we use to map Kerrness onto the waveform. Type D 4 is particularly noisy, as it contains the highest number of numerical derivatives. The measures exponentially decay as the spacetime approaches Kerr, ultimately reaching a numerical noise floor. We observe that the peak of each measure moves outwards with radius, indicating propagation of non-Kerrness. 57

14	Absolute Kerrness measures on slices of the BBH post-merger spacetime. The data is presented in the equatorial plane, with the gray region corresponding to the excised BH. The black circles correspond to coordinate radii $R = 5 M$ and $R = 10 M$. The columns correspond to Speciality Index, Type D 1, and Kerr 1, and the rows (from top to bottom) correspond to coordinate times at which the each measure at $R = 5 M$ achieves 100%, 30%, 10%, and 1% of the combined peak value. The quadrupolar pattern (with $ m = 2$) in all three measures is consistent with the dominant quadrupolar radiation (recall that these are absolute measures, and hence do not distinguish between positive and negative values). Notice that the algebraic measures—Speciality Index and Type D 1—settle outward-in, whereas Kerr 1, a geometric measure, settles inward-out. Additionally, the structures in the measures are visible even at 1% of the peak value. We can compare these measures to Ψ_4 (in Figs. 21) to infer their sensitivity to the spacetime curvature features.	59
15	Kerr 2 measure throughout the post-merger BBH simulation, averaged on a variety of coordinate 2-spheres of radius R . The values remain relatively constant and low, indicating that no NUT charge is gained during ringdown.	60
16	Exponential convergence of the noise floor of each Kerrness measure on the final timestep of the BBH simulation. Each measure ζ is presented as an average over a 2-sphere of $R = 5 M$ (where the measures have settled to a noise floor), normalized by $ \zeta_0 $, the average of the lowest resolution. The resolution is indicated by $\sqrt[3]{N}$, where N is the number of spectral collocation points. The convergence to zero shows that the noise floor observed in Fig. 13 is a numerical noise floor, rather than real a physical artifact. We have also testing this convergence behavior on a 2-sphere $R = 5 M$ and verified that the behavior is consistent (although more noisy).	61

- 17 Connecting the Kerrness measures in the strong-field to dynamics at \mathcal{S}^+ using the procedure described in Sec. 4.3.3 on the BBH post-merger. The **left panels** map the algebraic measures and the **right panels** map the geometric measures on to the news function. The **top panel** within each subplot corresponds to a Kerrness measure in the strong-field, while the **bottom panel** shows the news function at \mathcal{S}^+ . The purpose of plotting the news function directly below each Kerrness measure is to emphasize that the top and bottom panels are mapped to the same time axis. The dashed lines of different colors indicate the % decrease from the peak value of the respective Kerrness measures. The horizontal axis corresponds to the simulation coordinate time induced on the news function extracted from a world tube radius of $R = 128 M$. Furthermore, unlike the strong-field result plots that aim at rigorous characterization of isometry to Kerr, here we aim at providing insight into validating the start time of ringdown for data analysis. Therefore, these plots are on linear scale as opposed to logarithmic scale. Notice that the curves on the left panel decay more slowly than those on the right; Type D 1 is the slowest to decay, closely followed by Type D 2. Also, recall that we cannot compare the magnitude of the top part of each of these panels as they are dimensionally different. . . . 63
- 18 This figure is similar to Fig. 17 but for Speciality Index. We plot this separately as it is an independent measure and decays rapidly compared to the other measures. Further, we do not indicate the 1% of peak line because of numerical noise (cf. Fig. 13) which leads to unreliable root finding for time of percentage decrease. 64
- 19 The concomitant decrease of all of our Kerrness measures. The dashed lines indicate the time at which all the measures decay to at least the indicated % of peak. The bands color the region in which different measures decrease to the indicated % of peak. Notice that there is about half a cycle spread in each of these bands. Therefore, the dashed lines provide a conservative idea of the validity of the choice of the start time for data analysis. We have specifically included the spread of these bands as a quantifier of error bounds in the statements of validity made further in this chapter. Furthermore, one could shrink the right boundary of these shaded bands if one combines the Kerrness measures with appropriate weights based on their sensitivity to the spacetime curvature and the final remnant's effective potential. 65

- 20 Ψ_4 in the equatorial plane for both a single BH with an $l = m = 2$ perturbation of amplitude $\varepsilon = 7.5 \times 10^{-3}$ and $\varepsilon = 10^{-3}$ (**left panel**), and for the BBH ringdown (**right panel**) at times that achieve the same Kerrness as (**left panel**). For all cases, Kerrness is matched on a coordinate 2-sphere of $R = 5 M$. The two black circles correspond to coordinate radii $R = 5 M$ and $R = 8 M$. The Gaussian envelope of width $R = 8 M$, as described in Fig. 7, can be seen in the plots for the single BH cases. Note that this is only meant to show qualitative agreement between Ψ_4 on both slices, as the quantity is still subject to coordinate tetrad effects in the strong-field region. Notice that although the two systems look similar, allowing us to infer the BBH simulation perturbation amplitude, the mapping does have some imperfections. 67
- 21 Ψ_4 in on the x-axis (in the equatorial plane) for both a single BH with an $l = m = 2$ perturbation of amplitude $\varepsilon = 7.5 \times 10^{-3}$ (**top panel**) and $\varepsilon = 10^{-3}$ (**bottom panel**), and for the BBH ringdown at times that achieve the same Kerrness. For all cases, Kerrness is matched on a coordinate 2-sphere of $R = 5 M$. The x-axis of the plot shows the radius, and includes the data within the Gaussian envelope of width $R = 8 M$, as described in Fig. 7. Note that this is only meant to show qualitative agreement between Ψ_4 on both slices, as the quantity is still subject to coordinate tetrad effects in the strong-field region. Notice that although the two systems look similar, the mapping does have some imperfections. Recall, however, that it is ultimately the invariant Kerrness measures that determine the mapping between the perturbation amplitude and the BBH merger-ringdown time. 68

22	Comparison of the Kerrness measures during the BBH post-merger to the values of the Kerrness measures on an $l = m = 2$ QNM perturbed Kerr BH of various perturbation amplitudes ε , with the same mass and spin parameters. The measures are averaged on a 2-sphere of coordinate radius $R = 5 M$, which corresponds to comparable areal radii of $\sim 2.59 M$ in both systems. The measures evaluated on the BBH slices are shown by solid black lines, decaying as a function of time. The Kerrness measures for the perturbed metric are presented as horizontal dashed red lines, one for each ε . The times at which the BBH curves intersect the Kerrness values for a given ε Kerr perturbation give a scale for the BBH Kerrness measures as the post-merger progresses. These times, known as <i>crossing times</i> are then mapped onto the waveform, and used to validate the start time of ringdown. Note that the measures have different crossing times. The time axes are shifted to agree with the timestamps of the GW at $R = 128 M$, as explained in Table 4.	69
23	Mapping the inferred perturbation amplitude close to the BH onto the news function. The top panel shows the spread in the crossing times computed using just the Speciality Index, the middle panel uses only the algebraic measures and the bottom panel utilizes only the geometric measures. Notice that amplitudes larger than 2×10^{-3} do cross the post-merger timeslices when computed using the geometric measures and that the crossing time spreads in them are relatively large, suggesting a difference in the symmetry of a perturbed Kerr metric and the post-merger BBH spacetime. However, this does not seem to be reflected when we just consider the algebraic measures as they have a relatively small spread in the crossing time. The spread in the crossing time of the Speciality Index is equal to the sampling rate.	71
24	Comparison between the strain h calculated using CCE and RWZ methods. All waveforms are presented in terms of the $l = m = 2$ mode. We use the fact that the strain is the integral of the news function to cross-check the methods. The top panel shows the CCE news function \mathcal{N}_{CCE} compared to \dot{h}_{RWZ} , the derivative of the RWZ strain. The bottom panel shows h_{CCE} , the integral of the CCE news function, compared to the RWZ strain h_{RWZ} . We find good agreement until late times, when h_{CCE} begins to drift, likely due to the numerical integration scheme used.	73

25	The top panel of this figure shows the percentage decrease of SNR from the peak value. The % SNR is set to 100 at t_{merger} . For this plot, we evaluate Eq. (4.29) with varying lower bounds for the integration. The dashed horizontal lines correspond to $\{80, 60, 40, 20\}$ % SNR. On the same plot, we mark the perturbation amplitude bands for a direct comparison between perturbation amplitude and statistical error. Notice that by the time the perturbation amplitude near the BH decreases by an order of magnitude, there is only a few percent of SNR left in the signal, emphasizing the sharp trade-off between the systematic biases arising from modeling the post-merger as perturbed Kerr and the statistical uncertainty arising due to exponentially decay of signal amplitude. The bottom panel shows the total energy radiated in units of M during the merger-ringdown. This is calculated by integrating Eq. (4.31). Again, we have plotted the concomitant percentage decrease of the Kerrness measures from their peak values for an easy comparison between the statistical and systematic errors associated with the choice of the start time of ringdown. In particular, the constant settling in the total radiated energy occurs between the time when the Kerrness measures have decayed to 5 – 1% of their peak values, implying that at these times the GW is very weak in amplitude. . . .	74
26	Spread in estimation of dominant mode frequency as a function of SNR. We present the spread, σ_f in the estimation of frequency calculated using Fisher information matrix formalism. We should the increase in spread with decreasing SNR, providing the rough intuition on the implication of Fig. 25 on parameter estimation.	75

27	Comparison of the times chosen in the testing GR study of GW150914 [5]. Here, we make statements about their validity to perform tests that rely on the perturbative nature of the BH. Specifically, we propose that a plot of this nature be done for future detections, especially if the SNR is high, to gain an insight into the inferred strong-field perturbation amplitudes corresponding to different choices of ringdown start time. The dotted line in the top panel shows different choices of start time for performing tests on the detector data. The bottom panel shows what each time choice corresponds to in the simulation gauge. Although a practical choice of start time to perform tests like no-hair theorem tests should be decided based on the interplay between the statistical and systematic uncertainty, a plot of this nature gives significant understanding of the results of such tests. For instance, in the case of GW150914, had the signal been much louder than what we observed, this plot suggests that we <i>could</i> get biased results due to large inferred perturbation amplitude in the strong-field leading to errors in modeling the post-merger as a perturbed BH at 3 ms.	78
28	The following are sensitivity models for each detector [6] we consider in our study. The aLIGO curve corresponds to the design sensitivity of Advanced LIGO and the A+ curve to the proposed upgrade to the Advanced LIGO detectors. The Cosmic Explorer (CE) and the Einstein Telescope (ET) are two of the proposed next generation ground-based detectors. We also perform the analysis with a flat noise curve at a strain per $\sqrt[2]{\text{Hz}}$ of 10^{-25} , to infer some conclusions which are independent of the shape of the noise curve. The shaded region shows the frequency band that corresponds to optimal tuning of the detectors for ringdown searches.	86
29	This figure presents the magnitude of mode amplitudes $\ A\ $ predicted by the fitting formulae given in [7] as a function of dimensionless symmetric-mass-ratio η . Comparing the amplitudes of different modes, we infer that the potential candidates for sub-dominant mode measurability correspond to $l = m = 3$, $l = 2, m = 1$ and $l = m = 4$	87

30	We show the dimensionless central frequency of QNMs as a function of symmetric-mass-ratio η as predicted by [8]. Note that modes with different l have central frequencies that are well separated. One could naively expect that resolving modes with the same l could be challenging. However, for stellar mass black-hole mergers this is not the case.	88
31	These contour plots show the differences in the central frequencies of the sub-dominant modes: $l = 2, m = 1$, $l = m = 3$ and $l = m = 4$, with the dominant mode. The color bar presents a measure of frequency difference in Hz. Notice that the central frequency of the $l = m = 3$ and $l = m = 4$ sub-dominant mode differs from the dominant mode by hundreds of Hz. It would be right to assume that resolvability of these modes is not challenging. However, it is very interesting to note that even for the $l = 2, m = 1$ sub-dominant mode the central frequency is separated by at least 20 Hz from the central frequency of the dominant mode. This is consistent with the fact that our results indicate that resolvability is not a limiting factor.	89
32	Scatter plots of all points that allow for measurability of sub-dominant modes in our analysis using a flat detector sensitivity curve at a strain of $10^{-25} \sqrt[2]{\text{Hz}}^{-1}$. The x and y axes of these plots correspond to the central frequencies of $l = m = 2$ and the measurable sub-dominant modes in Hz respectively. From these plots, we can infer that if one were to perform detector de-tuning optimized towards a spectroscopic analysis of stellar mass black-holes, a frequency band around 300 Hz to 500 Hz would be the best choice for narrow banding.	91
33	This figure presents the magnitude of mode amplitudes $ A $ predicted by the fitting formulae given in [7] as a function of dimensionless symmetric-mass-ratio η . This figure is taken from [62]	102
34	This is a null result test. Above are the posterior plots for the recovery of mode amplitude ratio and phase of the subdominant mode. The injected waveform has ringdown corresponding to only the dominant mode but it is recovered by a template family that has two modes of ringdown. The top panel corresponds to an injection of an optimal injected SNR = 15, the top right to SNR = 20, the bottom left to SNR = 25 and that in bottom right to SNR = 30.	105

35	Above are the posterior plots for the recovery of mode amplitude ratio and phase of the subdominant mode. The mode amplitude ratio of the injection is 0.1 and the phase of the subdominant mode is 1. The top panel corresponds to an injection of an optimal injected SNR = 15, the top right to SNR = 20, the bottom left to SNR = 25 and that in bottom right to SNR = 30.	106
36	Above are the posterior plots for the recovery of mode amplitude ratio and phase of the subdominant mode. The mode amplitude ratio of the injection is 0.2 and the phase of the subdominant mode is 1. The top panel corresponds to an injection of an optimal injected SNR = 15, the top right to SNR = 20, the bottom left to SNR = 25 and that in bottom right to SNR = 30.	107
37	Above are the posterior plots for the recovery of mode amplitude ratio and phase of the subdominant mode. The mode amplitude ratio of the injection is 0.3 and the phase of the subdominant mode is 1. The top panel corresponds to an injection of SNR = 15, the top right to SNR = 20, the bottom left . . .	108
38	Mode amplitude ration of 0.1 at an SNR of 40. In this figure, we show the result of parameter estimation when the optimal SNR of ringdown injection with amplitude ratio of 0.1 is increased to 40. Panel on the left shows the posterior recovered and can be compared with Figure 35. Panel on the right compares the normalized histogram for amplitude ratio for $A_R = 0$ (single mode) and $A_R = 0.1$ and can be compred to Figure 39. In this case we see that the second mode can be infered.	109
39	Marginalized posteriors for amplitude ratio for all the injection in this study. The panels corresponds to normalized histogram for amplitude ratio for ring-down injections corresponding to an optimal SNR = {15, 20, 25, 30} from top to bottom. In each of these panels, the black histogram corresponds to the null case, where the injected signal has only one mode. The green, blue and red histogram correspondes to an injection with amplitude ratio of 0.1, 0.2 and 0.3 respectively. When the colored histograms (corresponding to a non-zero amplitude ratio) seperate clearly from the black histogram (corresponding to single mode injection), one can claim the detection of the second mode. . .	110

Dedicated to my parents, Satyavati Bhagwat and Prabhat Bhagwat

Chapter 1

Introduction

1.1 Overview

Many challenges of 21st-century physics revolve around our understanding of the nature of gravity. Some of the major open research problems include: the quantization of gravity [9, 10, 11, 12], the black hole (BH) information paradox [13, 14, 15, 16, 17], building a unified theory that describes all the fundamental forces [18], the fine-tuning problem in cosmology [19, 20] and understanding the nature of the dark energy [21]. The general theory of relativity (GR) which describes the classical behaviour of gravitation [22], has an elegant theoretical structure and has been tested experimentally in various regimes [23]. Nevertheless, our current understanding of gravity seems to be in conflict with the framework of quantum mechanics [24, 25, 26] and reconciling the two theories in a consistent framework has been very challenging. Developing a quantum theory of gravity remains an important puzzle that is crucial to our understanding of fundamental physics. Additionally, the fine-tuning problem in cosmology suggests that our understanding of gravity might be incomplete at the large scales. With this understanding that GR might be a good description of gravity only up to certain scales (and that it might need both UV and IR corrections), alternative descriptions of gravity are being developed that aim to resolve one or more of these inconsistencies [23, 27, 28, 29]. Experimental and observational tests of GR and other alternative theories of gravity are needed to understand the nature of gravity at different scales [30, 31, 32, 33].

Metric theories of gravity predict propagating disturbances in the space-time curvature known as the gravitational waves (GW) [34]. The details of the GW produced by a disturbance depends on the exact underlying theory of gravity [23]. For instance, if there is an IR modification to GR, one could witness a change in propagation of GW from a high redshift source, while if there were additional degrees of freedom in the theory, one could see

propagation in scalar and vector sectors as well. Depending on the details of the underlying theory the morphology of the GW emitted changes. Thus, a measurement of GW can help eliminate or constrain families of alternative theories of gravity and test the validity of GR [35, 36].

The advent of GW astronomy offers an unprecedented method of testing GR and probing the nature of gravity in different regimes [34]. Two GW signals from binary black hole (BBH) mergers (named GW150914 and GW151226) were observed by the Laser Interferometer Gravitational-wave detectors (LIGO) in its first observing run with a statistical significance greater than 5σ [37]. In the second observing run, a binary neutron star (BNS) event (named GW170817) and three more BBH events (named GW170608, GW170814 and GW170104) were observed [38, 39, 40, 41]. With these observations, tests have been performed to understand the underlying theory of gravity; GR was seen to be consistent with all the observed GW signals [5]. Although the possibility of an alternative description of gravity could not be excluded, these observations placed rigorous constraints on many families of alternative theories of gravity [42, 5, 43]. With the upgrades to the current LIGO facilities [44] and the future ground-based missions like the Cosmic Explorer [6] and the Einstein Telescope [45], complemented by the proposed space-based projects like the LISA [46], our ability to probe the nature of gravity will improve significantly.

GW emitted during a BBH coalescence can be roughly divided into three parts [47]. Each of these parts contains imprints of gravitational dynamics at different length scales and spacetime curvatures, therefore, testing different regimes of gravity. In the first phase, called the ‘inspiral’, the GW emitted has an increasing frequency and amplitude (referred to as the GW chirp). In this phase, the two BH are far apart (compared to the size of the BH horizons) and are slowly orbiting (compared to the speed of light, c) the common centre of mass. One can use an analytical series expansion in $\frac{v}{c}$, called the ‘post-Newtonian (PN) approximations’ to compute the GW emitted during the inspiral phase. This approximation assumes the limit $\frac{v}{c} \ll 1$. This part of the signal can be used to study the accumulated effects of the small differences in the dynamics predicted by GR. This phase is followed by a ‘plunge-merger’ phase where $\frac{v}{c}$ grows to become comparable to 1 and the PN approximation breaks down. It contains imprints of the rich nonlinear-strong field dynamics. In this stage, the two BHs merge and form a single distorted BH. The third part of the signal is called the ‘ringdown’ (RD). During the RD, the newly formed BH settles down to its final stable configuration. This phase can be described in the framework of analytical BH perturbation theory. The GW radiated during this phase is a superposition of the characteristic modes

of the final BH, called the ‘quasi-normal-modes’ (QNM). The plunge-merger and the RD signals contain imprints of dynamics in the strong field gravity and probe a length scale of the order of the BH horizon size.

The GW signal from a BBH event offers some powerful tests of GR. In particular, using the inspiral signal in a parameterized-post-Newtonian (PPN) scheme [c.f chapter 4 of [48]], one can experimentally constrain violations of many fundamental features of GR. Some of the features that one can test using this framework are the following: the amount of spatial curvature given a central mass, the time delay effects, the lorentz dispersion, diffeomorphism symmetry of GR, the principle of equivalence and the conservation laws associated with the global symmetries [48]. Similarly, the merger-RD part of a CBC GW signal can be used to perform tests of GR in the strong field and, to explore nature of the compact objects [49, 50, 51, 52, 53]. These tests probe a region of spacetime with high curvature¹. The tests that can be performed using this part of the signal include the no-hair theorem test [54, 55], the BH area increase test [56, 57], direct observation of BH QNM spectrum [58] and the absence (or presence) of echoes in post-merger signal [59, 60]. These tests are invaluable as they let us probe gravity in regimes that are inaccessible to most other experiments.

Some of the important tests using the RD rely on the BH perturbation theory. For instance to perform tests to validate the no-hair theorem and the area increase law, one needs to measure at least two QNM modes present in the RD. Unfortunately, the GW150914 signal has an SNR ~ 8 in the RD. The uncertainty in the measurement of the frequency of the dominant RD mode is large (~ 40 Hz) [5], which leads to large error bars in the tests of gravity; it was not accurate enough to perform stringent tests to rule out other alternative descriptions. Further, the BBH system that generated GW150914 signal comprised of nearly equal mass BHs. This produces a merger phase that excites primarily the dominant RD mode and suppresses sub-dominant mode excitations. Although the RD in GW150914 signal is consistent with the prediction of GR [5], it could not be used to perform precision tests of the strong field gravity. However, this signal gives us hope that for louder signals from BBH systems with a larger mass ratio, stringent tests of GR could be carried out using RD signals in the future.

The primary focus of this thesis is to develop the tools needed to probe the strong field gravity using the RD of a BBH merger. RD is a particularly appealing part of the BBH GW signal; it has an elegant analytical description offered by the BH perturbation theory.

¹LIGO detects stellar mass BHs, which are relatively small compared to say, the mass of the BH at the center of the galaxy. The smaller the BH, the higher the curvature close to the BH. With detections of BH in various mass ranges, we also probe gravity at different length scales and curvatures.

To complement this, since BBH evolution only deals with vacuum spacetime (unlike in the case of, say neutron star merges where it is hard to model complicated matter dynamics), numerical relativity (NR) can provide apprehensible insights into the strong-field dynamics. Although, the RD signals contain a rich set of information about the strong field dynamics and nature of the compact objects, the extraction of this information from of these signals are far from straightforward. Currently, the GW research community is building robust data analysis tools to test GR with BBH RDs. In this thesis, we explore aspects of BBH RD signal, using a conglomeration of techniques developed in analytical BH perturbation theory, NR and GW data analysis.

1.2 On the discovery of GW150914

Chapter 2 of this thesis summarizes the first direct detection of gravitational wave from a BBH merger, the GW150914. It was remarkably fortunate that the first detection also happened to be an extraordinary loud signal and that it allowed for visual inspection of the signal in the raw detector data with minimal data conditioning. We performed the first visualization of the GW signal in the raw data to check for visual consistency of the signal observed by the two detectors and the best-fit template reported by the search pipelines. A more refined version of this analysis was later performed by the LIGO collaboration and is presented in Figure 1 of the GW150914 discovery paper [3].

As a part of the LIGO collaboration, I was involved in the review process of an implementation of a waveform approximant that uses an effective one body formalism and includes precession effects during the inspiral, called the "SEOBNRv3" template family. This waveform family was used to improve the parameter estimation results of GW150914 and we summarize the astrophysical properties of GW150914 obtained by the LIGO collaboration using this waveform approximant.

1.3 On ringdown and scales of perturbation

Several RD-based tests of GR rely on verifying the predictions of BH perturbation theory using the GW observations. One of the major challenges of performing these tests is to identify where in the post-merger signal one needs to start this analysis, i.e., where does the RD start? One naive argument could be that one needs to at least wait until the scale of perturbation is smaller than the scale of the event horizon of the final BH formed for perturbation theory to be valid. This requires us to quantify the scale of perturbation which

is a difficult problem in the framework of GR. The diffeomorphic invariance of GR makes it hard to quantify the perturbation as a function of time of evolution. In Chapter 3, we set up two simplified toy models to explore the concept of scales of perturbation in BBH RD: i) a system comprising of two point masses and, ii) a rotating tri-axial ellipsoid. This work is primarily meant to develop an intuition towards the scales of perturbation that occurs in the source frame (close to BH) during the RD phase and to motivate the more precise study presented in Chapter 4.

1.4 On choosing the start time of binary black hole ringdown

In this chapter, we present an algorithmic method to analyze the choice of the RD start time in the observed waveform. This method is based on determining how close the post-merger BBH spacetime is to a Kerr BH which we call the *Kerrness*. Using numerical relativity simulations, we characterize the Kerrness of the strong-field region close to the BH using a set of local, gauge-invariant geometric and algebraic conditions that measure local isometry to Kerr. We produce a map that associates each time in the gravitational waveform with a value of each of these Kerrness measures; this map is produced by following outgoing null characteristics from the strong and near-field regions to the wave zone. We perform this analysis on a numerical relativity simulation with parameters consistent with GW150914.

The choice of RD start time of 3 ms after merger used in [5] to test GR using GW150914 corresponds to a high value of the dimensionless perturbation amplitude of $\sim 7.5 \times 10^{-3}$ in the strong-field region. This suggests that in higher SNR detections, one would need to start analyzing the signal at a later time for studies that depend on the validity of BH perturbation theory.

This chapter contains the work published as ‘On choosing the start time of binary black hole RD’ by *Swetha Bhagwat*, Maria Okounkova, Stefan W. Ballmer, Duncan A. Brown, Matthew Giesler, Mark A. Scheel, Saul A. Teukolsky [61].

1.5 On spectroscopic analysis of stellar mass black-hole mergers

In Chapter 5, we investigate the prospects of ground-based detectors to perform a spectroscopic analysis of signals emitted during the RD of the final Kerr black-hole formed by a stellar mass BBH merger. If we assume an optimistic rate of $240 \text{ Gpc}^{-3}\text{yr}^{-1}$, about 3 events per year can be measured with sufficient SNR to be spectroscopically interesting by the Advanced LIGO detectors. Upgrades to the existing LIGO detectors will increase the odds of measuring

multiple RD modes significantly. New ground-based facilities such as the Einstein Telescope or the Cosmic Explorer could measure multiple RD modes in about thousand events per year. We perform Monte-Carlo injections of 10^6 BBH mergers in a search volume defined by a sphere of radius 1500 Mpc centered at the detector, for various proposed ground-based detector models. We assume a uniform random distribution in component masses of the progenitor binaries, sky positions and orientations to investigate the fraction of the population that satisfy our criteria for detectability and resolvability of multiple RD modes. We investigate the detectability and resolvability of the sub-dominant spheroidal harmonic modes corresponding to $l = m = 3$, $l = m = 4$ and $l = 2, m = 1$. Our results indicate that the modes with $l = m = 3$ and $l = 2, m = 1$ are the most promising candidates for sub-dominant mode measurability. We find that for stellar mass black-hole mergers, resolvability is not a limiting criteria for these modes. We emphasize that the measurability of the $l = 2, m = 1$ mode is not impeded by the resolvability criterion.

This chapter contains the work published as ‘Spectroscopic analysis of stellar mass black-hole mergers in our local universe with ground-based gravitational wave detectors’ by *Swetha Bhagwat*, Duncan A. Brown, Stefan W. Ballmer [62].

1.6 On the detectability of the subdominant mode in a binary black hole ringdown

In the previous chapter, we tried to understand the prospects spectroscopic analysis in RD using a Fisher matrix formalism. In this Chapter, we will further explore this theme with a full Bayesian Parameter estimation framework. While Fisher matrix gives a good approximation to study the variance in the estimated parameters for a signal with a loud SNR, in reality to measure the parameters of the RD one generally uses full Bayesian Parameter estimation framework. Here, we are specifically interested in detecting the presence of the loudest subdominant mode in RD assuming that the underlying theory of gravity is GR.

To first order, whether or not one can detect a subdominant mode depends on the overall SNR ratio present in the RD signal and on the mode amplitude ratio. In this Chapter, we study zero noise-injections of RD signals, systematically varying both these parameters to understand their interplay. We perform a full Bayesian parameter estimation to detect the presence of the subdominant mode in a set of analytical ringdown signals. This study is done with the aim of developing an intuition on what kind of systems might allow us to detect the second mode at different SNRs. We find that detection of the subdominant mode seems

promising for unequal mass progenitor binaries with advanced LIGO detector. A follow up study with a real gaussian noise is underway.

This chapter contains the work that will be soon published as ‘Detectability of the subdominant mode in a binary black hole ringdown’ by *Swetha Bhagwat*, Miriam Cabero, Collin Capano, Badri Krishnan, Duncan Brown.

Chapter 2

On the discovery of GW150914

2.1 An overview on the search and the best-fit template

In the second generation detectors, a GW signal from a CBC event is generally buried in the detector noise and careful data analysis needs to be performed to extract the information of the signal from the raw detector data. Several GW search pipelines have been developed, equipped with various algorithms and techniques to detect the GW signal in the detector data [66, 67, 68, 63, 64, 65].

The search for GW from a CBC relies on a technique known as the *matched filtering* [69, 47]. The basic idea in matched filtering is to cross-correlate the data from the detector with the expected GW waveform. These expected GW waveforms are known as the *templates*. The waveforms are obtained by solving Einstein's equations, either using a variety of analytical approximations or numerically or with a combination of both analytical and numerical techniques [70]. Each method of solving Einstein's equation yields a *waveform family* or an *approximant*.

The operation of matched filtering can be written down as a weighted inner product in the frequency domain,

$$\mathcal{M}(t) = \langle s|h \rangle = 4\text{Re} \int_{f_{low}}^{f_{high}} \frac{s(f)h^*(f)e^{2\pi i f t}}{S_n(f)} df, \quad (2.1)$$

where $s(f)$ is the Fourier transform of the data and $h(f)$ is the template in the Fourier domain. $S_n(f)$ is the one-sided power spectral density (PSD) of the detector. PSD describes the sensitivity of the detector across the frequency band. It is computed by,

$$\langle s(f)s(f') \rangle = \frac{1}{2} S_n(f) \delta(f - f') \quad (2.2)$$

In practice, the detector data contains noise transients and is non-gaussian, and therefore additional statistical tools are implemented to construct a detection statistic [71, 72, 73, 64].

When a GW signal from a CBC event is present in the data, one does not know a priori the parameters of the CBC system. Therefore, a bank of templates is created and the data is matched against each of the templates present in this bank [73]. In the search pipeline, PyCBC, the template bank corresponds to waveforms emitted by the compact binary systems whose component masses have spins that are aligned/anti-aligned to the orbital angular momentum of the system (the bank is, thus, called an aligned spin bank). Further, the binaries are assumed to have negligible eccentricity. When constructing the template bank, one needs to sample the astrophysical parameter space sufficiently densely to be able to capture the GW signal with enough SNR but also keep the bank sparse enough so that it is computationally viable. In PyCBC, the template bank is generated such that no more than 3% SNR is lost due to the discreteness of the template bank. When a matched filter operation is performed throughout this bank, the search pipeline reports the parameters of the template that produces the maximum match as the *best-fit-template*. These parameters give an approximate estimate of the astrophysical parameters of the source but a further careful parameter estimation (PE) study is followed to infer the true parameters of the system. Note that the best-fit template parameters will depend on the state of the detectors at the time of the event, on the family of templates being used and the discreteness of the bank chosen.

2.2 On the detection of GW150914

On the 14th of September, 2015, both of the LIGO detectors recorded a GW signal consistent with what GR would predict when BHs with masses $\sim 36M_{\odot}$ and $\sim 29M_{\odot}$ inspiraled and merged [3, 74]. The signal was first found by a Generic transient search pipeline (specifically, a CWB pipeline) [66, 75] which identifies the events by looking at the coherent excess power in the time-frequency plots of the data from the two detectors. The signal was also reported by two independent CBC focused search pipelines. In this chapter, the specific CBC GW search pipeline we refer to is called PyCBC; it is an open source software package that has inbuilt algorithms to detect and analyze the CBC events using calibrated detector data. For the details of PyCBC search pipeline refer to [64].

To ensure that the signal is from an astrophysical source and not of instrumental origin, one must look for coincidence between the two detector's data. Since the detectors are far apart, one does not expect to see correlated noise sources and the data stream from each of

the detectors can be assumed as independent. Statistical significance is assigned to a GW detection by estimating the recurrence of witnessing an SNR comparable to (or greater than) the GW trigger solely due to noise coincidences. For reporting the statistical confidence of this detection, data from a total coincident observation time of 16 days¹ was used. From this data, a noise background equivalent to 608000 years was produced by performing unphysical time delay; the time shifts greater than 10 milliseconds (typically, a timeshift that is greater than the light travel time between the detectors) ensure that the simulated data stream contains no true astrophysical signal in it and contains simply the detector noise realization. The statistic used by the LIGO collaboration for detection is an empirically re-weighted new-SNR (SNR from the two detectors are added in quadrature and is called as combined-new SNR) details of which can be found in [78]. On analyzing the data containing the GW150914 event, it was found that this event has a combined SNR of 23.6. The false alarm probability was calculated to be $\sim 2 \times 10^{-7}$, which affirms that the signal corresponded to an astrophysical event. The statistical significance of this event was reported to be 5.1σ . It should be emphasized that this event was exceptionally loud.

The PyCBC search pipeline also reports the parameters of the best-fit-template, and therefore provides a rough estimate of the astrophysical parameters of the system immediately after identifying the event (in low latency). In Table 1, we list the best-fit parameters reported by the PyCBC search for the GW150914 event. It should be noted that the values of best-fit template parameters reported by the search differ from the parameters inferred on performing a Bayesian parameter estimation (compare Table 1 with results presented in papers [79]). However, the parameter estimation studies take a longer timescale (order of a few weeks). The study presented in section 2.3 was performed shortly after the GW150914 trigger was recorded. At that time, the parameter estimation studies were still being performed and the PE inferred values were not available. Therefore, for the study presented in section 2.3, we use the best-fit-template parameters presented in Table 1 (reported by the PyCBC search pipeline).

¹This is the duration of coincident data obtained after applying the data quality vetoes. The details of data quality checks and vetoes applied for the analysis of GW150914 event can be found in [76, 77]

Parameters	Best-fit value
Mass 1	49.9 M_{\odot}
Mass 2	36.6 M_{\odot}
Spin 1z	0.96
Spin 2z	-0.89
Effective distance in L1	1194.9118 Mpc
Effective distance in H1	970.70534 Mpc
Arrival phase in L1	0.58 rad
Arrival phase in H1	-2.77 rad

Table 1: The parameters of the best-fit-template for GW150914 trigger reported by the PyCBC search pipeline obtained by analyzing the data containing GW150914 trigger. These values are used in our study presented in section 2.3

2.3 Direct comparison of the data and best fit template

The exceptionally loud nature of GW150914 event prompted us to study the raw data from the detectors directly. In this study, we present the first visual consistency test of the GW150914 event directly from the raw data from the two LIGO detectors. The premise of this work is to visually check that the signal seen by the LIGO instruments at Hanford site (H1) and the Livingston site (L1) are consistent with each other, i.e., the data from each of the detectors can be lined up against each other. We additionally check that the data from the detectors are consistent with the best-fit template parameters reported by the search pipeline, thereby ensuring that both the detectors see the similarly astrophysical signal.

The raw GW strain seen by the LIGO detectors are recorded in a channel called the `GDS-CALIB-STRAIN`. The data in this channel is calibrated but no other data quality vetoes are applied. We use the data recorded in this channel from both the detectors and perform a minimal set of filtering needed to visually inspect the GW event in the data.

To compare the data from the two detectors, we first condition the data such that the unphysical artefacts that are introduced due to the detector’s configurations are removed. The sensitivity of the detectors is not uniform across all frequencies in its band; the noise of the detector as a function of the frequencies is encoded in the detector PSD. In reality, the detector noise is not really stationary, although for short time stretches it is a good approximation. Also, each detector in the network can have a different detector PSD depending on the state

of the instruments (in the duration around the event) and this also could vary with time. To remove this feature from the data, we ‘whiten’ it; the data from each of the detectors is Fourier transformed and is divided by the respective detector’s inverse noise amplitude spectrum in the Fourier domain.

The data is band-passed to remove frequencies at which the detector is not sensitive. Further, there are known physical mechanisms in the detectors that produce high amplitude noise contamination that are localized in a narrow frequency band in the raw detector data (for example, the harmonics of the electric power line frequencies, the harmonics of the resonance frequency of mirror suspensions fibres etc). In order to see the astrophysical signal, we have to notch out these contaminated frequency bands from the raw data. We do this using an analytical filter constructed using a zero-pole-gain (zpk-filter) model that notches out these frequencies. The filter that we use is depicted in the bottom right inlay panel of Figure 1. The filter is designed such that the amplitude is set to 1 at 100 Hz. Next, the data is filtered both forward and then backwards to ensure that filtering does not introduce a phase error (zero-phase filtering). Note that the filter is acausal (specifically, symmetric in time) and is designed to introduce a zero-phase offset. The impulse response of the filter can be seen in the top right inlay panel of Figure 1. At this point, it must be emphasized that these sets of filtering are very non-aggressive and are the minimal data conditioning that we had to perform in order to visually examine the data.

From the search pipeline, we find the time at which the SNR peaks in each of the detector data. This corresponds to the time when the template aligns best with the data. However, note that the value of this time-stamp may vary slightly when the search is performed using the different template families (also known as waveform approximants); they depend on the convention of defining the t_{merger} within the waveform family. We find that this difference in the time-stamps can affect the alignment of the template with the data.

To overlay the best-fit template on to the detector data, we need a time-domain template with the best-fit template parameters. However, typically the search uses a frequency domain template in order to increase computational efficiency. We construct a template bank consisting of a single time-domain template corresponding to the parameters given in Table 1. The template family used in our study corresponds to a spinning effective one body waveform (called the SEOBNRv2 approximant in the LAL code library) [80]. We then perform a search on the data containing the event using this single-template ‘template bank’ and record the reported time of the merger. Further, this reported time of merger is used to align the raw data from the two detectors. This is also used to align the best-fit template to the data to

Detector	Time-stamp (in sec)
L1	1126259462.415039062
H1	1126259462.422363281

Table 2: The time at which SNR timeseries peaks in each of the detector. The detector data is match filtered against a single time-domain template constructed using SEOBNRv2 waveform family. The template corresponds to a BBH system with the parameters set to the best-fit-template parameters reported by the PyCBC search.

produce the overlay plot presented in Figure 1. The merger times obtained are listed in Table 2.

We observed a time delay of 7.32 ms between the Livingston (L1) and Hanford (H1) detectors. Our analysis uses a sampling rate of 16384 Hz and therefore, to align the data from the two detectors, we shift the raw data of H1 by 120 sample points. Also, the two detectors detect signal arriving with different phase as their location and orientation are different. Therefore, the data is suitably phase shifted by the values presented in Table 1.

The result of this study is presented in Figure 1. We see an excellent agreement between the raw data from the two detectors (see the coherence in the green and the red curve in the main panel). Note that the best-fit template (the thin blue and black lines) match very well with the two detector data (and with each other). In this plot we see that a minimal set of non-aggressive filtering allows us to clearly see the inspiral and the merger phase of the GW signal buried in the detector noise. However, the RD portion of the waveform is buried under the noise floor.

A refined version of Figure 1 was prepared by the LIGO collaboration and is presented in the top two panels of Figure 1 in the GW150914 detection paper [3]. For the ease of comparison, we present this plot in Figure 2. Figure 2 differs from Figure 1 in the following ways. The template that was used in the making of Figure 1 of [3] used the numerical relativity (NR) waveform from the SXS-NR waveform catalogue indexed as SXS:BBH:0305. Note that this waveform also does not correspond to the most-likely or maximum a posteriori parameters reported by the parameter estimation presented in [79] and [1]. However, it produces an overlap of 0.993 with the maximum a posteriori parameters reported in [1]. The template amplitude, phase, and the arrival times are obtained by a ‘hand’ adjustment to approximately minimize the visual content of the residue. For data conditioning, a Butter-worth bandpass filter from 35.0 Hz to 350.0 Hz was applied followed by notching out frequencies where the PSD contained unphysical spikes.

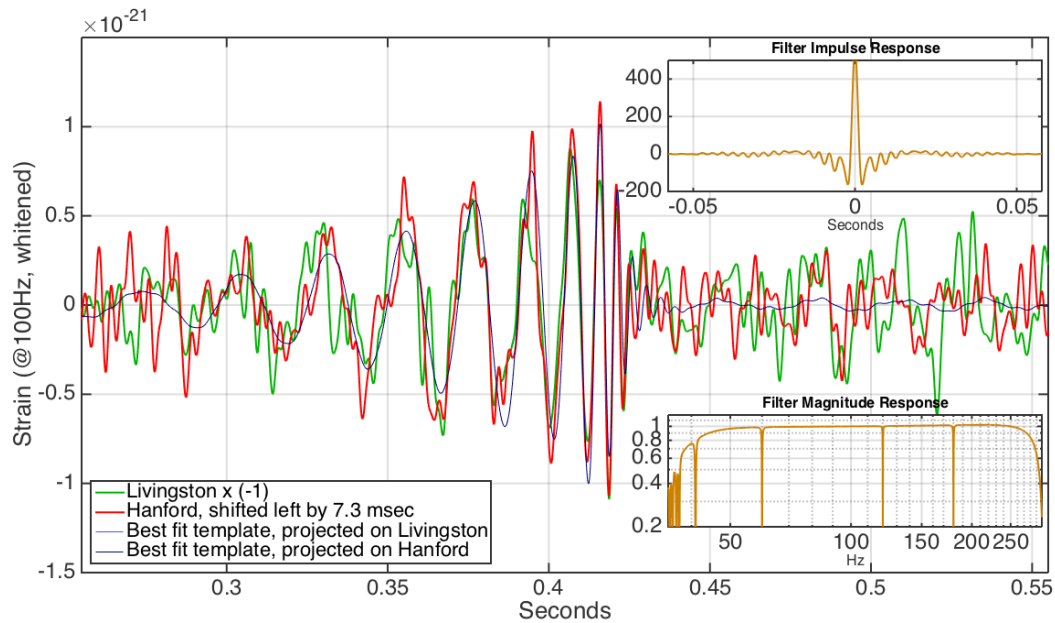


Figure 1: Direct comparison of the detector data with the best fit template. The data from the H1 and L1 have been minimally filtered and appropriately shifted to align with each other. The best-fit template corresponding to each of the detector timeseries is overlaid on the data. The inlay panels display the details of the filters used to condition the data. We see that with very minimal data conditioning, the data from the two detectors as well as the template aligns well, validating the presence of an astrophysical signal.

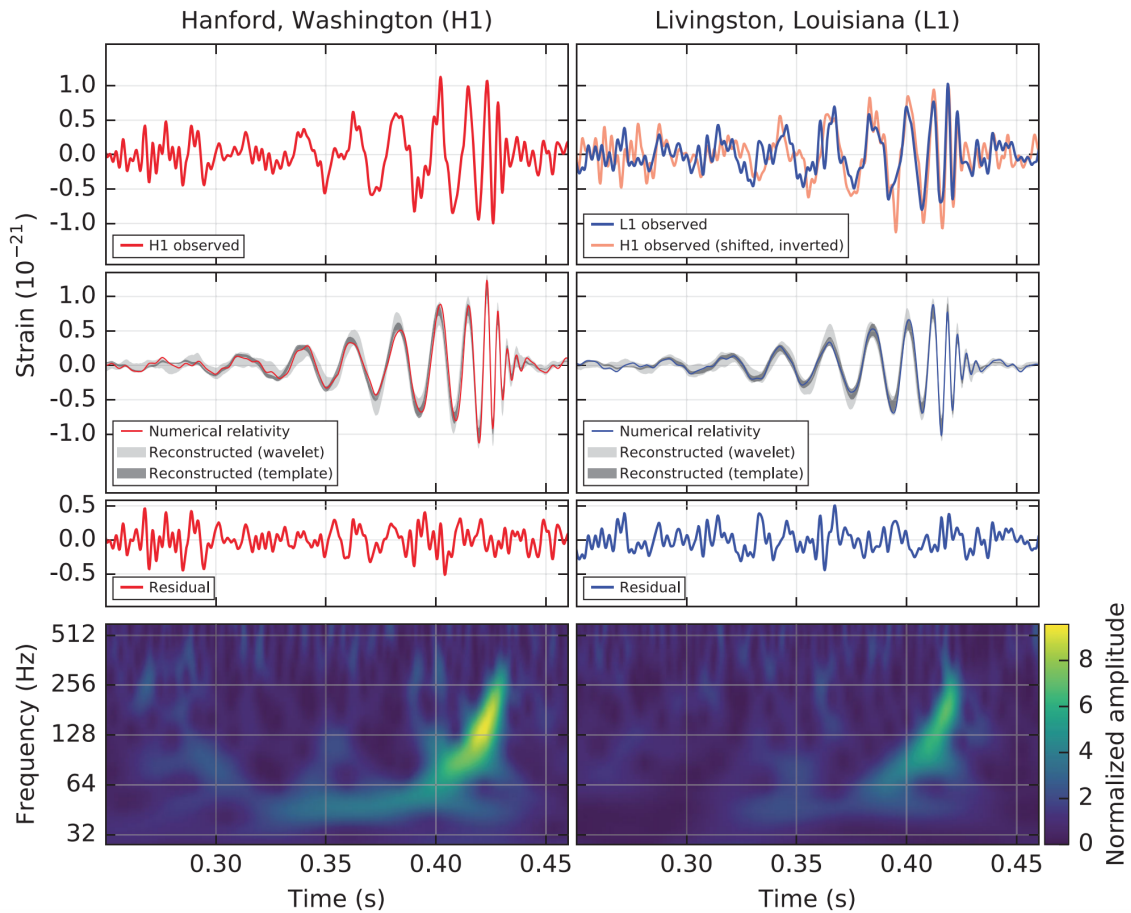


Figure 2: Figure 1 from GW150914 detection paper [3]. This Figure is taken from the GW150915 detection paper [3] by the LIGO collaboration. The top two panels of this Figure displays a more refined version of the plot we produce in our preliminary study presented in Figure 1. The bottom panel is a frequency-time plot, revealing a clear chirping in the data signal.

2.4 Parameters of GW150914 inferred using SEOBNRv3 waveform family

Since the parameters reported by the search are approximate, a Bayesian PE needs to be performed to estimate the astrophysical parameters. In this section, we review the parameters estimation results for GW150914 performed using a template family that includes spin and precession effect in the BBH waveforms using the framework of an Effective One Body (EOB) formulation. This section contains results of the PE studies performed by the LIGO collaboration that are presented in papers [79] and [1].

PE of GW150914 was initially performed using two template families that had independent ways of constructing the waveforms [79].

1. One of the template families used was based on an effective one body (EOB) formulation and is calibrated to a set of numerical relativity simulations. This model did not allow for a non-aligned spin, thereby, did not contain precession physics in the waveform modelling. In the LAL code library, the implementation of this template family is called `SEOBNRv2` [80]. To perform the PE study presented in [79], a reduced ordered model of this waveform in the frequency domain, called the `SEOBNRv2-ROM-DoubleSpin`, was used in view of computational efficiency.
2. The second waveform family used in the PE study presented in [79] models the waveform by phenomenologically predicting the amplitude and phase evolution. This waveform family is also calibrated to a set of numerical relativity simulations. However, in this waveform family, the precession physics of the binary system is incorporated i.e., it can generate waveform corresponding to non-aligned BBH systems. In the LAL code library, the implementation of this waveform family is called as the `IMRPhenomPv2` [81].

Two independent template families were used with the aim of understanding the effects of waveform modelling systematics on the inferred astrophysical parameters of the BBH [79]. However, since the waveform model `SEOBNRv2` lacks the precession physics in it, comparing them to quantify the modelling error was not entirely fair; it overestimates the errors on the upper bounds on systematic errors incurred due to the difference in waveform modelling. An implementation of the EOB template family that incorporated the precession physics was developed shortly after the initial parameter estimation analysis presented in [1] was concluded. The new implementation of precessing EOB waveform family was called `SEOBNRv3` and the details of the physics in modelling this waveform can be found in [82]. Then the

PE analysis was repeated using this new template family, thereby, giving a more realistic estimate of the effects of modelling errors between different IMR waveform families.

Table 3 presents the PE results obtained by the LIGO collaboration using the `SEOBNRv3` template family. It was found that the inferred parameters of GW150914 using the two precision models were indeed very close, affirming that inferred astrophysical parameters of the system are not affected significantly by the difference in the waveform models. The difference in inferred astrophysical parameters due to the differences in waveform family used for performing the PE study is beautifully visualized in Figure 1 of [1].

	precessing EOBNR
Detector-frame total mass M/M_\odot	$71.6^{+4.3}_{-4.1}$
Detector-frame chirp mass \mathcal{M}/M_\odot	$30.9^{+2.0}_{-1.9}$
Detector-frame primary mass m_1/M_\odot	$38.9^{+5.1}_{-3.7}$
Detector-frame secondary mass m_2/M_\odot	$32.7^{+3.6}_{-4.8}$
Detector-frame final mass M_f/M_\odot	$68.3^{+3.8}_{-3.7}$
Source-frame total mass $M^{\text{source}}/M_\odot$	$65.6^{+4.1}_{-3.8}$
Source-frame chirp mass $\mathcal{M}^{\text{source}}/M_\odot$	$28.3^{+1.8}_{-1.7}$
Source-frame primary mass $m_1^{\text{source}}/M_\odot$	$35.6^{+4.8}_{-3.4}$
Source-frame secondary mass $m_2^{\text{source}}/M_\odot$	$30.0^{+3.3}_{-4.4}$
Source-frame final mass $M_f^{\text{source}}/M_\odot$	$62.5^{+3.7}_{-3.4}$
Mass ratio q	$0.84^{+0.14}_{-0.20}$
Effective inspiral spin parameter χ_{eff}	$-0.02^{+0.14}_{-0.16}$
Effective precession spin parameter χ_p	$0.28^{+0.38}_{-0.21}$
Dimensionless primary spin magnitude a_1	$0.22^{+0.43}_{-0.20}$
Dimensionless secondary spin magnitude a_2	$0.29^{+0.52}_{-0.27}$
Final spin a_f	$0.68^{+0.05}_{-0.05}$
Luminosity distance D_L/Mpc	440^{+160}_{-180}
Source redshift z	$0.094^{+0.032}_{-0.037}$
Upper bound on primary spin magnitude a_1	0.54
Upper bound on secondary spin magnitude a_2	0.70
Lower bound on mass ratio q	0.69

Table 3: The parameters of GW150914 estimated by the LIGO collaboration using the fully precessing EOB templates. This table contains the first two columns presented in Table 1 of [1]. In this Table the median value of each of the parameters is quoted along with the 90% credible intervals.

Chapter 3

On ringdown and the scales of perturbation

3.1 The binary black hole ringdowns and the quasi-normal-modes

In GR, when two BHs merge, they form a highly distorted BH, that then rings down to settle to a final Kerr state ¹[83, 84]. The GWs radiated as the distorted BH settles down is known as the post-merger signal in a BBH waveform. Qualitatively, the post-merger signal contains two phases. The early part of the post-merger signal carries information about the highly non-linear dynamics of the strong field region (close to the BH). This part of the signal can only be modelled by solving the full Einstein’s equation using NR [70]. As the BH evolves towards its final state, the non-linearity is dissipated as GW and eventually, the system can be modelled as a linear perturbation on the spacetime of the final Kerr BH [85, 86, 87]. In this chapter, we will refer to this later part of the signal as ‘ringdown’ ².

When the final BH is in its ringdown stage, it can be analytically modeled using the perturbation theory. In Boyer-Lindquist coordinates (t, r, θ, ϕ) , the Kerr metric corresponding

¹Although we colloquially say that the BH settles to a Kerr state, strictly speaking, what we mean is that the spacetime of the merged BH is asymptotically (in time) locally isometric to the Kerr manifold. Kerr is a stationary spacetime and does not contain any nontrivial time evolution. It has a global time translation symmetry which is not true for a BBH ringdown spacetime.

²The definition of ringdown is not consistent among different papers in the literature. Some call the entire post-merger as ringdown while others choose to call the perturbative regime of post-merger as ringdown. In this work, I find it useful to use the second terminology.

to the spacetime of a BH with a mass M and a dimensionless spin a can be written as,

$$ds^2 = \left(1 - \frac{2Mr}{\Sigma}\right)dt^2 + \frac{4Mar \sin^2(\theta)}{\Sigma} dt d\phi - \frac{\Sigma}{\Delta} dr^2 - \Sigma d\theta^2 - \sin^2(\theta) \frac{r^2 + a^2 + 2Ma^2r \sin^2(\theta)}{\Sigma} d\phi^2. \quad (3.1)$$

Here, $\Sigma = r^2 + a^2 \cos^2 \theta$ and $\Delta = r^2 - 2Mr + a^2$. In the framework of GR, any perturbation on this metric is governed by a master equation called the Teukolsky's perturbation equation [85, 86, 87], given as

$$\begin{aligned} & \left\{ \frac{(r^2 + a^2)^2}{\Delta} - a^2 \sin^2 \theta \right\} \frac{\partial^2 \psi}{\partial t^2} + \frac{4Mar}{\Delta} \frac{\partial^2 \psi}{\partial t \partial \phi} + \left\{ \frac{a^2}{\Delta} - \frac{1}{\sin^2 \theta} \right\} \frac{\partial^2 \psi}{\partial \phi^2} \\ & - \Delta^{-s} \frac{\partial}{\partial r} \left\{ \Delta^{s+1} \frac{\partial \psi}{\partial r} \right\} - \frac{1}{\sin \theta} \frac{\partial}{\partial \theta} \left\{ \sin \theta \frac{\partial \psi}{\partial \theta} \right\} - 2s \left\{ \frac{a(r-M)}{\Delta} + \frac{\iota \cos \theta}{\sin^2 \theta} \right\} \frac{\partial \psi}{\partial \phi} \\ & - 2s \left\{ \frac{M(r^2 - a^2)}{\Delta} - r - \iota a \cos \theta \right\} \frac{\partial \psi}{\partial t} + (s^2 \cot^2 \theta - s) \psi = 4\pi \Sigma T. \end{aligned}$$

Here ψ is the field that satisfies the perturbation equation, T is the source term and the spin weight s describes the nature of perturbation. $s = 2$ corresponds to a gravitational perturbation while $s = 1$ and 0 correspond to vector (e.g. electromagnetic) perturbation and scalar perturbation respectively. Details on ψ , T and s are summarized in Table 1 of [85]. By casting this into a radiative boundary value problem and finding the eigensolution, one can obtain the characteristic resonance frequency of the BH. An inertial observer at the asymptotic future null infinity (\mathcal{I}^+) perceives the GW emitted by a perturbed BH as excitation of modes corresponding to a characteristic discrete frequencies (complex frequencies) spectrum. These are known as the quasi-normal-modes (QNMs) [88, 89]. Given $\{M_f, a_f\}$, the spectrum of QNMs is unique for a BH.

3.2 Ringdown as a probe for strong field gravity

Ringdowns serve as a powerful probe to understand the dynamics of strong field gravity. The equation governing the perturbation when cast in form of a radiative boundary value problem [90, 89, 83] takes a form similar to the Schrodinger equation and contains an effective potential for the BH [91]. Since QNMs are the solutions to this equation, observing them serves as a confirmation of:

1. The equation governing the perturbation: This in turn, is dictated by the Einstein's equation and therefore, will validate the dynamics predicted by GR.

2. The boundary conditions imposed in solving these equations: The boundary conditions encode the nature and geometry of the compact object. For instance, while on one hand for a BH one imposes the condition that there should be no outgoing radiation at the event horizon, on the other hand in the case of many of the exotic compact objects (ECO) the appropriate condition to impose is a (partially) reflective boundary condition at the surface of the compact object. The exact detail of the boundary condition will depend on the structure of the compact object [59, 60].
3. The effective potential of the compact object: This contains information about the spacetime geometry around the compact object.

Testing these features will allow us to validate GR and to place stringent constraints on the alternative theories of gravity.

3.3 Intuition on scales of perturbation and start time of ringdown

In order to perform tests of gravity that rely on the BH perturbation theory, it is crucial to understand which part of the postmerger signal can be described by the perturbation theory, i.e. where does the ringdown begin? This is not a straightforward question and there have been various attempts to address it ³[92, 93, 94, 95]. A general notion of validity of perturbation theory is that the scale of the perturbation should be much smaller than the scale intrinsic to the unperturbed system ⁴.

In sections 3.3.1 and 3.3.2, we develop two simplistic models to build an intuition on the scale of perturbation in the source frame as a function of time during a BBH ringdown. In both of these cases, we construct an effective source from the observed GW strain at future null infinity (\mathcal{I}^+) and use that to study the scales of perturbations in the ringdown. Then we apply these ideas to a GW waveform and present the result in section 3.3.3.

3.3.1 Model 1: Two point masses

Consider an effective system which is comprised of two point particle of mass m_1 and m_2 . Given this toy system, we now construct the evolution of the separation vector between the

³The diffeomorphic symmetry of GR makes it hard to both quantify the amplitude of perturbation in the source frame (there is no preferred metric) as well as to connect the source frame dynamics to GW observed at the \mathcal{I}^+ .

⁴The two physical features of a BH spacetime that can be used as an intrinsic scale are a) the event horizon (located at $2M$ for a Schwarzschild BH) and b) the light ring (located at $3M$ for a Schwarzschild BH).

two particle such that it produces the observed GW at \mathcal{S}^+ . In this study, GWs are computed only to the order of the quadrupole moment at \mathcal{S}^+ and we assume a quasi-Keplerian motion. Therefore, the system is an ‘effective system’ and does not correspond to a BBH merger; the source frame system is retroengineered to produce a BBH GW at \mathcal{S}^+ , but the source-frame does not model the dynamics of a BBH merger. We refer to the magnitude of separation as the effective radius (r_{eff}). r_{eff} serves as a rough guide to the scale of gravitational dynamics in the source-frame that we can map to an observed GW.

A GW strain $h(t)$ can be written down as,

$$h(t) = h_{\text{amp}} e^{i2\omega t}. \quad (3.2)$$

Here h_{amp} is the amplitude and ω is the orbital frequency. For the case of two point masses separated by r_{eff} , at a distance of R from the observer, h_{amp} has a magnitude of,

$$h_{\text{amp}} = \frac{-4Gr_{\text{eff}}^2\mu\omega^2}{c^4 R}. \quad (3.3)$$

Here, μ is the reduced mass of the system. From this, one can define r_{eff} as,

$$r_{\text{eff}}^2(t) = \frac{h_{\text{amp}}(t)c^4 R}{4G\mu\omega(t)^2} \quad (3.4)$$

Now, we find R assuming that far way from merger, the dynamics of binaries can be described by quasi-circular-Keplerian orbits. Using Kepler’s law,

$$r_{\text{eff}}(t) = \left(\frac{GM}{\omega^2} \right)^{1/3}, \quad (3.5)$$

where $M = m_1 + m_2$. We assume that R will not change in the timescale of evolution of the binaries. Let $t = t_0$ be some early time in the evolution of the binary system when the quasi-circular-Keplerian assumption holds. Then, the amplitude of the GW at $t = t_0$ can be expressed as,

$$h_{\text{amp}}(t_0) = \left(\frac{GM}{\pi^2 f^2} \right)^{2/3} \frac{4G\mu\pi^2 f^2}{c^4 R} \quad (3.6)$$

where $f = \frac{\omega}{\pi}$ is the GW frequency. Inverting for R ,

$$R = \frac{4G^{5/3}\mu M^{2/3}\pi^{2/3} f^{2/3}}{c^4 h_{\text{amp}}(t_0)} \quad (3.7)$$

Now, using Eq. 3.7, we can compute Eq. 3.4 for r_{eff} as a function of time.

In the early inspiral part of the evolution, we expect that r_{eff} will match the physical separation between the component masses of the BBH system. As the two BHs come closer

and the dynamics becomes more relativistic, r_{eff} will start to deviate away from the physical separation of the two BH. After merger, r_{eff} will give a length scale associated with quadrupole moment of the final remnant BH, providing a sense for scale of perturbation during the RD phase. For instance, as the final remnant rings down, we expect r_{eff} to exponentially decrease.

3.3.2 Model 2: Final black hole as a rotating tri-axial ellipsoid

Next, we build another toy model. We model the merged BH as a rotating triaxial ellipsoid with a time varying semi-axes. Here, the question we ask is how should the geometry of this tri-axial ellipsoid change such that an observer along the z axis (axis of spin of the final BH) will see a GW corresponding to the BBH merger. The scale of this change can be used as a way to develop an intuition of the scales of perturbation during a BBH RD.

Let I_i , where $i = \{1, 2, 3\}$, be the moment of inertia of a rotating tri-axial ellipsoid. Let $\{a, b, c\}$ be the semi-axis of the ellipsoid. The GW emitted by such a system is given by,

$$h(t) = \frac{4G(I_1 - I_2)\omega^2}{c^4 R} e^{i2\omega t}. \quad (3.8)$$

Here we identify amplitude of the GW as

$$h_{\text{amp}} \equiv \frac{-4G(I_1 - I_2)\omega^2}{c^4 R}. \quad (3.9)$$

The moment of inertia of an ellipsoid is given by,

$$I_1 = \frac{M_f(b^2 + c^2)}{5} \quad (3.10)$$

$$I_2 = \frac{M_f(a^2 + c^2)}{5}. \quad (3.11)$$

Then, the amplitude of the GW can be expressed as,

$$h_{\text{amp}} = \frac{-4GM_f(b^2 - a^2)\omega^2}{5c^4 R}. \quad (3.12)$$

We use the fitting formula obtained from numerical relativity for the M_f of the merged BH, presented in [96],

$$M_f = M(1 + ((8/9)^{1/2} - 1)\eta - 0.4333\eta^2 - 0.4392\eta^3). \quad (3.13)$$

Here η is the symmetric mass ratio of the binary system and M is the total mass of the BBH system. Plugging this back into Eq 3.12, we get

$$h_{\text{amp}} = \frac{4GM(1 + ((8/9)^{1/2} - 1)\eta - 0.4333\eta^2 - 0.4392\eta^3)(b^2 - a^2)\omega^2}{5c^4 R}. \quad (3.14)$$

Now notice that the quantity $(b^2 - a^2)$ gives a rough estimate of deformation of the final BH.

$$(b^2 - a^2) = \frac{5h_{\text{amp}}c^4R}{4GM_f\omega^2}. \quad (3.15)$$

In terms of parameters of the progenitor BBH,

$$(b^2 - a^2) = \frac{5h_{\text{amp}}c^4R}{4GM(1 + ((8/9)^{1/2} - 1)\eta - 0.4333\eta^2 - 0.4392\eta^3)\omega^2}. \quad (3.16)$$

For simplicity, let the scale of the system be the Schwarzschild radius (R_S) of the final BH (instead of the horizon size of the Kerr BH which is spin-dependent), given as,

$$R_S = 2\frac{GM_f}{c^2}. \quad (3.17)$$

This expressed in terms of η gives,

$$R_S = 2\frac{GM(1 + ((8/9)^{1/2} - 1)\eta - 0.4333\eta^2 - 0.4392\eta^3)}{c^2}. \quad (3.18)$$

We now have two scales; an intrinsic scale defined by the radius of the event horizon of the BH and a scale of perturbation given by $(b^2 - a^2)$. We shall now proceed to compare these two scales by defining a measure of fractional deformation $\delta(t)$ of the final BH as,

$$\delta(t) = \frac{(b^2 - a^2)(t)}{R_S^2}. \quad (3.19)$$

For a perturbative analysis to be valid, we demand $\delta(t) \ll 1$. In other words, the scale of the perturbation should be smaller than at least the inherent scale of the system (i.e) the Schwarzschild radius of the final BH that is formed. This imposes the condition that, for perturbative analysis to be valid, the following condition has to be satisfied

$$\delta(t) = \frac{(b^2 - a^2)(t)}{R_S^2} = \frac{5h_{\text{amp}}(t)c^2R}{2R_S^3}. \quad (3.20)$$

$$= \frac{5\mu}{M_f} \frac{r_{\text{eff}}^2}{R_S^2} \quad (3.21)$$

$$\ll 1. \quad (3.22)$$

3.3.3 On the scales of perturbation in a GW150914-like ringdown using our toy models

Having developed two independent toy models to understand the scale of perturbation to the intrinsic scale of the system, in this section, we investigate the implication on a BBH system.

We apply the ideas developed in sections 3.3.1 and 3.3.2 to the GW emitted by a system with the progenitor masses $m_1 = 49M_\odot$ and $m_2 = 36M_\odot$ and with dimensionless spins along the z-direction corresponding to $s_{1z} = 0.96$ and $s_{2z} = -0.89$. These are the intrinsic parameters reported by the PyCBC search pipeline [63, 64, 65] for the event GW150914. We use an aligned spin inspiral-merger-ringdown (IMR) waveform approximant (called the SEOBNRv2 in the LIGO analysis library (LAL)) to produce the waveform with these parameters. The peak of the strain amplitude occurs at time $t = 0$. We then use this waveform to compute r_{eff} as defined in Eq 3.4 and mark it on the waveform in Figure 3. Note that the solid vertical lines marking r_{eff} smaller than the Schwarzschild radius are meaningful as the radius of separation only for the effective point particle model and not for a true BBH system. Although it can not be interpreted as the radius of separation, r_{eff} gives a scale for the perturbation for the BBH system during the post-merger phase. In Figure 3, we see that the line for $r_{\text{eff}} = 2M$ (which we identify as the intrinsic scale of the system) corresponds to about half a cycle after the merger. This implies that one must wait for at least half a cycle after the peak for perturbation analysis to hold.

Next, we compute the evolution of the deformation parameter $\delta(t)$ for the waveform and present it in Figure 4. Note that Figure 4 has the same time axis as the Figure 3. For perturbation theory to hold, we demand that δ be less than 1. From Figure 4, we infer that for analysis based on perturbation theory one should at least wait for roughly 0.005 ms after the peak of the waveform.

Both the models used are simple toy models, studied primarily built with the intention of developing an intuition for the scales of perturbation during BBH RD. These are oversimplified models compared to the rich non-linear and strong field dynamics that occur in a general relativistic BBH merger-RD. Moreover, in defining δ , we have used the Schwarzschild radius as the intrinsic scale of the system, whereas the final BH in a BBH merger is a Kerr BH (unless in case of head-on collisions).

In the next chapter, we will address the issue on the start time of RD in a more rigorous way using a full NR evolution of the BBH spacetime. In particular, we will compare the changing geometry of a dynamical spacetime during a BBH merger to that of a stationary Kerr manifold and predict the start time of RD.

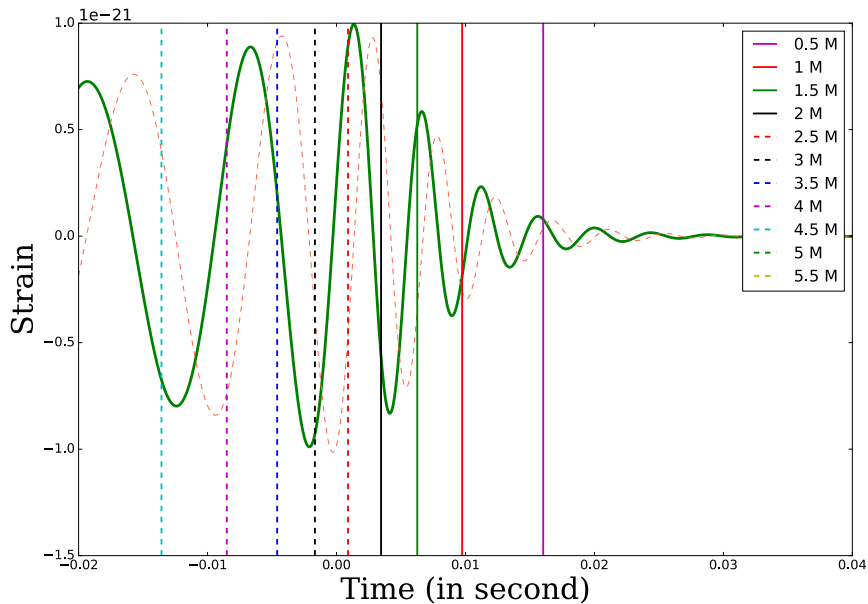


Figure 3: r_{eff} marked on the GW strain. This plot presents the GW waveform corresponding to the best-fit template parameters reported by the PyCBC search pipeline for the event GW150914. The solid waveform is the $+$ polarization and the dotted one is the \times polarization of the GW strain $h(t)$. The waveform is zoomed-in on the last few cycles. The lines indicate to the value of r_{eff} at different times of the evolution. The dotted lines correspond to separation vector before merger of the BBH system and the solid line correspond to un-physical separation, that provide the scale of perturbation during the merger-ringdown phase of the BBH evolution. We use the units where $G = c = 1$.

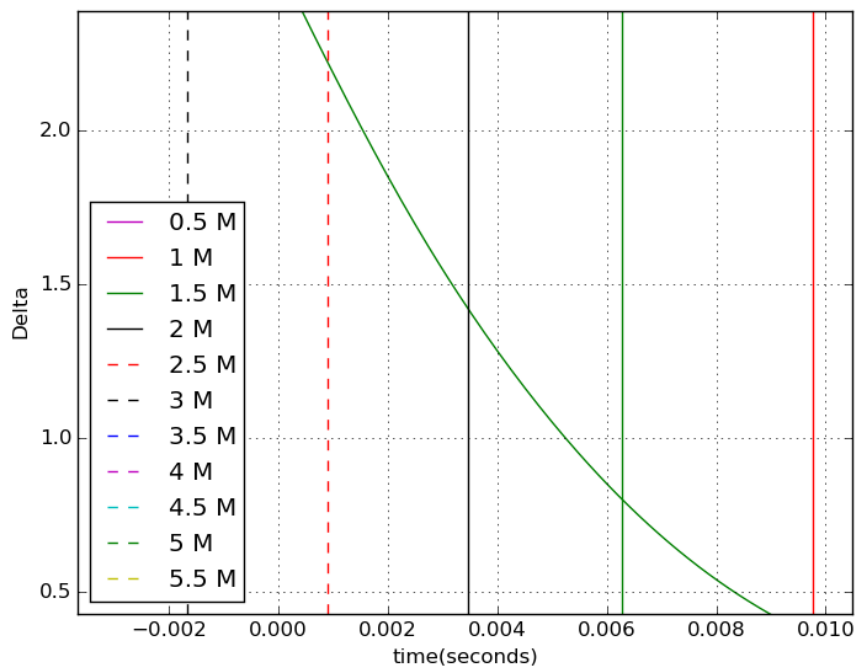


Figure 4: The distortion parameter δ as a function of time. This plot depicts the evolution of the distortion parameter δ defined in Equation 3.20. The scale of the perturbation is comparable to the intrinsic scale of the system roughly when $\delta = 1$. We see that about 0.005 sec after the peak of the waveform, the value of $\delta \sim 1$. Note that by convention used in the waveform family the merger is set at $t = 0$ (see Figure 3). We assert that any perturbative analysis should start later than this time.

Chapter 4

On choosing the start time of binary black hole ringdown

4.1 Introduction

The quasi-normal mode (QNM) spectrum seen during the ringdown of a perturbed black hole (BH) is determined by the Teukolsky equation; it carries the signature of the BH potential along with the BH horizon and asymptotic boundary conditions [85, 86, 87]. The recent detections of binary black hole (BBH) gravitational wave (GW) signals by LIGO (the Laser Interferometer Gravitational-Wave Observatory) [97, 98, 37, 99, 100] allow us to begin to probe this QNM signature [5]. The QNM spectrum in a gravitational-wave observation allows us to perform tests of the no-hair theorem. This theorem states that vacuum, asymptotically flat, stationary, axisymmetric, uncharged BHs are completely characterized by two parameters: the mass and the spin [49, 50, 51, 52, 53]. This allows us to constrain modified theories of gravity that violate the no-hair theorem [101, 42]. Observing the QNM spectrum in GWs can be used to validate the BH uniqueness theorem. This theorem states that the exterior geometry of an vacuum, asymptotically flat, stationary, axisymmetric, uncharged BH must be Kerr [49, 102].

However, testing the no-hair and uniqueness theorems relies on observing GWs from the QNM perturbative regime (without additional transients remaining from the inspiral). This requires an appropriate choice of start time of this regime.¹ Identifying this time in the signal is mathematically an ill-defined problem, since QNMs form an incomplete and non-orthogonal

¹While conventions in the literature vary, in this chapter, by ‘ringdown’, we explicitly mean the part of the post-merger gravitational waveform that can be described in terms of QNMs.

basis [103, 104]. Hence, the conventions for choosing the start time of the ringdown have varied in the literature. Berti et al. [92] and Baibhav et al. [93] chose the start time based on maximizing the energy contained in the QNM. London et al. [94] used $10 M$ after the peak of the dominant mode of Ψ_4 (the Newman-Penrose scalar that encodes outgoing radiation) for fitting to NR waveforms.² Kamaretsos et al. [95] chose $10 M$ after the peak luminosity of the dominant mode of the waveform, while Thrane et al. [105] proposed a loudness-dependent start time. In the GW150914 testing general relativity (GR) chapter [5], different start times were used to perform the QNM analysis shown in Fig. 5 of that chapter, and the results were consistent with GR when the start time was picked as 3 ms (or later) after the merger.

None of these methods use information from the strong field to motivate the start times. The strong field refers to the region near the BHs (typically within a radius of few M), where the scale of the curvature is much smaller than the wavelength of a gravitational wave. In this chapter, we develop an algorithmic method for validating choices of the start time of ringdown using strong-field features. Specifically, we measure the *Kerrness*, or closeness to Kerr, in the strong-field region of an NR simulation ringdown, and use null characteristics to map Kerrness onto the GW at asymptotic future null infinity, \mathcal{I}^+ . We then demonstrate this method on a GW150914-like system. However, this method is generic, and this procedure can be carried out for any BBH system.

Determining Kerrness in the strong-field regime is non-trivial, since one needs a coordinate-invariant way of identifying a metric as Kerr. Necessary and sufficient conditions for a gauge-invariant characterization of local isometry to a Kerr manifold were proposed by García-Parrado Gómez-Lobo in [106].³ We use this set of algebraic and geometric conditions to provide a numerical measure of Kerrness. Previous studies have used multipole moments of the BH apparent horizon [4], horizon spin measurement comparisons [107], or Petrov classification [108, 109, 110] to characterize ringdown spacetimes. Our work is the first set of conditions that completely characterizes a spacetime as isometric to a Kerr manifold. We study the violation of these conditions post-merger in the strong field of a BBH simulation.

Connecting the strong-field region to the wave zone is a challenge, as the simulation gauge is different from the gauge in which GWs are observed. There is no straightforward way to transform between these gauges. Furthermore, establishing simultaneity between events is not possible in the GR framework, and thus there is no direct map between an event in the strong-field region and a point on the waveform. We therefore devise a scheme to

² Since vacuum GR is a scale-invariant theory, it is convenient to express distance and time in terms of source mass by setting $G = c = 1$. Explicitly, $1 M = M_{\text{BH}} \times G/c^3$ seconds, where M_{BH} is the mass of the BH.

³Throughout this text, *isometry* refers to the smooth mapping of manifolds equipped with metrics.

approximately associate the two frames. The association used in this study is of a cause-effect nature: we follow the outgoing null characteristics from the strong-field region to the wave zone using a Cauchy Characteristic Extraction scheme (CCE) [111, 112, 113], and associate events in the strong field to the wave zone. However, given that GR is a nonlinear theory, the source associated with a particular feature in the GW signal may not be well localized in the spacetime. Nevertheless, one would expect that the source dynamics that dominantly contribute to certain features in the waveform be localizable to a certain extent. Several such approximate localizations have been performed in linear perturbation theory [114, 115].

This chapter is organized as follows. Sec. 4.2 presents the theoretical methods used in this chapter, and Sec. 4.3 discusses their implementation in NR simulations. Sec. 4.4 then presents and discusses the results of applying these methods to an NR simulation with GW150914-like parameters. We conclude in Sec. 4.5. Figs. 19 and 27 are the flagship figures, presenting our major results. The the results are quantitatively summarized in Table 6.

Conventions

We work with the standard 3+1 decomposition of NR (cf. [116] for an introduction). In this chapter, g_{ab} refers to the spacetime metric, n^a refers to the timelike unit normal vector, γ_{ij} refers to the spatial metric on each slice, D_i is the covariant derivative with respect to γ_{ij} , and K_{ij} refers to the extrinsic curvature. We set $G = c = 1$ and express all quantities in terms of M , the sum of the Christodoulou Masses of the two BHs at the start of the simulation. Latin letters at the start of the alphabet, $\{a, b, c, d\}$, refer to (4-dimensional) spacetime indices, while Latin letters in the middle of the alphabet, $\{i, j, k, l, m, n\}$ are (3-dimensional) spatial indices. We denote complex conjugation by an overbar (e.g. \bar{A}). To avoid confusion among the multiple meanings of ‘data’ in this chapter, we refer to the vacuum data $\{\gamma_{ij}, K_{ij}\}$ on a spatial slice simply as ‘a slice’.⁴ Similarly, rather than being purely geometric, a ‘slicing’ in our case is a foliation equipped with a coordinate chart.

4.2 Theory

4.2.1 Characterizing strong-field Kerrness

First, we explain our method of measuring Kerrness in the strong-field region and develop a method to map it onto \mathcal{S}^+ . Secs. 4.2.1 and 4.2.1 discuss theoretically characterizing Kerrness

⁴*Vacuum data* means that the spatial metric, γ_{ij} , and the extrinsic curvature K_{ij} satisfy a set of constraint equations corresponding to the decomposition of the vacuum Einstein equations.

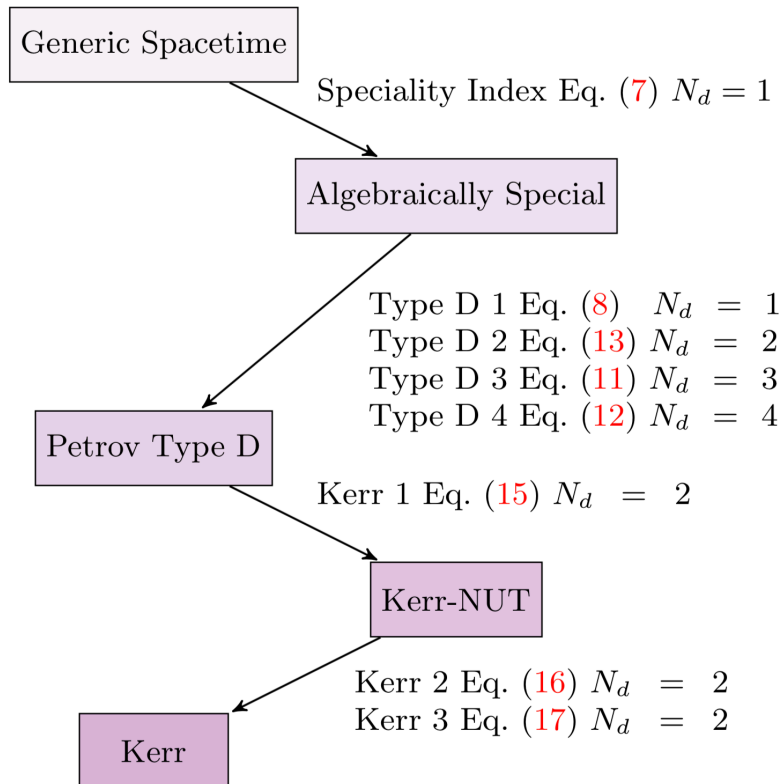


Figure 5: The set of conditions for a slice to be locally isometric to Kerr. The nodes refer to the resulting type of spacetime when the conditions on each edge, given by their name and equation in the text, are met. For example, a spacetime must meet all four of the conditions specified in the edge from Algebraically Special to Petrov Type D to belong to the type D subset of algebraically special spacetimes. In numerical applications, the failure of these Kerrness conditions to be met gives a set of respective Kerrness measures, where larger measures denote greater deviation from Kerr. For each measure, we give N_d , the number of numerical derivatives beyond the first derivatives of the metric needed to evaluate it, which corresponds to the numerical noise level in the measure, with higher derivative powers giving more numerical noise.

in the strong-field region, while Secs. 4.2.2, 4.2.2, and 4.2.2 discuss mapping strong-field information onto the wave zone via null characteristics.

Overview and historical background

Our overall goal in this section is to evaluate *Kerrness*: how close a numerical BH ringdown spacetime is to being locally isometric to the Kerr spacetime. In order to evaluate the Kerrness of a spacetime, we first need a set of theoretical conditions to evaluate whether a spacetime *is* isometric to Kerr. We can then turn these conditions into a set of *measures*, where deviation from zero indicates being farther from being locally isometric to Kerr. In a numerical simulation, one would evaluate these measures on spatial slices of a simulation. To characterize Kerrness in the strong-field region, one needs local quantifiers evaluated close to the BH, as opposed to looking at regions far away which are contaminated by gravitational radiation. Consequently, we seek a point-wise measure and do not use global measures on a slice such as those proposed in [117, 118, 119].

Uniquely characterizing a spacetime as Kerr has been historically challenging—until recently one could only classify spacetimes up to a Petrov type, which gives a weaker classification that admits several manifolds besides Kerr. The Petrov classification uses algebraic properties of the Weyl tensor C_{abcd} based on the four principal null directions (PNDs), by solving the eigenbivector problem (cf. [120] for a review)

$$\frac{1}{2}C^{ab}{}_{cd}X^{cd} = \lambda X^{ab}, \quad (4.1)$$

where eigenbivectors $X_{(\alpha)}^{ab}$ have eigenvalues $\lambda_{(\alpha)}$. The degeneracies of the PNDs give a unique algebraic classification of a spacetime. A spacetime with no repeated PNDs is fully general (Petrov Type I). A spacetime with at least one repeated PND is *algebraically special*. The Kerr metric belongs to a particular class of algebraically special spacetimes, the set of type D spacetimes, which have two double PNDs. A necessary condition for the manifold to be locally isometric to Kerr is to be type D.

Campanelli et al. [109] used this approach to analyze a numerical BBH ringdown. They determined the degeneracies between the PNDs by solving the eigenbivector problem and measuring the difference between eigenvalues. Their analysis found that the spacetime first numerically settled to type II, which has only one double PND, and then to type D. Owen [110] later showed that this measure was sensitive to the choice of tetrad used to compute the Weyl scalars needed to solve the characteristic equation. He proposed a new measure, less-sensitive to the choice of tetrad, and showed that the spacetime settled to type D without first settling to type II.

A type D spacetime can then be shown to be locally isometric to Kerr through additional conditions. Kerr belongs to the Kerr-NUT subset of type D spacetimes. One needs to show that a spacetime is Kerr-NUT and then constrain the acceleration and the NUT parameters. We give more information on Kerr-NUT spacetimes and the various parameters in Appendix A.1. Ref. [109] investigated the asymptotic behavior of the acceleration and the NUT parameter on a BBH simulation and showed they were constrained to be those of Kerr.

In this study, we do not solve the eigenbivector problem, but rather use a set of local algebraic and geometric conditions recently proposed by García-Parrado Gómez-Lobo [106] to show that a spacetime is locally isometric to Kerr. These conditions are formulated in a fully covariant way and thus avoid the complications in [109] and [110] due to tetrad choice.

Necessary and sufficient Kerrness conditions

To characterize a spatial Cauchy slice as isometric to Kerr, we first check if the slice is algebraically special. Next, we use two geometric conditions to check for the existence of Killing vectors (KVs) on the slice, and we impose two algebraic conditions to verify that the slice containing the KVs is type D. Then, we check the properties of the KVs and further classify the slice into the Kerr-NUT subfamily. Finally, imposing conditions on the acceleration and NUT parameters, we completely characterize the slice as locally isometric to Kerr. These conditions are summarized in Fig. 5.

All algebraic conditions are expressed in terms of electric and magnetic parts of the Weyl tensor, C_{abcd} , as

$$E_{ab} \equiv +C_{acbd}n^cn^d, \quad (4.2)$$

$$B_{ab} \equiv -{}^*C_{acbd}n^cn^d, \quad (4.3)$$

where the left dual of the Weyl tensor is defined as ${}^*C^{abcd} \equiv \frac{1}{2}\epsilon^{abef}C_{ef}{}^{cd}$. For a vacuum spacetime, these spatial tensors can be more readily evaluated on a slice as

$$E_{ij} = K_{ij}K^k{}_k - K_i{}^kK_{jk} + {}^{(3)}R_{ij}, \quad (4.4)$$

$$B_{ij} = -\epsilon_{kl(i}D^kK_{j)}^l, \quad (4.5)$$

where ${}^{(3)}R_{ij}$ is the spatial Ricci tensor evaluated from γ_{ij} . These can be combined into a complex quantity as

$$\mathcal{E}_{ij} \equiv \frac{1}{2}(E_{ij} - iB_{ij}). \quad (4.6)$$

In [106], the algebraic condition for a slice to be locally algebraically special is given in Eq. 85 as

$$\text{Speciality Index: } 6b^2 - a^3 = 0, \quad (4.7)$$

where

$$\begin{aligned} a &\equiv 16\mathcal{E}_{ij}\mathcal{E}^{ij}, \\ b &\equiv -64\mathcal{E}_i^k\mathcal{E}^{ij}\mathcal{E}_{jk}. \end{aligned}$$

This condition is equivalent to the speciality index in the Petrov classification literature (cf. Eq. 4.13 of [120]).

Recall that algebraic speciality corresponds to having one double PND, and hence is a weaker condition than being type D, which corresponds to having two double PNDs. A *necessary* algebraic condition for a slice to be type D is given in Theorem 4 of [106] as

$$\text{Type D 1: } \frac{a}{12}\gamma_{ij} - \frac{b}{a}\mathcal{E}_{ij} - 4\mathcal{E}_i^k\mathcal{E}_{jk} = 0, \quad (4.8)$$

which makes use of 4-dimensional algebraic conditions proven in [121] and orthogonally splits these onto the spatial slice. Here we have called the condition ‘Type D 1’ purely for bookkeeping purposes, in order to label each of the type D conditions.

The three *sufficient* conditions for a slice to be type D consist of two geometric conditions involving KVs and one algebraic condition which also includes the KV. As proven in Theorem 2 of [106], a vacuum type D spacetime has a complex KV field ξ^a which satisfies an algebraic condition

$$\Xi_{ab} = \frac{27}{2}w^{\frac{11}{3}}\xi_a\xi_b, \quad (4.9)$$

where Ξ_{ab} is derived from the Weyl tensor, and

$$w \equiv -\frac{b}{2a}. \quad (4.10)$$

However, one must show that a KV field exists on the slice in the first place, and then that it satisfies the properties given in Eq. (4.9). The necessary and sufficient geometric conditions for a slice to contain a KV field are known as Killing Initial Data (KID), and for a vector $\xi^a = Yn^a + Y^a$, are given as

$$\text{Type D 3: } D_{(i}Y_{j)} - YK_{ij} = 0, \quad (4.11)$$

$$\begin{aligned} \text{Type D 4: } D_i D_j Y - \mathcal{L}_{Y^l} K_{ij} \\ - Y({}^{(3)}R_{ij} + KK_{ij} - 2K_{il}K_j^l) = 0. \end{aligned} \quad (4.12)$$

Satisfying these conditions guarantees that a KV field exists on the slice—note that these two conditions say nothing so far about type D.

We can then relate this KV field ξ^a to the condition on the KV in a type D spacetime given in Eq. (4.9) by requiring

$$\begin{aligned} \mathbf{Type\ D\ 2} : & \mathcal{E}_{pj}(\Omega^2 + \Omega_l\Omega^l), \\ & - 2\Omega^l \left(i\mathcal{E}_{(p}^k \varepsilon_{j)lk}\Omega + \mathcal{E}_{l(p}\Omega_{j)} \right) \\ & + \gamma_{pj} \left(\frac{1}{2}w\Omega^2 + \Omega^l \left(-\frac{1}{2}w\Omega_l + \mathcal{E}_{lk}\Omega^k \right) \right) \\ & + \frac{1}{2}w\Omega_p\Omega_j - \frac{27}{2}w^{11/3}Y_pY_j = 0, \end{aligned} \quad (4.13)$$

where Eq. (4.13) is the orthogonal splitting of Eq. (4.9), and

$$\begin{aligned} \Omega_j & \equiv D_k w, \\ \Omega & \equiv K^{jk}\mathcal{E}_{jk} - wK - 16i\frac{w}{a}\mathcal{E}^{jk}\varepsilon_{kpl}D^l\mathcal{E}_j^p, \\ Y & \equiv (w\Omega_j\Omega^j + 2\mathcal{E}_{jk}\Omega^j\Omega^k)^{1/2}w^{-11/6}, \\ Y_j & \equiv \frac{\Omega(2\mathcal{E}_{jk}\Omega^k + w\Omega_j) - 2i\varepsilon_{jkl}\mathcal{E}_p^l\Omega^p\Omega^k}{27Yw^{11/3}}. \end{aligned} \quad (4.14)$$

This procedure is shown in Theorem 6 of [106].⁵

Type D 3 and Type D 4 are independent geometric conditions that depend on the complex KV ξ^a and show that the slice is KID. Type D 1 is a purely algebraic condition that informs us of the behavior of the PNDs. Type D 2 ties in the algebraic and geometric conditions, thereby completing the classification into type D. Speciality Index, meanwhile, is an independent algebraic condition.

In order to then show that an algebraically special, type D slice is locally isometric to Kerr, we must also show that it belongs to the Kerr-NUT subset of type D spacetimes. Kerr-NUT spacetimes have the symmetry property of two commuting KVs [120] - one spacelike and timelike, and thus if we impose this geometric condition on KV ξ^a as defined above, we arrive at the condition given in Theorem 8 of [106],⁶

$$\mathbf{Kerr\ 1} : \text{Im}(Y\bar{Y}_j) = 0. \quad (4.15)$$

⁵The Type D 2 condition has a + in the second term where [106] has a -. The sign error has been confirmed by the author of [106]. Similarly, The factor of $\frac{1}{27}$ in the definition of Y_j is not included in [106], but is in the corresponding Mathematica notebook [122].

⁶However, this has a typographical error (confirmed by the author [122]), and should include \bar{Y}_j , the complex conjugate, as given Eq. (4.15).

In order to further show that a slice is locally isometric to Kerr, we must place constraints on the parameters characterizing Kerr-NUT spacetimes. We summarize the parameters involved in Type D spacetimes in Appendix A.1. We require that λ , the NUT parameter, vanish, and ϵ , which is related to the acceleration of the BH, be greater than zero. These conditions are given in Theorem 8 of [106] as

$$\mathbf{Kerr\ 2} : Z^3 \bar{w}^8 \in \mathbb{R}^- , \quad (4.16)$$

for the condition $\lambda = 0$, where $Z \equiv \nabla_a w \nabla^a w$, and

$$\mathbf{Kerr\ 3} : -|Z|^2 + 18\text{Re}(w^3 \bar{Z}) > 0 , \quad (4.17)$$

for $\epsilon > 0$. However, the above expression only holds outside of the ergoregion [122] in Kerr. This condition is thus impractical to use in this study, since it involves finding the ergoregion, and masking this region would introduce high levels of numerical error within a spectral code.

Thus, for a slice to be locally isometric to Kerr, it must satisfy all of the above conditions, which are summarized in Fig. 5. Since the vacuum spacetime at the start of a ringdown may be fully general, the left hand sides of the Kerrness conditions will not necessarily be zero on some slices. Instead, the Kerrness conditions turn into a set of *Kerrness measures*, where larger deviation from zero indicates a larger deviation from being isometric to Kerr.

4.2.2 Connecting strong-field information to \mathcal{I}^+

Motivation

Having characterized the Kerrness in the strong-field region, we connect this information to the GWs at \mathcal{I}^+ . We develop a framework to map the evolution of the Kerrness measures computed during a post-merger simulation to the evolution of the post-merger waveform in the asymptotic frame. This provides a procedure to validate the choices of start time of ringdown when analyzing a gravitational-wave signal.

Just after the two BHs merge, the newly formed BH is expected to be highly distorted. The dynamics of the BH can be explained only via a full numerical simulation. At \mathcal{I}^+ , where the GWs are observed, these strong-field dynamics are responsible for features in a small region close to the peak of the GW amplitude. Once the excitation amplitude in the strong-field region decays to a level when linear perturbation theory is valid the spacetime dynamics and the associated waveform is governed by the Teukolsky equation [85, 86, 87]. At \mathcal{I}^+ , the waveform appears as a sum of exponentially damped sinusoids with a specific

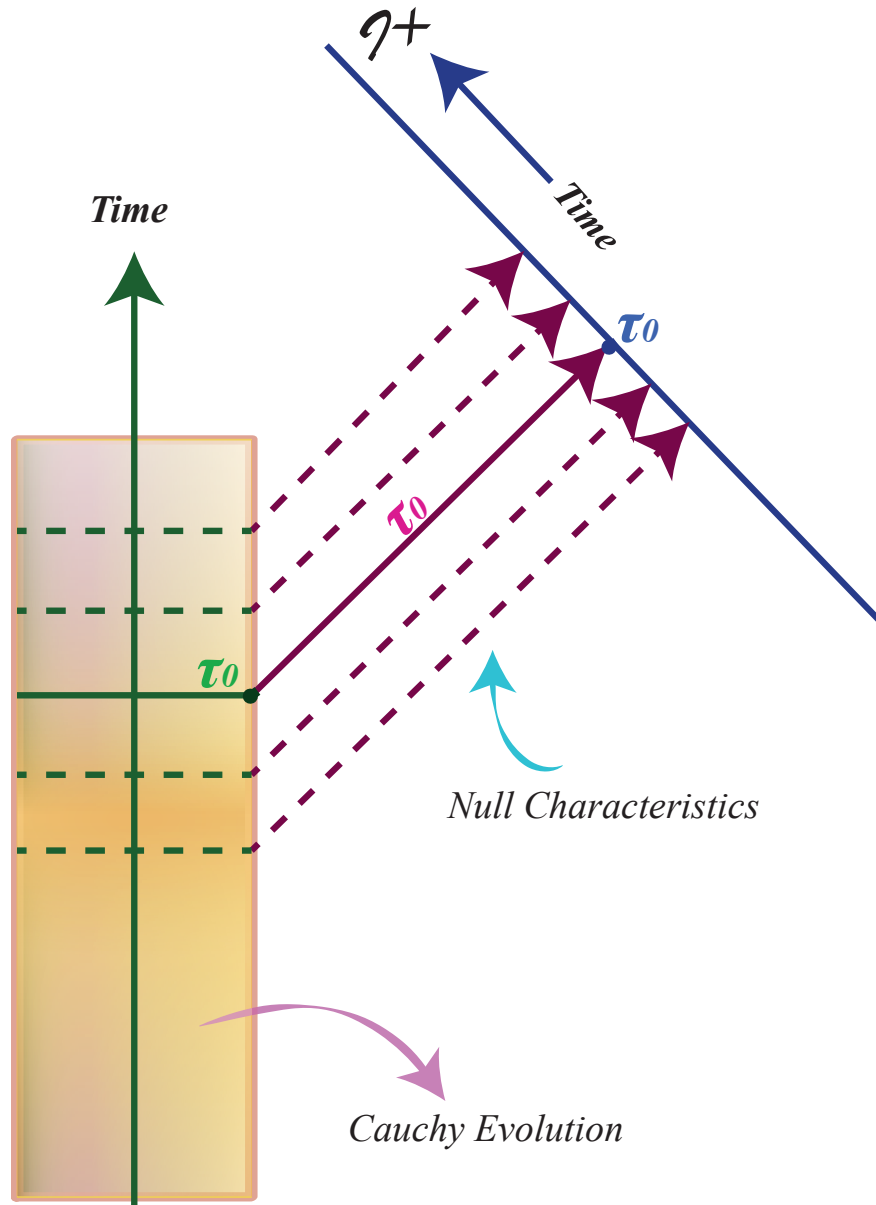


Figure 6: Prescription for connecting the strong-field information to the asymptotic frame dynamics. The colored cylinder represents the region of spacetime that is evolved by the Cauchy code. The vertical green line within the cylinder indicates the direction of coordinate time. The horizontal lines represent time slices. The details of the location of time slices depend on the gauge choice. The pink boundary of the cylinder depicts the worldtube from where the CCE is performed. The purple lines with unit slope illustrate the null characteristics along which the information on the worldtube is propagated to (the solid blue line) \mathcal{S}^+ . In our procedure of associating information in the source frame with the asymptotic frame, we identify all the points along a characteristic by an equivalence. The solid green line in the cylinder acts as a source to the waveform feature at τ_0 observed at \mathcal{S}^+ .

QNM frequency spectrum (with power-law tails that are usually very weak). Beyond this rough picture, the association of the specifics in the strong-field dynamics to the waveform is not well understood, especially during the merger and post-merger phases.

Understanding this association is crucial because several strong-field tests of GR rely on BH perturbation theory and thus, on identifying the perturbative regime in the waveform. These tests include the no-hair theorem test, consistency tests of the QNM spectrum with the inspiral parameters, and the area theorem test. The start of ringdown in the GW is mathematically ill-defined as damped sinusoids form an incomplete and non-orthogonal basis [103, 104]. Therefore, it is important that we validate the choices of start times in the data analysis of ringdown guided by the strong-field information, where the validity of perturbation theory can be better understood.

Conceptual challenges

Mathematically, GR being a non-linear theory does not allow for unambiguous localization of sources of GWs. However, to a certain extent, one expects that the dominant source of a particular feature in the wave zone be localizable to a relatively small region of the spacetime in the past light cone. For instance, studies like [114, 123] identify the dominant source for the peak of the waveform during the plunge of a test particle into a Schwarzschild BH with the particle crossing the light-ring.⁷ Furthermore, the last few cycles of the BBH GW signal are associated with the dynamics of a linearly perturbed BH [83, 124, 125]. However, one needs to bear in mind that these studies are performed using linear perturbation theory where such localizations are better defined. For example, if one adds a massive particle instead of a test particle in the former case and makes the problem non-linear, one would get some additional source contributions from self-force, thus making the source localization trickier.

In the case of BBH post-merger, identifying specific events as a source of the features in the waveform cannot be done unambiguously owing to the non-linear dynamics from merger. However, drawing intuition from analytical linear perturbation theory, we expect the region within the support of the analytical effective BH potential to contribute significantly to the waveform at \mathcal{I}^+ . Thus, we argue that even in a non-linear case, a small region in the spacetime around the BH containing the strong-field dynamics, can be associated as a dominant source of features in the GW.

Another challenge in performing this association is that the notion of simultaneity in GR

⁷The light-ring is the orbit of a massless particle around the BH, which corresponds to the peak of the BH potential located at $3M$ in Boyer-Lindquist coordinates for a Schwarzschild BH.

is not absolute, which means that all spacelike slicings of the spacetime are equally valid. In numerical simulations however, we have to make a gauge choice. In our case this choice is made by the Cauchy evolution code. The spatial features corresponding to a particular timeslice are gauge dependent. We choose to monitor the Kerrness on a spatial coordinate 2-sphere in the strong-field region, instead of computing a volume integral over the source region in a timeslice.⁸

We attempt to present a mathematically rigorous validation for the start time of RD. However, we caution the reader that this association may be affected by gauge choices, and in particular is dependent on the radius of the 2-sphere we monitor, especially in the strong-field region.

Forming a source-effect association via null characteristics

Given these challenges, we propose the following association scheme. We evaluate the Newman-Penrose scalar Ψ_4 , which measures the outgoing gravitational radiation, on a given slice of the simulation. Ψ_4 is obtained from the Weyl tensor as

$$\Psi_4 \equiv -C_{abcd}k^a\bar{m}^bk^c\bar{m}^d, \quad (4.18)$$

where k^a is a radially ingoing null vector, and the complex vector m^a is formed from spatial vectors orthogonal to the radially ingoing and outgoing null vectors (cf. [116] for more detail). By looking at Ψ_4 evaluated on the simulation, we infer a 2-sphere radius that lies within the strong-field region, containing and generating significant radiative fields. This 2-sphere acts like an effective source for the GW seen at \mathcal{I}^+ . We evaluate a surface integral of the Kerrness measures at each time slice during the ringdown on this 2-sphere. Then, we connect the evolution of the Kerrness measures on this surface to the associated features in the GW by following the outgoing null characteristics emanating from this 2-sphere. The details of this procedure are described below.

The GWs emanating from a source propagate to \mathcal{I}^+ along outgoing null rays (since the spacetime is curved, a small portion of GWs also travel inside the light cone). We utilize this in constructing an association between strong-field information and the features on the GW. We associate a feature on the GW to a 2-sphere in the strong-field region at a given time (in the simulation coordinates) if they lie on the same outgoing null hypersurface. This 2-sphere can thus be interpreted as an effective source producing the point on the waveform. The

⁸By doing so, the gauge effect is limited to uncertainty of picking the 2-sphere, thereby avoiding contribution of gauge effects through the entire volume region.

choice of 2-sphere should be close to the region generating GWs rather than farther out as we are interested in monitoring the region with a strong support of the BH potential. Measuring Kerrness of such a surface would give an insight into validity of perturbation theory in the region that acts as a dominant source of the GWs.

A framework that is naturally suited for such connections is Cauchy Characteristic Extraction (CCE). CCE foliates the spacetime into a family of outgoing null hypersurfaces and formulates Einstein's equations as an initial-boundary value problem in a 2+2 characteristic decomposition. The mathematical details of this formalism can be found in [126, 113]. CCE performs a characteristic evolution using the metric data on a timelike boundary of the Cauchy region (known as the worldtube) and propagates it to \mathcal{I}^+ . At \mathcal{I}^+ the radiation information is obtained as the Bondi news function \mathcal{N} [127]. The GW strain can then be obtained from \mathcal{N} by a time integration,

$$h(t) = \int_{-\infty}^t \mathcal{N}(t') dt'. \quad (4.19)$$

A key feature of this scheme is that each point at \mathcal{I}^+ corresponds to a null hypersurface, which in turn corresponds to a particular (coordinate) time label on the world tube.

We can thus associate the average of the Kerrness on a 2-sphere to spherical harmonic modes at \mathcal{I}^+ . We choose to average the quantities, rather than modally decompose them, in order to obtain a single number, which makes the interpretation and presentation of results easier. We illustrate this in Fig. 6. Here τ_0 marks a specific timeslice (horizontal solid green line) in the Cauchy evolution region in a gauge chosen by the Cauchy code. The intersection of this timeslice with the worldtube boundary is a spatial (topological) 2-sphere. The information on this 2-sphere is propagated to \mathcal{I}^+ along a null hypersurface labeled (solid purple line) as τ_0 . The radiation feature carries the time stamp τ_0 at \mathcal{I}^+ , which, roughly speaking, arises from the 2-sphere defined by the intersection of timeslice τ_0 and the worldtube in the simulation and thus, we identify them to be associated.

Having established a framework to associate information on a 2-sphere in the strong-field region to the waveform at \mathcal{I}^+ , we now discuss the choice of the 2-sphere used in this study. Motivated by analytical studies of test particles plunging into Schwarzschild BHs [114, 123], one might want to inspect the 2-sphere associated with the peak of effective BH potential. However, locating it during the merger in a numerical simulation is non-trivial (if at all well-defined), and is beyond the scope of this chapter. Furthermore, CCE cannot be performed from an arbitrarily small worldtube close to the horizon. This limitation arises

because CCE is formulated in light-cone coordinates. In the regions very close to the horizon, light-cone coordinates can form caustics, leading to coordinate singularities. Because of these constraints, we choose the worldtube radius corresponding to the smallest coordinate 2-sphere that is accessible to our procedure, but we visually verify that it contains strong-field dynamics by plotting Ψ_4 in Figs. 21.

4.2.3 Inferring perturbation amplitudes via Kerrness

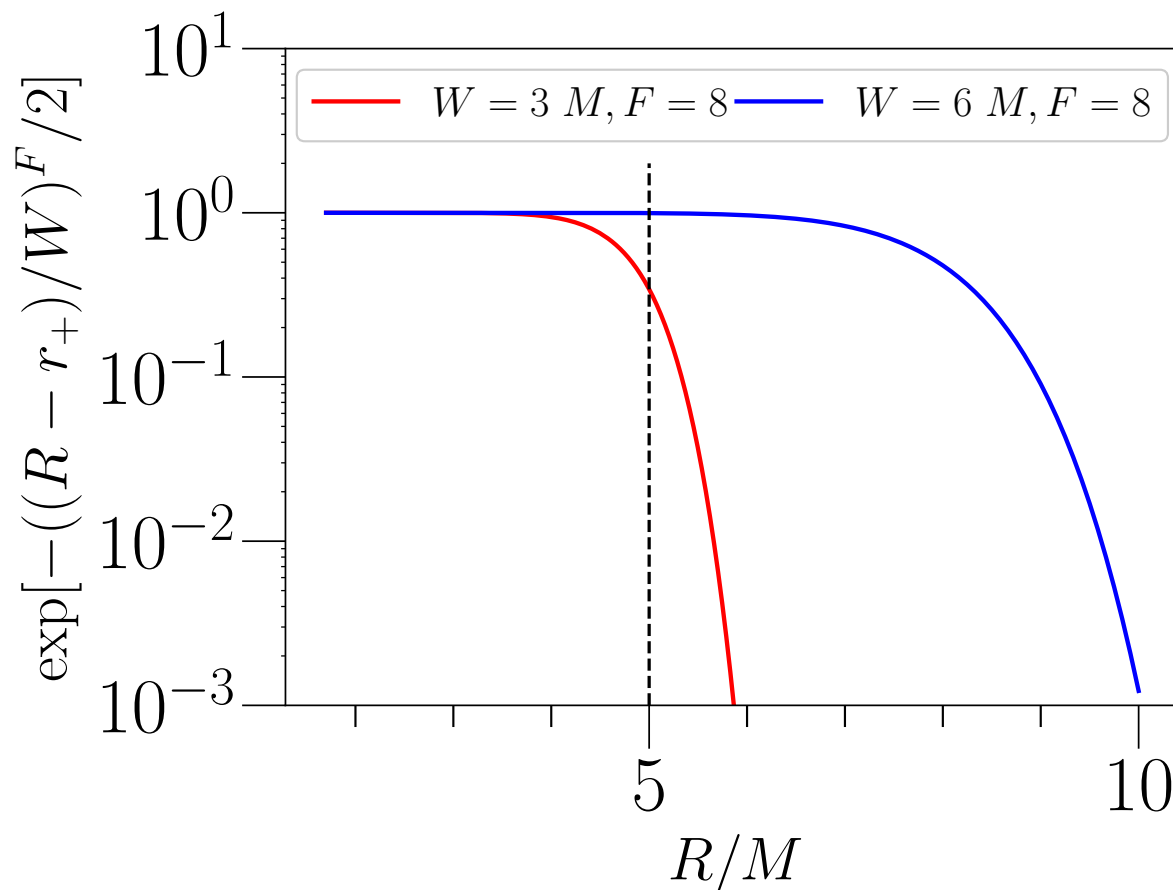


Figure 7: Envelope function from Eq. (4.21), for two choices of width and falloff parameters, $\{W, F\}$. We show how the envelope parameters affect an extraction radius of $R = 5M$ (marked by the dashed black line). For our chosen values of $\{W = 6M, F = 8\}$, the envelope is at ~ 1 and $R = 5M$, while for $\{W = 3M, F = 8\}$, the envelope affects the perturbation amplitude at $R = 5M$. We have checked that using a smaller envelope does not change the qualitative behavior of our results.

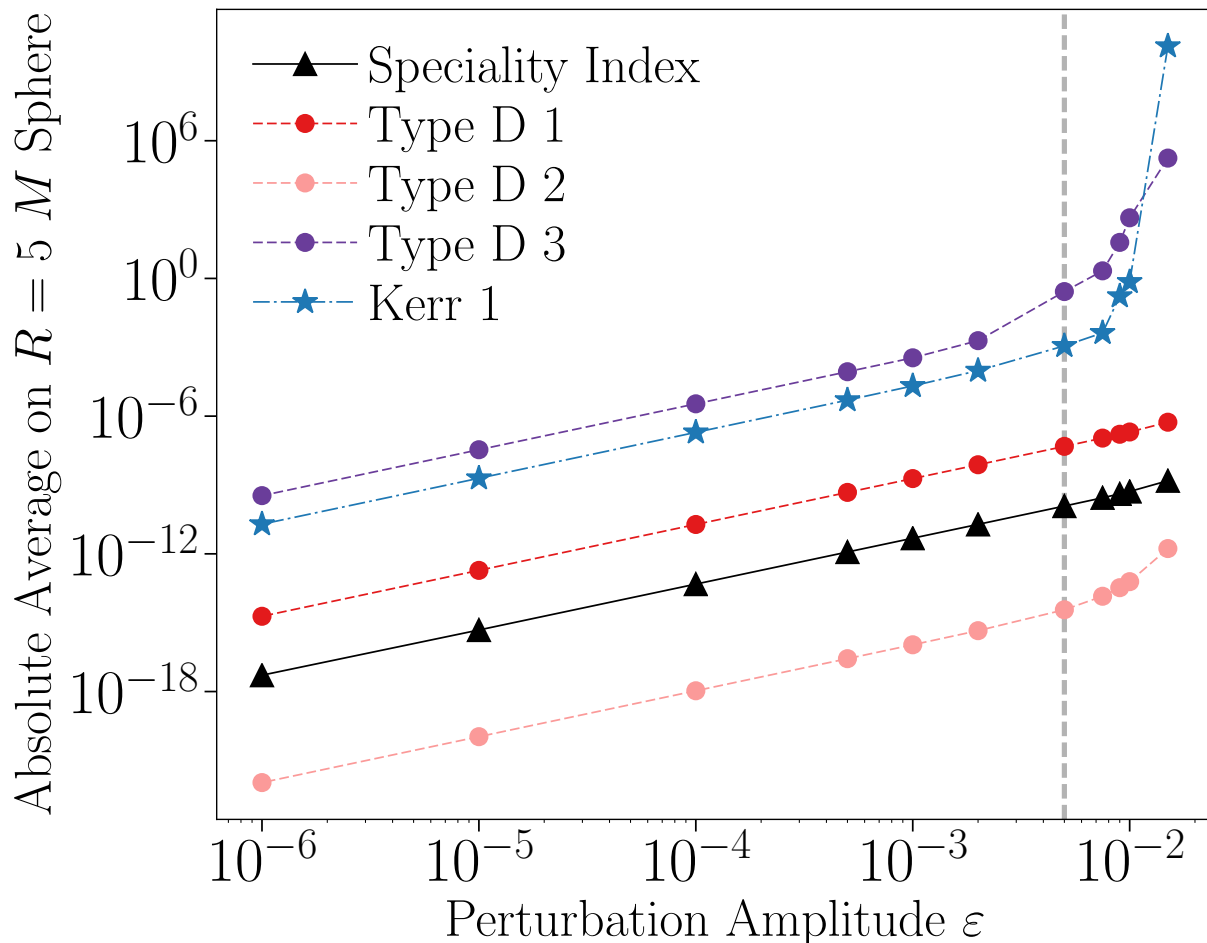


Figure 8: Behavior of absolute Kerrness measures with perturbation amplitude ε . We compute this on an $l = m = 2$ QNM perturbed Kerr BH with the same mass and spin as the final remnant in the BBH simulation we consider in this chapter. We average each measure on a coordinate 2-sphere of $R = 5M$. Note that we do not plot Type D 4 due to the high level of numerical noise in the measure, but it behaves similarly to Type D 3. The behavior is initially quadratic with ε for all measures. At larger amplitudes $\varepsilon \geq 5 \times 10^{-3}$, Type D 2, D 3, D 4 and Kerr 1 show higher-power dependence, and hence non-linearity. We show this $\varepsilon_{\text{crit}} \sim 5 \times 10^{-3}$ by a dashed vertical line. The lines between the points are only used to visually connect them (rather than being fits).

In order to give physical meaning to the values of the Kerrness measures outlined in Sec. 4.2.1, we can compare their values (on a post-merger spacetime, for example) to those on a single BH with a known analytic perturbation. Specifically, we can compare the Kerrness measures during ringdown to those on a $l = m = 2$ spheroidal QNM perturbed Kerr BH of the same final mass and spin, with varying dimensionless perturbation amplitude ε . This will provide a true physical comparison, as linearly-perturbed type D spacetimes are fully generic type I, and thus the Kerrness measures on the perturbed spacetime are expected to be nonzero [128]. This comparison will allow us to infer the perturbation amplitude to which a particular coordinate time corresponds. We can then map this inferred amplitude onto the waveform using the methods in Sec. 4.2.2.

Given the initial masses and spins, we can generate initial data for a perturbed BH (including all the relevant modes). In this study we choose to use the initial data consisting of only (2,2) mode as this is the dominant mode of the system. We have fitting formula for relative mode amplitudes in the perturbative regime, and thus we can extract an overall amplitude factor and call that ε .

Kerrness measures on perturbed metrics

The perturbed metric is generated on a single slice for each ε by solving the Teukolsky equation and reconstructing the metric perturbation h_{ab} using a Hertz-potential formalism [129, 130] (cf. [83] for a general review). The resulting perturbation h_{ab} is then added to the background metric to give

$$\tilde{g}_{ab} = g_{ab}^{\text{Kerr}} + \varepsilon h_{ab}, \quad (4.20)$$

which is correct to linear order. The constraint equations for the metric \tilde{g}_{ab} are then solved to give a fully constraint-satisfying metric g_{ab} in Kerr-Schild coordinates using the extended conformal thin-sandwich formalism (cf. [116]). This introduces some nonlinear effects into the perturbed metric. Furthermore, the asymptotic radial behavior leads to blow-up of the solution at large radii [131]. Thus, before solving for g_{ab} , we multiply h_{ab} by an envelope of the form

$$f_{\text{Envelope}}(R) = \exp[-((R - r_+)/W)^F/2], \quad (4.21)$$

where r_+ is the radius of the outer horizon of the BH, W is the width, and F is the falloff of the envelope. Since the mapping of the Kerrness measures onto the waveform occurs at $R = 5M$, as will be discussed in Sec. 4.3.3, and the horizon typically has outer radius

$R_+ \sim 1.7 M$, we choose $W = 6 M$ to give $f_{\text{Envelope}}(5 M) \sim 1$ so as to minimally affect the perturbation at the extraction radius. Additionally, we choose $F = 8$ in order to counteract the steep growth of the perturbation with radius. We plot the envelope in Fig. 7. In practice, the metric perturbation is generated using an extension of the code used in East et al. [132], but with the QNM solution rather than an ingoing GW solution and using the full radial dependence.

Fig. 8 shows the behavior of the Kerrness measures averaged on a 2-sphere of $R = 5 M$ with ε on a BH of the same final mass and spin as the simulation outlined in Sec. 4.3.1. The theoretical behavior of the Kerrness measures with perturbation amplitude is unknown [122, 133], and thus this is the first (numerical) computation of the behavior. We first check that the measures converge to finite values with numerical resolution, thus representing real physical values. The Kerrness measures increase quadratically for small ε , then show higher-order effects for large ε . Type D 2 grows to (best-fit) quartic, Type D 3 and Kerr 1 become cubic, while Speciality and Type D 1 remain quadratic at $\varepsilon \sim 10^{-2}$, the largest amplitude for which we can solve for g_{ab} before violating the constraints. In particular, the steep increase of the Type D 3 and Kerr 1 measures, which come from geometric conditions on KVs, indicates that at large enough perturbation amplitude, the slice fails to have even an approximate KV. Since the perturbation we are introducing is not axisymmetric, it makes sense that at large ε the slice loses this KV symmetry.

The linear perturbation regime corresponds to the region where the measures increase quadratically with ε , while the non-linear regime approximately begins where one can see higher-power behavior. In this case, we see the transition from quadratic behavior around $\varepsilon_{\text{critical}} \sim 5 \times 10^{-3}$, suggesting that this is the approximate start of the nonlinear regime. In practice, one can normalize all of the ε values in this chapter by $\varepsilon_{\text{critical}}$. However, we do not do this for readability of the figures.

However, there are some sources of error in the g_{ab} analysis. The areal radius of the perturbed metric on a coordinate 2-sphere of radius $R = 5 M$ changes slightly with perturbation amplitude, changing by $10^{-2} M$ between $\varepsilon = 10^{-6}$ and 10^{-2} . Thus, a coordinate-radius measure comparison does not happen on exactly the same 2-sphere. Solving for g_{ab} changes the values of the mass and spin from the parameters used in creating g_{ab}^{Kerr} . At the largest perturbation amplitude $\varepsilon = 10^{-2}$, the dimensionless spin changes by .003, while the mass changes by .008 M . We keep these errors in mind when computing the Kerrness values of the strong-field region in terms of ε and mapping them to the waveform for the binary case in Sec. 4.4.3.

Mapping onto the waveform

A perturbation amplitude ε is associated with each timeslice of a post-merger spacetime in the strong-field region by the procedure described above. Since the procedure developed in 4.2.2 allows us to associate simulation timeslices with the gravitational waveform at \mathcal{S}^+ , we can map the perturbation amplitude associated with each timeslice to the corresponding parts of the waveform at \mathcal{S}^+ . This gives an insight into deciding which portion of the waveform at \mathcal{S}^+ can be modeled as being generated by linearly perturbed Kerr manifold, thus providing validation of start times chosen in data analysis that rely on perturbative description of Kerr.

4.2.4 Outline of method

For quick reference, we now concisely provide an outline of the algorithmic procedure developed in this chapter. This also serves as a step-by-step plan that we can apply to future BBH detections.

1. Performing an NR simulation with waveform parameters inferred from parameter estimation, and saving the metric data,
2. Generating worldtube data for various extraction radii and performing CCE from the inner-most possible radius,
3. Evaluating the Kerrness measures on the metric data at this radius for BBH ringdown,
4. Evaluating the Kerrness measures on QNM perturbed data with the same final mass and spin, and inferring corresponding perturbation amplitude from the Kerrness values,
5. Mapping the Kerrness measures and inferred perturbation amplitudes to the waveform via null-characteristics,
6. Using these results to validate choices for the start time of ringdown in detector data analysis.

4.2.5 Measuring Kerrness on the horizon

In addition to local measures throughout a spatial slice discussed in Sec. 4.2.1, Kerrness can also be evaluated on the post-merger apparent horizon (AH). Owen describes a multipolar horizon analysis in [4], finding that the multipolar structure of a final BBH remnant was that of Kerr. Probing the multipolar structure also serves as a test of the no-hair theorem [83].

This formalism involves computing the mass multipole moments I_α of the horizon as

$$I_\alpha = \oint y_\alpha R dA, \quad (4.22)$$

where R is the scalar curvature of the horizon, dA is the metric volume element on the AH, and α labels generalized (non-axisymmetric) scalar spherical harmonics y_α . These generalized spherical harmonics are computed from the eigenvalue problem

$$\Delta y_\alpha = \lambda(\alpha) y_\alpha, \quad (4.23)$$

where Δ is the operator $\Delta \equiv g^{AB} \nabla_A \nabla_B$ on the AH, and λ is its eigenvalue. In analogy with axisymmetric spherical harmonics Y_{lm} , an effective l is defined for the eigenvalues as

$$\lambda = -\frac{l_{\text{eff}}(l_{\text{eff}} + 1)}{r^2}, \quad (4.24)$$

where r is the areal radius of the horizon. Since the l_{eff} values are time-dependent, we refer to a given multipole by its final value.

As discussed in [4], the multipole moments that are zero on a Kerr BH either immediately vanish due to the symmetry of the AH, or decay to zero from their excited values as the remnant BH settles to Kerr. The multipole moments that do not vanish on Kerr are functions of the mass and spin, and reach these values with increasing coordinate time. We use the code implemented and tested in [4] to compute the multipole moments. However, since the multipole moments are features of the horizon, we cannot map their behavior onto the waveform at \mathcal{I}^+ . Moreover, CCE cannot be performed close to the horizon, as discussed in Sec. 4.2.2. Nevertheless, we can compare the qualitative behavior of the multipole moments with those of the Kerrness measures as done in Secs. 4.4.1 and 4.4.2.

4.3 Numerical implementation

4.3.1 Description of simulation

We apply the methods outlined Sec. 4.2 to the numerical simulation presented in Fig. 1 of [134], with similar parameters to GW150914, the first LIGO detection. The simulation is performed and the methods are applied using SpEC, the Spectral Einstein Code. The waveforms and parameters are available in SXS:BBH:0305 in the SXS Public Catalog [135]. The simulation has initial mass ratio $q = 1.221$, and dimensionless spins $\chi_A = (0, 0, 0.33)$ and $\chi_B = (0, 0, -0.44)$. The initial orbital frequency is $\Omega_0 = 0.017$. The final (post-merger) BH has dimensionless spin $\chi_C \simeq (0, 0, 0.69)$ (within numerical error, as measured using the

techniques in [107]) and mass $0.952 M$. The inspiral proceeds for $3694.4 M$ until the formation of a fully-resolved common AH. The visible part of the post-merger waveform on a linear scale has a temporal duration of $\sim 61 M$.

Within a BBH simulation, the metric equations are evolved in a damped harmonic gauge [136, 137], with excision boundaries just inside the apparent horizons [138, 139], and minimally-reflective, constraint-preserving boundary conditions on the outer boundary [140]. The spectral grid used during the inspiral of the simulation has an excised region for each BH. Once a common AH forms, the simulation proceeds for a few M before switching to a new grid, in which there is one excision region for the new AH [138]. For this simulation, the grid-switch happens at $3696.9 M$. For more information on the code, see [141].

4.3.2 Implementation of Kerrness measures

We discuss the numerical implementation of the Kerrness measures outlined in Sec. 4.2.1, and summarized in Fig. 5, on an NR BBH post-merger. Note that these measures will not be zero even on a numerical Kerr spacetime, due to the resolution of the simulation.

In order to quantify the Kerrness measures at each point, we convert the complex tensors into scalars. We contract a tensor A^{ij} , a vector B^i , and a scalar C as

$$S_A = A^{ij} \bar{A}_{ij} \quad S_B = B^i \bar{B}_i \quad S_C = C \bar{C}, \quad (4.25)$$

where raising and lowering occurs using the spatial metric γ_{ij} .⁹ Throughout the rest of the chapter, all of the measures will refer to their respective scalars generated using Eq. (4.25).

Because our simulations are performed using spectral methods, we expect errors to converge exponentially with increasing numerical resolution [142]. In Fig. 9, we plot the Kerrness measures as a function of resolution for a single Kerr black hole; we see that the measures decay exponentially towards zero as expected.

SpEC solves a first-order formulation of the Einstein equations, and therefore evolves both the spacetime metric and variables corresponding to its time and spatial derivatives [143]. The metric and first derivatives are available to the accuracy of the numerical simulation on each slice. Kerrness measures that require additional numerical derivatives, however, will have greater numerical noise and a higher numerical noise floor. The highest numerical order derivative needed to evaluate each measure is given in Fig. 5. Type D 4, which requires four

⁹The Kerr 2 measure given in Eq. (4.16) requires that the imaginary part be zero, while the real part be ≥ 0 . Hence, when evaluating Kerr 2, we measure the deviation of the imaginary part from zero, and the deviation of the real part from being positive (hence only including negative values).

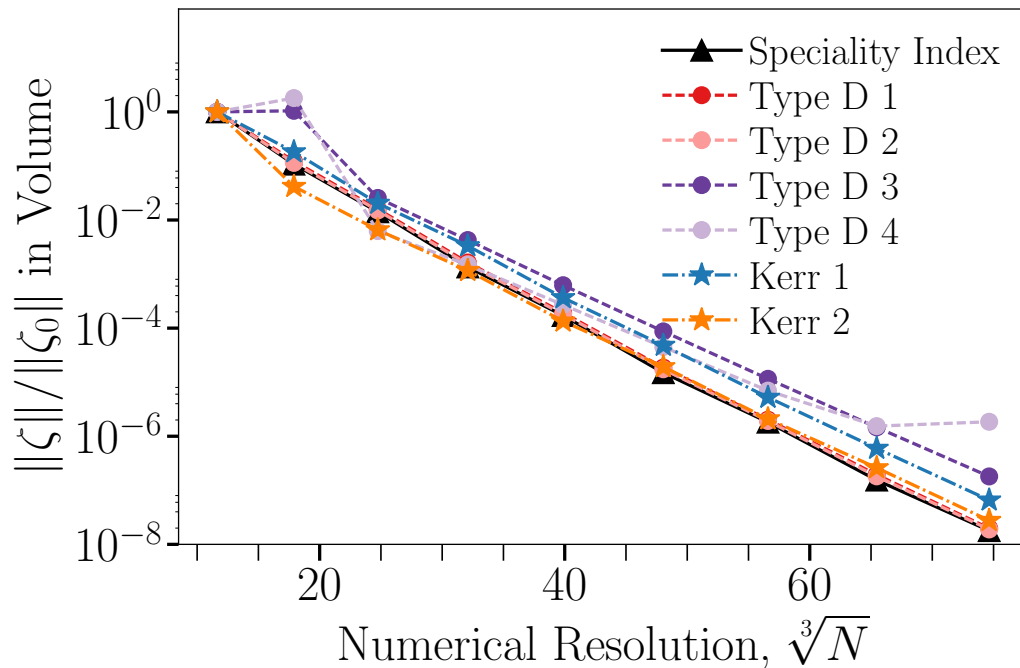


Figure 9: Convergence of Kerrness measures on a numerical BH in Kerr-Schild coordinates with dimensionless spin $\chi = (0.2, 0.3, 0.4)$. We observe exponential convergence towards the theoretical value of zero with numerical resolution. For each measure ζ , we present $\|\zeta\|/\|\zeta_0\|$, the L2 norm over the spatial slice normalized by the L2 norm of the lowest resolution. The resolution is expressed $\sqrt[3]{N}$, where N is the number of spectral collocation points in the domain.

numerical derivatives, is the noisiest measure and has a higher noise floor than the other measures, as shown in Fig. 9.

4.3.3 Map from source to \mathcal{S}^+ - implementation

In our study, we use a CCE implementation in SpEC (cf. [144], in prep). This implementation uses a no ingoing and outgoing radiation condition on the initial null hypersurface of the characteristic evolution. This means that the code treats the spacetime outside the worldtube as initially free of any gravitational radiation from the past.¹⁰ Usually the CCE worldtube is placed at a large radius, and the CCE evolution begins at the start of the numerical simulation during early inspiral. However, here we begin CCE only at the merger portion of the Cauchy evolution, and in addition, we place the CCE worldtube at a very small radius. This means that extracted waveform does not contain contribution coming from the inspiral part of the dynamics.

By decreasing the radius of the extraction worldtube progressively by $1 M$, we find the smallest radius of the worldtube that our procedure can be applied to occurs at a coordinate radius of $R = 5 M$. For a radius of $R = 3 M$, the CCE procedure can not be performed, presumably due to the formation of caustics. At $R = 4 M$, we get a very glitchy and unreliable extraction of the news function.

However, performing the CCE from such small radii gives rise to an additional complication. Since time stamps on the waveform at \mathcal{S}^+ are induced by the simulation coordinates, the news function obtained is not necessarily in an inertial gauge. In a standard CCE scheme, a gauge transformation is applied to the news function in order to obtain it in an inertial gauge. To preserve the map between the time in simulation gauge and the time coordinate on the extracted news function, we do not perform this gauge transformation. We see the effect of the gauge transformation in the waveform at \mathcal{S}^+ as a mixing of mode amplitudes. The effect is very small when the worldtube boundary for CCE is large i.e., lies in the weak field region. For instance, for a worldtube boundary of $R = 128 M$ the effect of this transformation is negligible. To confirm this, we compute the overlap \mathcal{O} between the news extracted from $R = 128 M$ with and without the gauge transformation. The overlap \mathcal{O} is defined as,

$$\mathcal{O} = \langle \tilde{\mathcal{N}}_1 | \tilde{\mathcal{N}}_2 \rangle = \int_{-\infty}^{\infty} \frac{\tilde{\mathcal{N}}_1(f) \tilde{\mathcal{N}}_2^*(f)}{|\tilde{\mathcal{N}}_1| |\tilde{\mathcal{N}}_2|} df, \quad (4.26)$$

¹⁰During the Cauchy evolution, we perform the evolution with a boundary of $R \approx 670 M$ and we do not neglect the backscatter from the region outside of the CCE extraction radius.

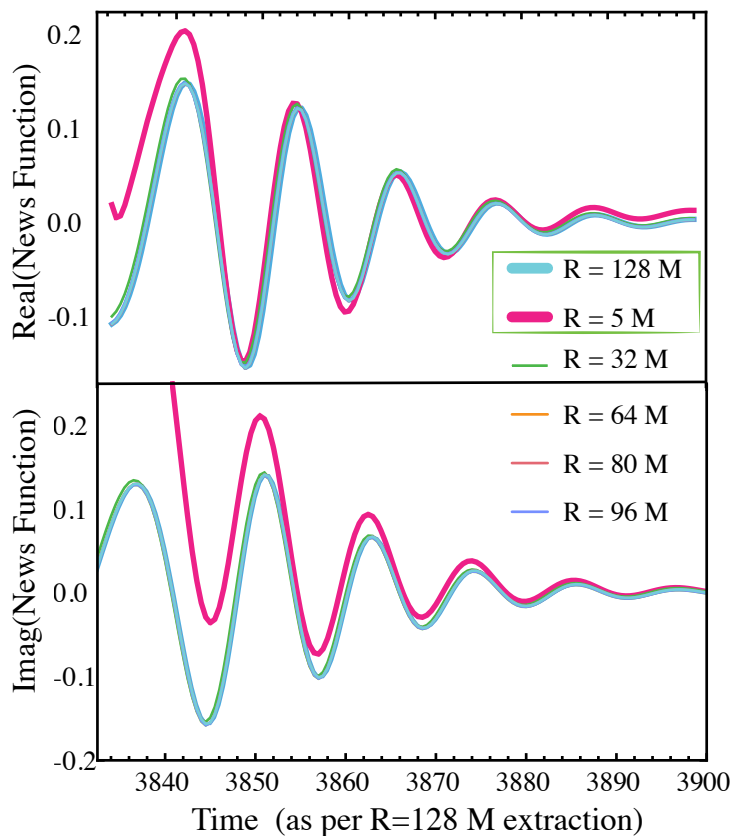


Figure 10: The $l = m = 2$ mode of the news function seen at \mathcal{S}^+ extracted from worldtube boundaries of $R = 5 M$, $32 M$, $64 M$, $80 M$, $96 M$ and $128 M$. The horizontal axis corresponds to the time stamps associated with the news function corresponding to CCE from $R = 128 M$. The **top panel** shows the real part and the **bottom panel** shows the imaginary part of the news function. The alignment of news functions has been done such that the overlap is maximized. The transformation that changes the gauge from a non-inertial to an inertial observer has not been applied to any of the extractions. All of the extractions beginning with $R = 32 M$ seem to agree with one another (to the point of overlapping with the $R = 128 M$ line). Notice that the amplitude of the news function extracted from $R = 5 M$ deviates from the other extractions, especially in the first cycle. Nevertheless, the phase evolution between the news function from extraction radii seem to agree. The primary goal of this figure is to compare the extracted waveforms at $R = 5 M$ and $R = 128 M$. Thus we have bolded and boxed these lines.

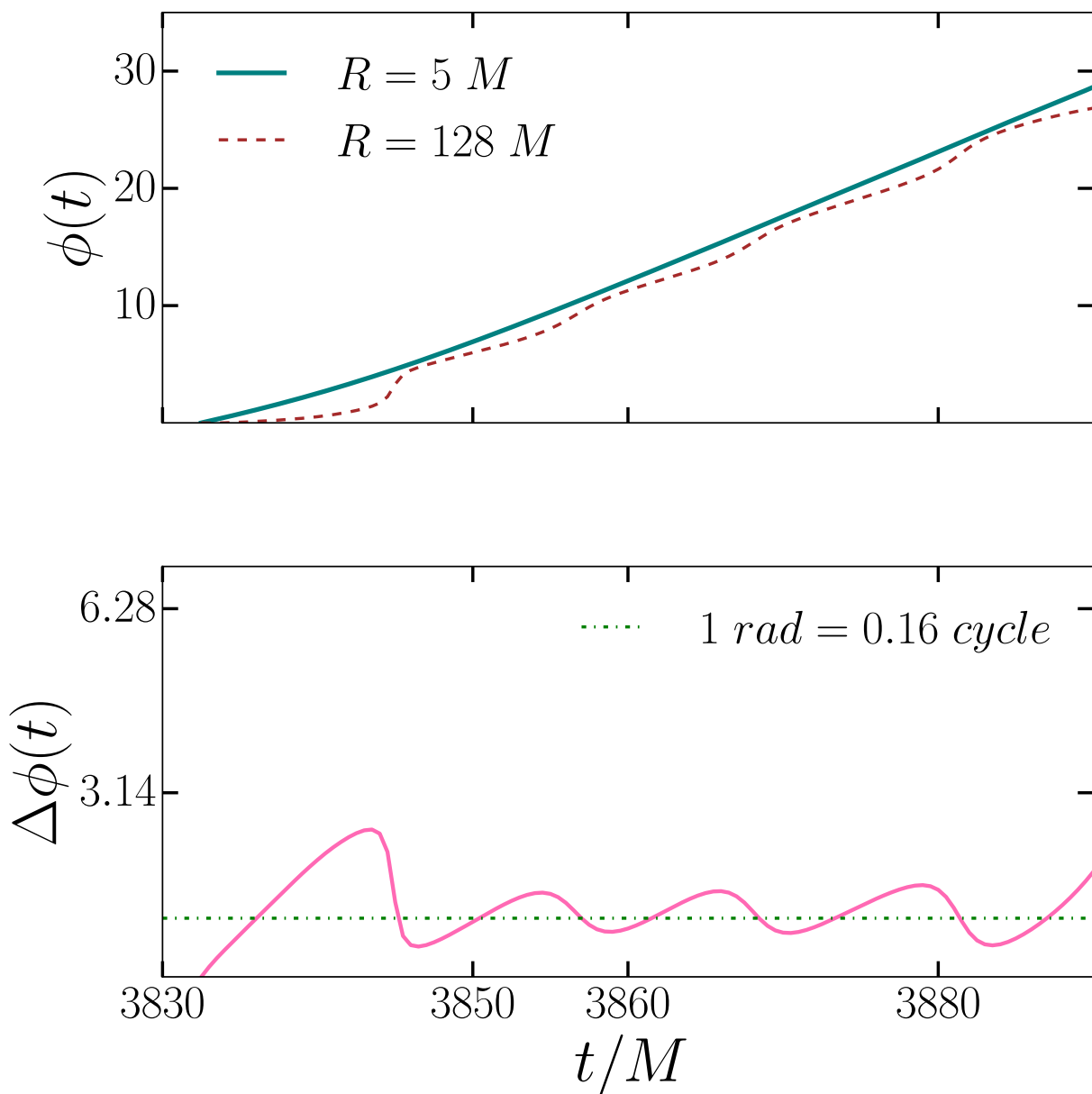


Figure 11: The phase discrepancy between the news function extracted from a worldtube radius of $R = 5M$ and $R = 128M$. The news functions are aligned to maximize the overlap. The **top panel** presents the phase evolution of the news function for each extraction radius. The **bottom panel** shows the fractional difference defined as $\phi_{128} - \phi_5$. Notice that the phase difference is significant at the very beginning but quickly decreases to an acceptable level for our analysis. We notice that the phase difference oscillates about 1 radian, indicating the level of error we introduce by - a) not performing the final gauge transformation, b) imposing no-ingoing condition for CCE.

where $\tilde{\mathcal{N}}_{1,2}$ is the frequency domain Fourier-transformed news function, and $*$ denotes complex conjugation for ease of readability, and $||$ is the norm [145].

We find that the mismatch, $1 - \mathcal{O}$, is $\sim 10^{-6}$. This overlap computation uses only the merger and post-merger parts of the news function for the dominant ($l = m = 2$) spin-weighted spherical mode. However, for a worldtube radius of $R = 5M$, there could be significant amplitude deviations between the waveforms in the simulation-coordinate-induced gauge and the inertial gauge. Because of technical difficulties in the code implementation, we could not apply the gauge transformation to an extraction from $R = 5M$ and quantify the difference.

Furthermore, before the non-inertial to inertial gauge transformation, every point on \mathcal{S}^+ at the same timestamp on the waveform corresponds to the same null hypersurface and therefore to the same simulation coordinate time. After the transformation, this is no longer true: the waveform seen at different sky directions with the same timestamp on the waveform corresponds to different null hypersurfaces and therefore different values of simulation coordinate time. This happens because the choice of the 2-sphere is gauge-dependent. Therefore, we omit the gauge transformation, as the aim in this chapter is to connect the near-zone to the wave zone, requiring us to retain the timestamps.

Additionally, the initial no-ingoing radiation condition neglects gravitational radiation coming from the inspiral. This may be significant for extraction done at small radii, where the initial CCE null hypersurface connects the strong-field region close to merger to \mathcal{S}^+ and may contain significant radiation from the inspiral. This could contribute towards the discrepancy between the $R = 128M$ and $R = 5M$ waveforms.

To assess this difference, we compare the news function obtained by extraction performed from $R = 5M$ with the extractions performed from the worldtubes of larger radii, all without the gauge transformation. The result of this is presented in Figure 10. We observe that all the extractions from radii greater than $32M$ converge with radius, indicating that the effect of the gauge transformation is insignificant at these radii. Further, the extraction from $R = 5M$ has a significant amplitude discrepancy with the other extractions, particularly in its first cycle. Therefore, we would ideally wish to map the strong-field information computed on the 2-sphere at a coordinate radius of $R = 5M$ on the news function that has been extracted from a larger radius like $R = 128M$.

We do this mapping in two steps. First, we map the strong-field information computed on the 2-sphere at a coordinate radius of $R = 5M$ onto the CCE performed from a worldtube of $R = 5M$ using the framework described above. Next, we note that the phase evolution of

extraction from $R = 5 M$ agrees with the extractions from larger radii.¹¹ We verify this in Fig. 11. Then we align the news function extracted from $R = 5 M$ to the extraction from larger radii as shown in Fig. 10. The alignment is done such that the overlap \mathcal{O} between the CCE extracted news function from different world tube radii is maximized. The maximum normalized \mathcal{O} between the news function extracted from $R = 128 M$ and $R = 5 M$ is 0.82. Incidentally, this alignment is equivalent to aligning the real part of the news function at its global minima (or global maxima of the absolute value). Table 4 lists the time shifts that have been applied in order to align the news function extracted from a radius R_i with extraction done at $R = 128 M$.

Worldtube radius	Alignment shift wrt $R = 128 M$
$R = 5 M$	$132.5 M$
$R = 32 M$	$96.5 M$
$R = 64 M$	$62.5 M$
$R = 128 M$	$0 M$

Table 4: The shift in the time axis performed to align the news functions extracted from different radii in Fig. 10. The alignment has been done such that the overlap between the news function extracted from different worldtube radii with the extraction from $R = 128 M$ is maximized.

Using this alignment we map the time stamps on the $R = 5 M$ to those on $R = 128 M$. From this, we infer the mapping of strong-field information at $R = 5 M$ on to the extraction done from $R = 128 M$, thus mapping the strong-field information onto the news function as seen in near inertial gauge.

We summarize our algorithm for mapping the strong-field information onto the news function:

1. Perform CCE from worldtube with radius of the 2-sphere that lies in the strong-field region (whose evolution you wish to map on to the news function seen at \mathcal{I}^+) without the final non-inertial to inertial gauge transformation. The time stamps on this extracted news function are induced by the time coordinates in the simulation, thus providing a natural map between the evolution of the strong-field region and the wave zone.
2. Perform CCE from a large worldtube radius where the effect of the non-inertial to inertial gauge transformation is negligible.

¹¹The time-derivative of the phase gives the instantaneous frequency of the gravitational radiation.

3. Align the news functions obtained in steps 1 and 2 such that the overlap between the waveform is maximized.
4. Use this alignment to map the time stamps of the news function extracted in step 1 to that in step 2. The 2-sphere chosen in step 1 at the timeslice marked with the simulation time coordinate can be associated as the dominant source of the feature at \mathcal{I}^+ with the same time stamp.

4.4 Results

We now present the results of performing the analysis outlined in Secs. 4.2 and 4.3 on the GW150914-like simulation detailed in Sec. 4.3.1. Sec. 4.4.1 presents the behavior of the multipole moments of the AH, which provides a comparison for the Kerrness measures on the simulation volume. Sec. 4.4.2 discusses the results of evaluating the Kerrness measures on the post-merger spacetime and mapping them onto the waveform at \mathcal{I}^+ , presenting them in terms of the percentage decrease from their peak values. Sec. 4.4.3 presents the results of comparing the Kerrness measures on the post-merger spacetime to values on perturbed data, in order to infer the perturbation amplitude in the strong-field region, and mapping them onto the waveform, presenting them in terms of the inferred perturbation amplitude ε . The percentage decrease from the peak value and ε can then be used to estimate the overall level of Kerrness and validate choices for the start time of ringdown. Finally, in Sec. 4.4.4, we discuss the implications of these results on analyzing ringdown in GW data, and in Sec. 4.4.5 we compare our results to the ringdown start times chosen in the GW150914 testing GR study [5].

4.4.1 Horizon behavior and multipolar analysis on BBH ringdown

As a first measure of Kerrness, we apply the horizon multipolar analysis outlined in [4] and summarized in Sec. 4.2.5 to the simulation described in Sec. 4.3.1. Fig. 12 presents the behavior of the AH. The areal mass of the AH, given by $\sqrt{A/16\pi}$ where A is the proper area of the AH, sharply settles to a final value. The minimum and maximum radii are initially noisy, as the AH is initially peanut shaped, but they decrease exponentially with coordinate time, showing a settling of the AH to the final state. However, the radii are coordinate-dependent measures, and thus to check if the BH settles to Kerr it is more instructive to look at the AH multipole moments.

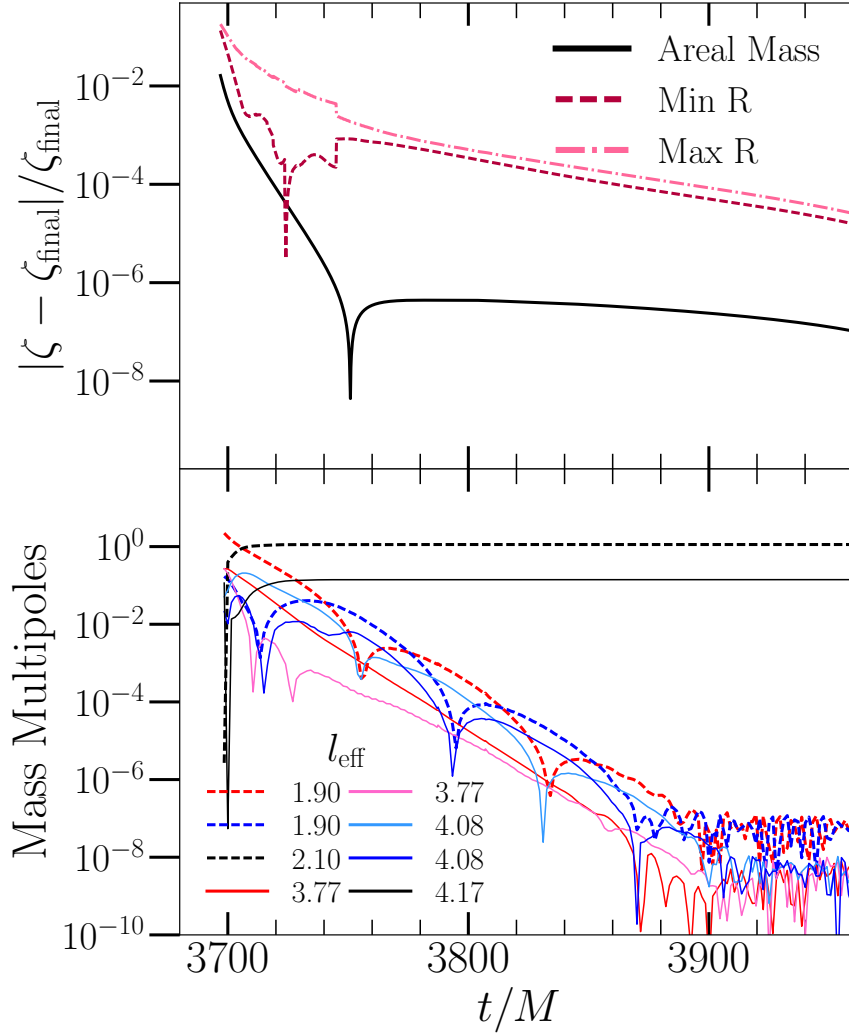


Figure 12: Settling of the post-merger AH as a function of coordinate time. The **top panel** shows the areal mass quickly attaining a constant value and the minimum and maximum radii R of the horizon exponentially settling to final values. Each quantity ζ is presented as $|\zeta - \zeta_{\text{final}}|/\zeta_{\text{final}}$ where ζ_{final} is the value at the final time of the simulation. The **bottom panel** shows the behavior of the initially excited AH mass multipoles, labeled by the l_{eff} given in Eq. (4.24) at the final time. The initially excited quadrupole moments ($l_{\text{eff}} \sim 2$) are shown by the dashed lines, while the initially excited hexadecupole moments ($l_{\text{eff}} \sim 4$) are shown by the solid lines. As discussed in the text, two of the quadropole moments and four of the hexadecupole moments, as well as the $l \sim 1$ and $l \sim 3$ moments immediately vanish due to symmetry. Thus, we do not plot them in this figure. The excited multipoles either exponentially decay or reach constant values consistent with the values expected for Kerr [4].

Fig. 12 shows the behavior of the initially non-vanishing quadrupole and hexadecupole moments, labeled by their corresponding l_{eff} at the final time, as given in Eq. (4.24). The quadrupole moments correspond to $l_{\text{eff}} \sim 2$ and the hexadecupole moments correspond to $l_{\text{eff}} \sim 4$. The multipole moments behave as expected for a generic simulation remnant settling to a Kerr BH. As explained in [4], two of the five quadrupole moments immediately vanish by reflection symmetry, while two others exponentially go to zero (eventually hitting a numerical noise floor) as the final remnant settles to Kerr. Four of the nine possible hexadecupole moments immediately vanish from reflection symmetry, while four go exponentially to zero as the remnant settles to Kerr. Note that the $l = 1$ and $l = 3$ moments vanish on Kerr due to symmetry. As in [4], one quadrupole moment ($l_{\text{eff}} = 2.1$) and one hexadecupole moment ($l_{\text{eff}} = 4.17$), both corresponding to $m = 0$, do not vanish, but rather attain a constant value in line with that of a Kerr BH of the same final mass and spin.

The multipolar behavior thus confirms that the final state of the AH is that of a Kerr BH. This serves as an independent test of Kerrness, and thus one would expect the Kerrness measures presented in Sec. 4.2.1 to also show the strong-field region exponentially settling to Kerr. This also serves as numerical evidence for BH uniqueness, as the final remnant of a BBH merger is indeed Kerr, as also discussed in [4]. Similarly, since the final multipolar structure can be described completely by the mass and spin, this serves as numerical validation of the no-hair theorem.

4.4.2 Measuring and mapping Kerrness onto the waveform

The goal in this section is to validate choices of the start time of ringdown using Kerrness measures on the GW150914-like system described in Sec. 4.3.1. We now present the results of evaluating the Kerrness measures outlined in Secs. 4.2.1 and 4.3.2 (and summarized in Fig. 5) in the strong-field region and mapping them onto the waveform at \mathcal{S}^+ using the procedure given in 4.3.3. These measures are evaluated point-wise on each slice, and we map the value on a 2-sphere at a radius of $R = 5M$ onto the news function. Recall that larger values of the Kerrness measures indicate greater deviation from being locally isometric to Kerr.

Fig. 13 shows the Kerrness measures averaged at various coordinate radii on each slice of the post-merger spacetime, presented as a function of coordinate time. All of the measures decay exponentially toward zero, showing that the spacetime approaches an isometry to Kerr. This confirms the results of the multipolar analysis in Sec. 4.4.1. Additionally, this serves as a numerical verification of BH uniqueness, as the final state of a BBH merger is isometric to Kerr. The behavior of the measures at large radii (such as $R = 128M$ in this case) is

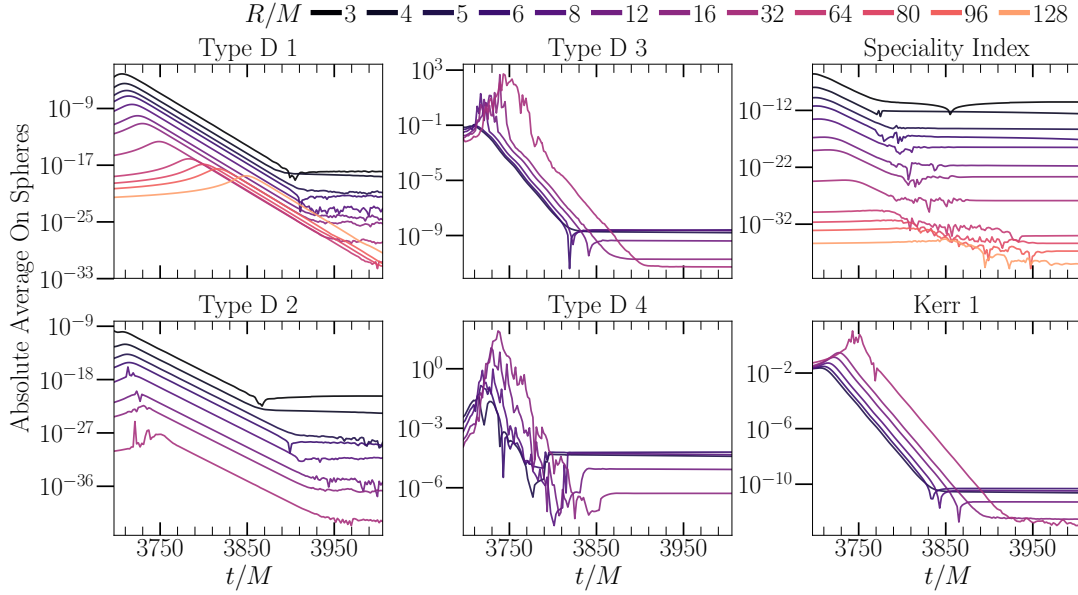


Figure 13: Behavior of absolute Kerrness measures with coordinate time on BBH post-merger spacetime. The measures are averaged on a variety of concentric nested coordinate 2-spheres of radii R around the BH, as indicated by the colors. Larger values *within each subplot* mean that the 2-sphere is farther from being locally isometric to Kerr. For measures that involve higher-order numerical derivatives, we present the results only at radii where they are at least somewhat well resolved. All plots, however, include $R = 5M$, the radius we use to map Kerrness onto the waveform. Type D 4 is particularly noisy, as it contains the highest number of numerical derivatives. The measures exponentially decay as the spacetime approaches Kerr, ultimately reaching a numerical noise floor. We observe that the peak of each measure moves outwards with radius, indicating propagation of non-Kerrness.

especially interesting to the question of BH uniqueness, which is particularly concerned with the *domain of outer communication* [133].

Fig. 14 shows the behavior of the Speciality Index, an algebraic measure (Type D 1) and a geometric measure (Kerr 1) in the volume, as a function of increasing coordinate time. We see a distinct quadrupolar pattern in all our measures (the equatorial plane has a modal pattern that corresponds to $|m| = 2$), consistent with the dominant mode of gravitational radiation. Furthermore, the Speciality Index and Type D 1 measures, which determine properties of the PNDs, settle first further from the BH, while the geometric Kerr 1 measure, which is determined by properties of the KV, first settles closer to the BH.

The Kerr 2 measure, which constrains the NUT parameter, is effectively constant throughout the ringdown, as shown in Fig. 15. Since the NUT parameter is one of the hairs of a generic type D manifold, Fig. 15 confirms that a NUT charge is not generated during a BBH merger. We thus do not include it further in our analysis.

Of these measures, two are algebraic constraints—Type D 1 and Type D 2—and three are geometric constraints on the KV, Type D 3, Type D 4, and Kerr 1. In Fig. 13 we see that all the algebraic measures decay in a similar fashion and all the geometric measures decay similarly. Type D 4, which requires 4 numerical derivatives, is visibly noisier than the other measures. This measure checks if the vector identified as (Y, Y_j) satisfies the Killing equation and is crucial for a rigorous mathematical characterization of Kerr manifold. However, all geometric measures depend on the same Killing vector and we observe that Type D 4 has a similar decay property as Type D 3 and Kerr 1. Thus, we do not include the noisier Type D 4 in our analysis, rather treating Type D 3 as a proxy for both.

Each measure at each radius in Fig. 13 eventually reaches a floor. This is confirmed to be a numerical noise floor in Fig. 16, where the floor is shown to exponentially converge to zero with numerical resolution. The radial behavior of the Kerrness measures stems from the radial behavior of the Weyl tensor and the metric quantities. For example, for a stationary background, $E_{ij} \sim R^{-3}$ and $B_{ij} \sim R^{-4}$, and thus Speciality Index given in Eq. (4.7) should be $\sim R^{-18}$, which we indeed observe.

The analysis outlined in Sec. 4.3.3 requires the Kerrness measures to be extracted at $R = 5M$ in order to map them to the news function. Fig. 14 shows that the Kerrness measures have strong support at $R = 5M$, thus justifying the choice of radius as being in the near field.¹²

¹²The measures at $R = 3M$ in Fig. 13 behave similarly to those at $R = 5M$ indicating that $R = 3M$ also behaves like the near field region, but unfortunately we have not been able to perform CCE from this small a radius.

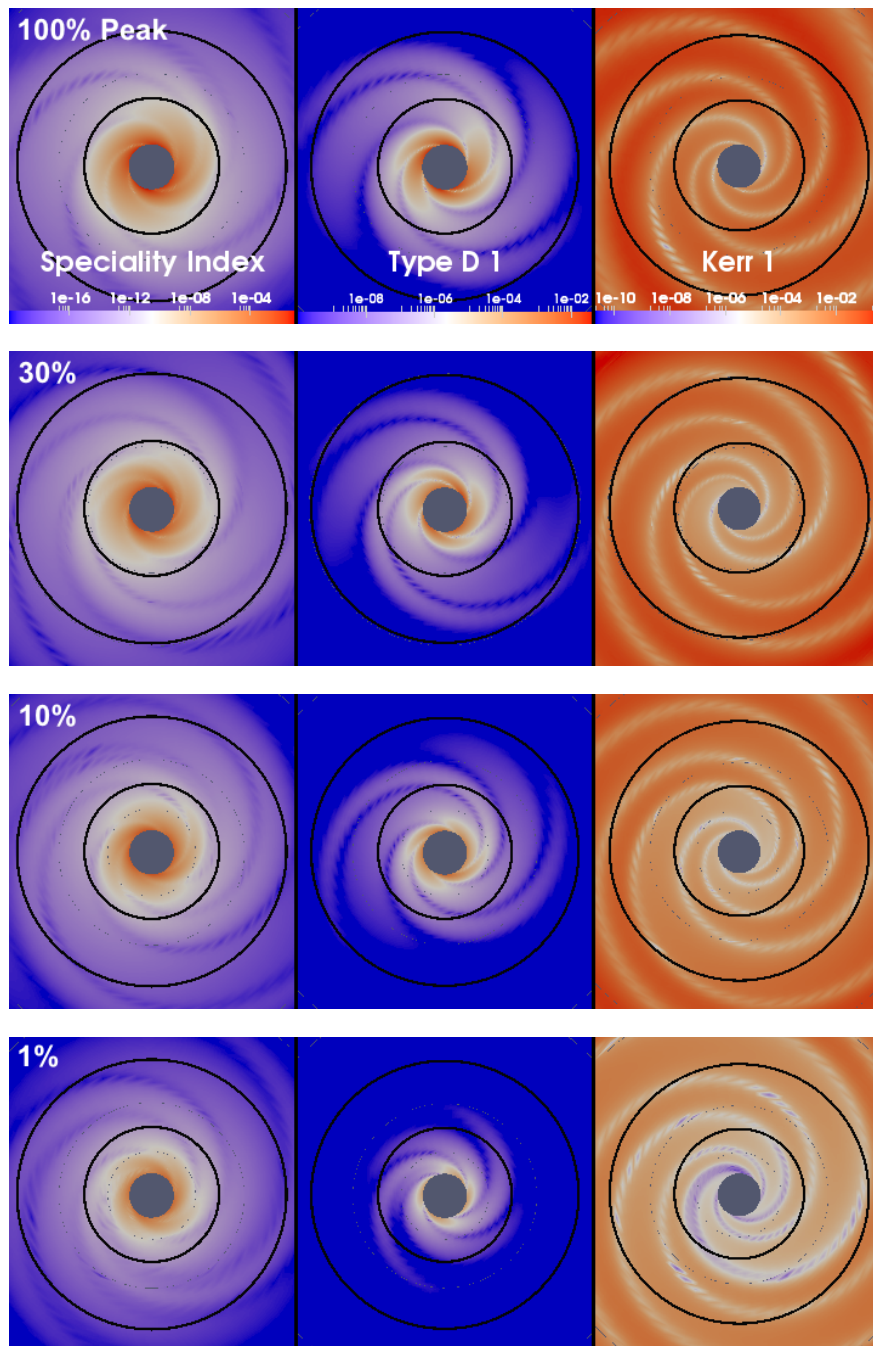


Figure 14: Absolute Kerrness measures on slices of the BBH post-merger spacetime. The data is presented in the equatorial plane, with the gray region corresponding to the excised BH. The black circles correspond to coordinate radii $R = 5 M$ and $R = 10 M$. The columns correspond to Speciality Index, Type D 1, and Kerr 1, and the rows (from top to bottom) correspond to coordinate times at which the each measure at $R = 5 M$ achieves 100%, 30%, 10%, and 1% of the combined peak value. The quadrupolar pattern (with $|m| = 2$) in all three measures is consistent with the dominant quadrupolar radiation (recall that these are absolute measures, and hence do not distinguish between positive and negative values). Notice that the algebraic measures—Speciality Index and Type D 1—settle outward-in, whereas Kerr 1, a geometric measure, settles inward-out. Additionally, the structures in the measures are

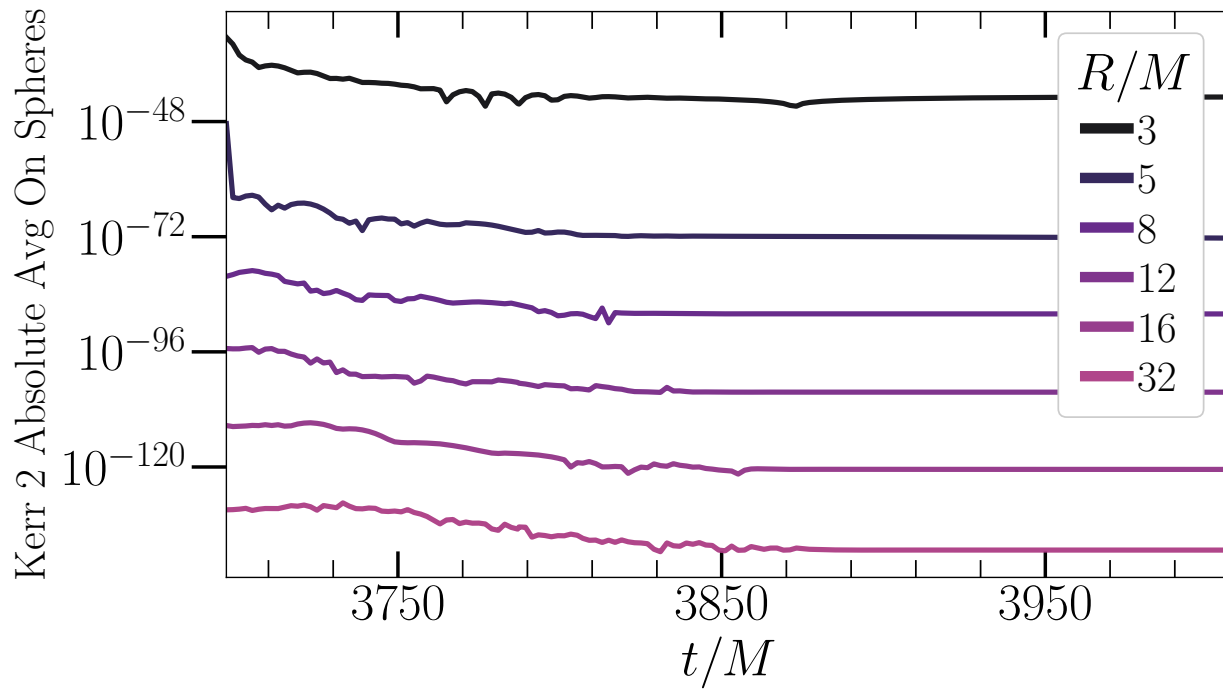


Figure 15: Kerr 2 measure throughout the post-merger BBH simulation, averaged on a variety of coordinate 2-spheres of radius R . The values remain relatively constant and low, indicating that no NUT charge is gained during ringdown.

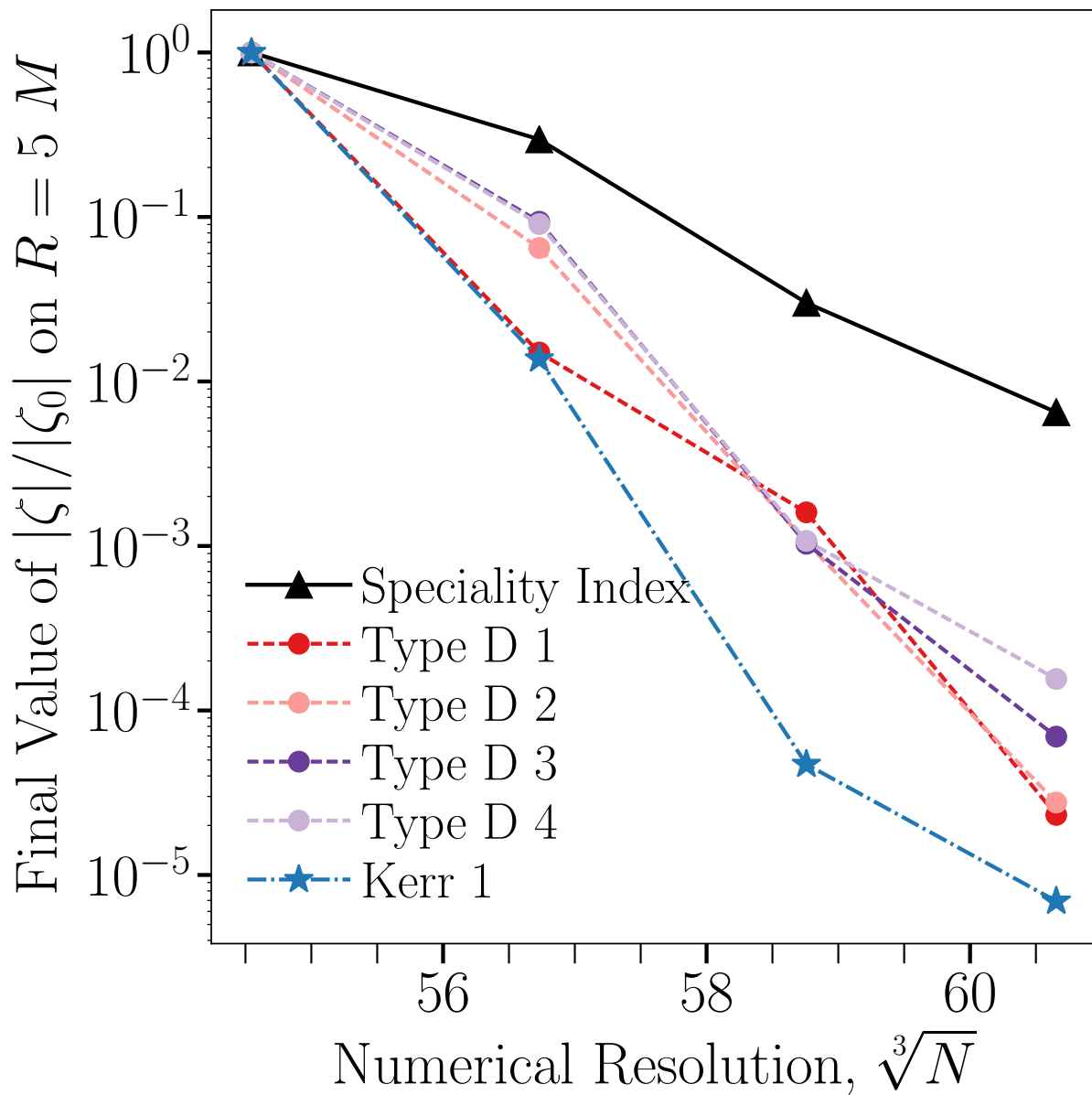


Figure 16: Exponential convergence of the noise floor of each Kerrness measure on the final timestep of the BBH simulation. Each measure ζ is presented as an average over a 2-sphere of $R = 5 M$ (where the measures have settled to a noise floor), normalized by $|\zeta_0|$, the average of the lowest resolution. The resolution is indicated by $\sqrt[3]{N}$, where N is the number of spectral collocation points. The convergence to zero shows that the noise floor observed in Fig. 13 is a numerical noise floor, rather than real a physical artifact. We have also testing this convergence behavior on a 2-sphere $R = 5 M$ and verified that the behavior is consistent (although more noisy).

The Kerrness measures quantify the violation of the conditions for a manifold to be isometric to Kerr and therefore, they need not have the same dimensions and sensitivities. Thus, one cannot compare the absolute magnitudes of these measures with each other and directly translate their value into statements on validity of start time of perturbative regime. In order to normalize and combine them into an overall measure of Kerrness, we use the concomitant percentage decrease from their peak values.

We present the percentage decrease of each of these measures from their peak values mapped on to the news function in Fig. 17 and Fig. 18. In the bottom panels of these figures, the news function is plotted as a function of time. On the same time axis, the top panel depicts the corresponding evolution of the Kerrness measure in the strong-field region. The waveform feature in the bottom panel at a particular time coordinate is associated to the timeslice carrying the same time label, via source-effect association outlined in Sec. 4.2.2. In the bottom panel, the Kerrness value at this time characterizes the deviation from Kerr.

In these figures, we delineate 6 lines marking the percentage decrease from the peak value of each of the Kerrness measures as a function of time—both in the strong-field region and on the news function at \mathcal{S}^+ . As stated before, these measures have different decay properties and so do not decay to a particular percentage of their peak value at the same time. The difference between the time at which measures decay to a particular percent is tabulated in Table 5.

% of peak value	Spread in time	Combined % Time
100 %	12 M	1.5 M
50 %	9.8 M	11 M
30 %	9 M	14.7 M
10 %	8.3 M	21.7 M
5 %	8.7 M	25.9 M
1 %	6.1 M	35.3 M

Table 5: The spread in the time for given % of the peak value of Kerrness measures computed using all the measures. The combined % time refers to the value of the dashed lines in Fig. 19 and corresponds to the time at which all the measures have at least decayed to the indicated % relative to the time at which the peak amplitude of news function occurs.

We present the combined percentage decrease from the peak value on the news function in Fig. 19. The shaded bands correspond to spread in percentage decay on the news function. The widths of these bands are given in Table 5. The solid line at the end of each band marks

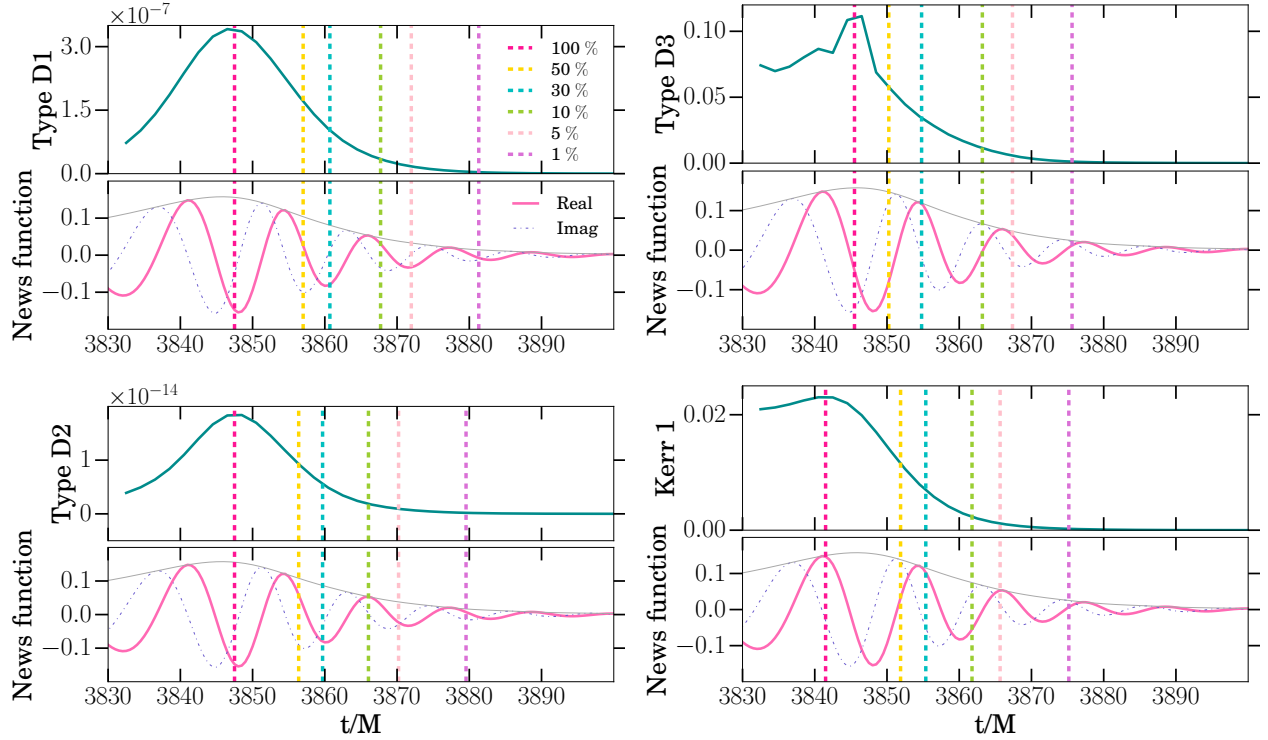


Figure 17: Connecting the Kerrness measures in the strong-field to dynamics at \mathcal{S}^+ using the procedure described in Sec. 4.3.3 on the BBH post-merger. The **left panels** map the algebraic measures and the **right panels** map the geometric measures on to the news function. The **top panel** within each subplot corresponds to a Kerrness measure in the strong-field, while the **bottom panel** shows the news function at \mathcal{S}^+ . The purpose of plotting the news function directly below each Kerrness measure is to emphasize that the top and bottom panels are mapped to the same time axis. The dashed lines of different colors indicate the % decrease from the peak value of the respective Kerrness measures. The horizontal axis corresponds to the simulation coordinate time induced on the news function extracted from a world tube radius of $R = 128 M$. Furthermore, unlike the strong-field result plots that aim at rigorous characterization of isometry to Kerr, here we aim at providing insight into validating the start time of ringdown for data analysis. Therefore, these plots are on linear scale as opposed to logarithmic scale. Notice that the curves on the left panel decay more slowly than those on the right; Type D 1 is the slowest to decay, closely followed by Type D 2. Also, recall that we cannot compare the magnitude of the top part of each of these panels as they are dimensionally different.

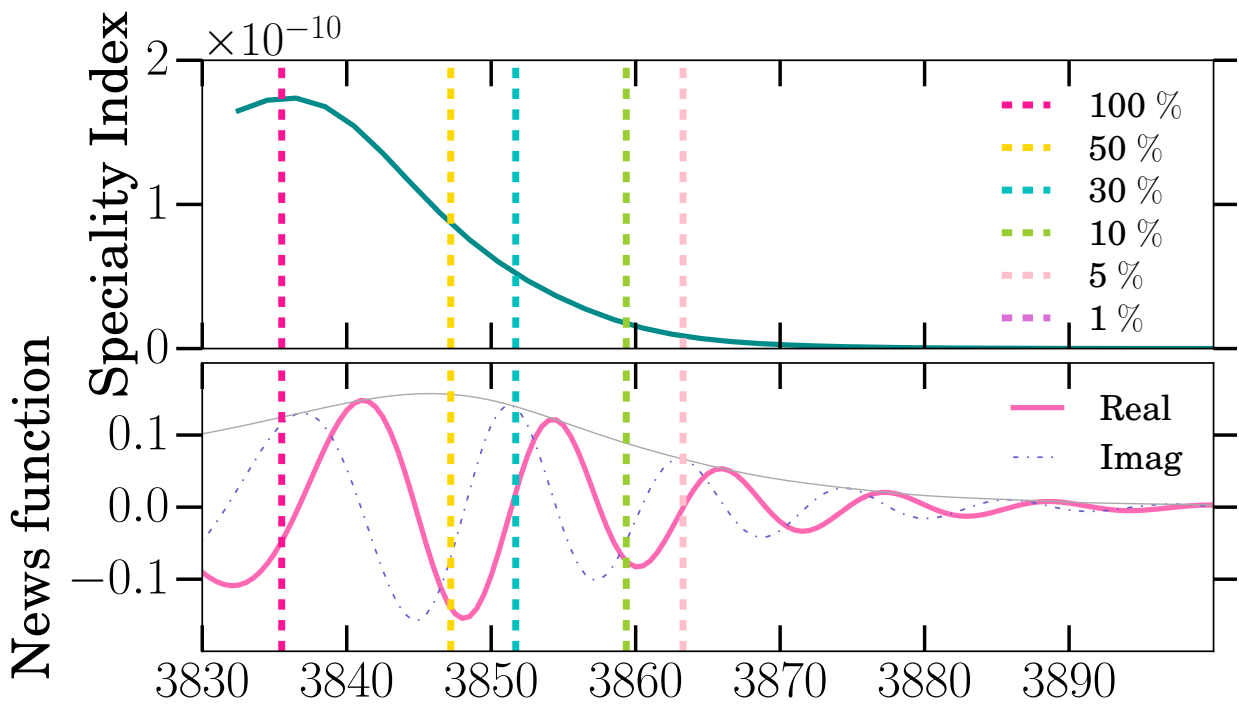


Figure 18: This figure is similar to Fig. 17 but for Speciality Index. We plot this separately as it is an independent measure and decays rapidly compared to the other measures. Further, we do not indicate the 1% of peak line because of numerical noise (cf. Fig. 13) which leads to unreliable root finding for time of percentage decrease.

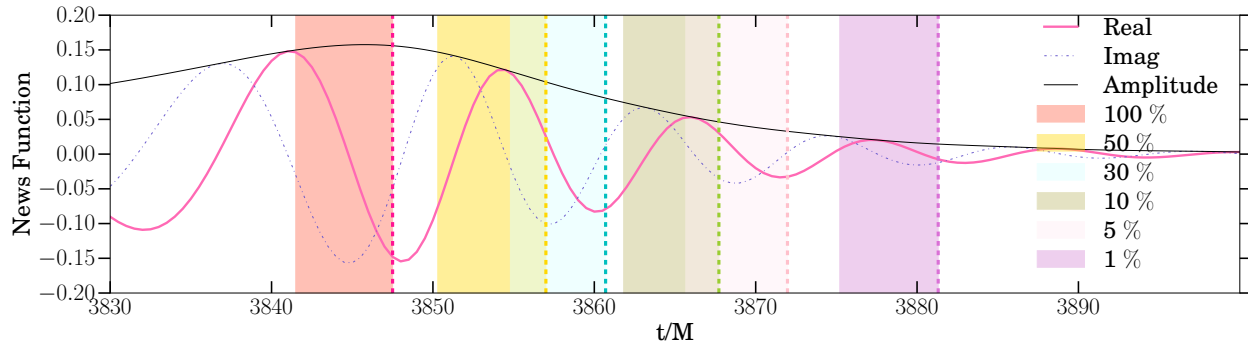


Figure 19: The concomitant decrease of all of our Kerrness measures. The dashed lines indicate the time at which all the measures decay to at least the indicated % of peak. The bands color the region in which different measures decrease to the indicated % of peak. Notice that there is about half a cycle spread in each of these bands. Therefore, the dashed lines provide a conservative idea of the validity of the choice of the start time for data analysis. We have specifically included the spread of these bands as a quantifier of error bounds in the statements of validity made further in this chapter. Furthermore, one could shrink the right boundary of these shaded bands if one combines the Kerrness measures with appropriate weights based on their sensitivity to the spacetime curvature and the final remnant’s effective potential.

the time when all these measures have decayed to the indicated percentages and this can be used to conservatively choose the start time.

Furthermore, in this figure we do not include the Speciality Index. The Speciality Index is an independent measure that quantifies if the manifold is algebraically special. Since this is the weakest condition in our Kerrness characterization scheme, we see that it gets satisfied earliest on the post-merger simulation from Fig. 18. The 1% of peak line which occurs unexpectedly late arises because of numerical reasons. We assert this by looking at the nearly flat nature of Speciality Index curves in Fig. 13 at late times, very close to the numerical noise floor.

We observe that all measures decay to $\sim 50\%$ of their peak value within half a cycle from the peak of the news function. Further, in approximately one cycle, all the measures are reduced to $\sim 30\%$ of their peak values. The spread in each of the bands is about $\sim 10 M$ when we include all the Kerrness measures in computing the band, and this shrinks to $\sim 6 M$ when we exclude Speciality Index.

We combine the measures with equal weights, thereby presenting a conservative result. Furthermore, we have repeated our analysis with larger worldtube radii and confirmed that

our results for the spread do not change significantly. For instance, using $R = 128 M$ results in a time shift of about $+4 M$ relative to the $R = 5 M$ results, and this positive time shift monotonically decreases with radius for $R = 32, 64$ and $80 M$.

4.4.3 Estimating and mapping the perturbation amplitude onto the waveform

In order to provide a physical understanding for the values of the measures in the strong-field region shown in Figs. 13 and 14, we can compare the values to those on an initial slice of a perturbed Kerr BH with the same final mass and spin as the BBH simulation, as outlined in Sec. 4.2.3. We can then map the inferred strong-field perturbation amplitude ε onto the waveform using the procedure outlined in Secs. 4.2.2 and 4.3.3. This procedure involves the following steps:

1. Generate perturbed Kerr manifolds for a range of amplitudes ε .
2. Compute the Kerrness measures at $R = 5 M$ on these slices.
3. Compute the Kerrness measures at $R = 5 M$ on the post-merger BBH simulation (verifying that the gauge-invariant areal radii of the $R = 5 M$ coordinate 2-spheres are approximately (within $0.01 M$ in our case) equal for the single-BH and the BBH case). If the areal radii do not match, then choose a different surface on the perturbation slice such that the two areal radii agree.
4. Identify the coordinate time in the post-merger BBH simulation at which the Kerrness measures at $R = 5 M$ agree with those on the perturbed Kerr slice for a given ε — this gives a *crossing time* for this ε .
5. Use this crossing time to map the inferred ε onto the waveform.

Fig. 22 shows the inferred ε for the BBH ringdown simulation as a function of coordinate time in the simulation. The gauge-invariant areal radii at $R = 5 M$ on the BBH simulation slices and on the metric perturbation are within $10^{-2} M$. The values of the Kerrness measures on the perturbed data vary quadratically with ε , as shown in Fig. 8. At higher values of ε , they obtain higher-power dependence, as discussed in Sec. 4.2.3. Each Kerrness measure decays through various ε as the simulation progresses. Type D 1 and Type D 2, the two algebraic conditions, have comparable crossing times for a given ε , while the two geometric KV conditions, Type D 3 and Kerr 1, also have comparable crossing times. Speciality Index crosses around $10 M$ before the other measures, in part because it is a weaker condition that

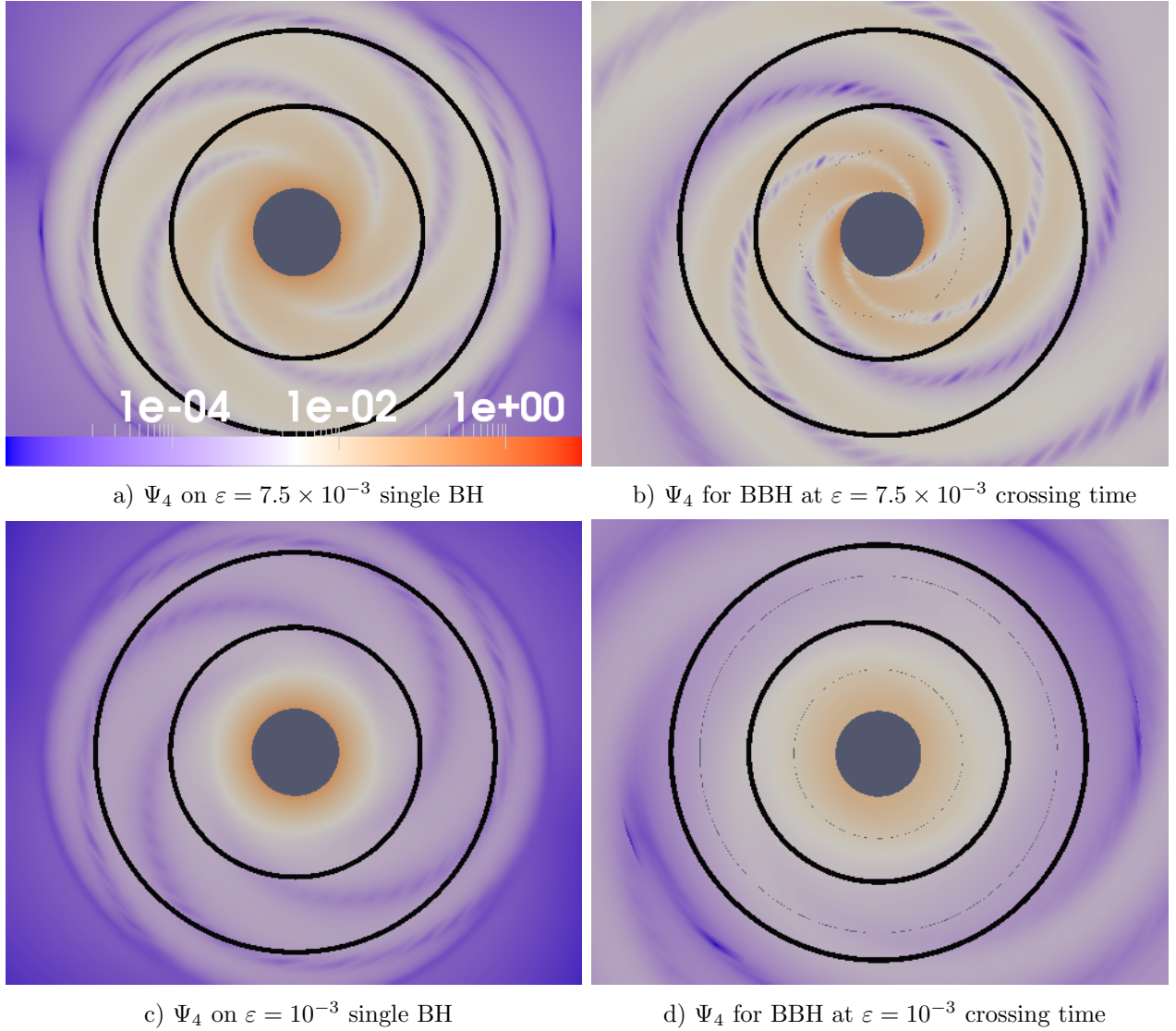


Figure 20: Ψ_4 in the equatorial plane for both a single BH with an $l = m = 2$ perturbation of amplitude $\varepsilon = 7.5 \times 10^{-3}$ and $\varepsilon = 10^{-3}$ (**left panel**), and for the BBH ringdown (**right panel**) at times that achieve the same Kerrness as (**left panel**). For all cases, Kerrness is matched on a coordinate 2-sphere of $R = 5M$. The two black circles correspond to coordinate radii $R = 5M$ and $R = 8M$. The Gaussian envelope of width $R = 8M$, as described in Fig. 7, can be seen in the plots for the single BH cases. Note that this is only meant to show qualitative agreement between Ψ_4 on both slices, as the quantity is still subject to coordinate tetrad effects in the strong-field region. Notice that although the two systems look similar, allowing us to infer the BBH simulation perturbation amplitude, the mapping does have some imperfections.

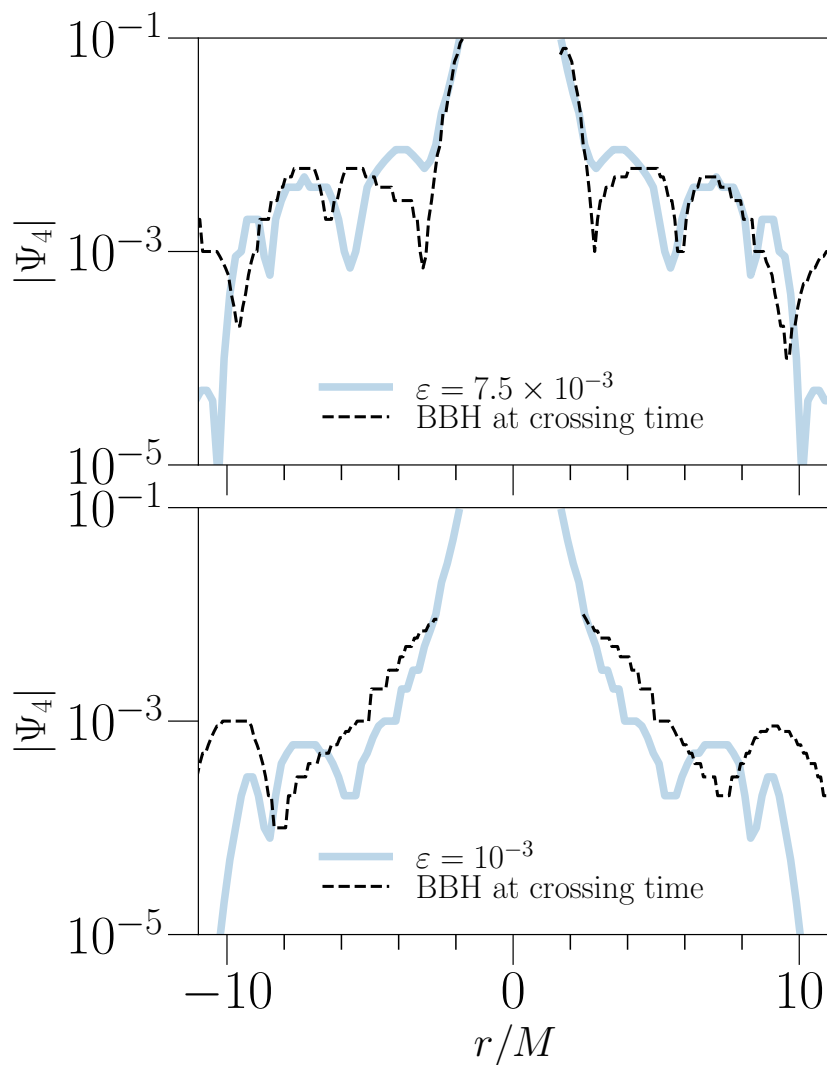


Figure 21: Ψ_4 in on the x-axis (in the equatorial plane) for both a single BH with an $l = m = 2$ perturbation of amplitude $\varepsilon = 7.5 \times 10^{-3}$ (**top panel**) and $\varepsilon = 10^{-3}$ (**bottom panel**), and for the BBH ringdown at times that achieve the same Kerrness. For all cases, Kerrness is matched on a coordinate 2-sphere of $R = 5M$. The x-axis of the plot shows the radius, and includes the data within the Gaussian envelope of width $R = 8M$, as described in Fig. 7. Note that this is only meant to show qualitative agreement between Ψ_4 on both slices, as the quantity is still subject to coordinate tetrad effects in the strong-field region. Notice that although the two systems look similar, the mapping does have some imperfections. Recall, however, that it is ultimately the invariant Kerrness measures that determine the mapping between the perturbation amplitude and the BBH merger-ringdown time.

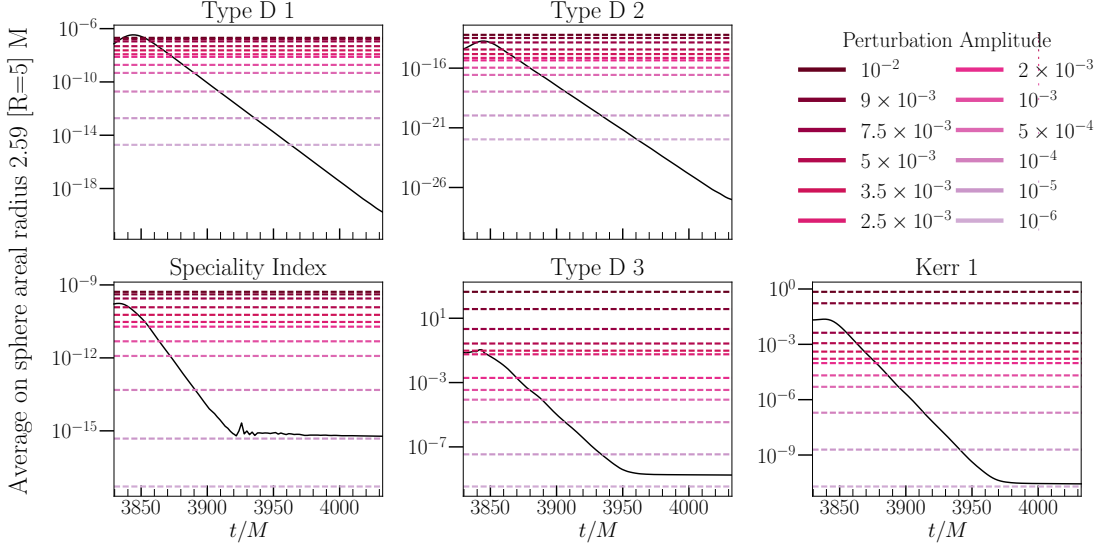


Figure 22: Comparison of the Kerrness measures during the BBH post-merger to the values of the Kerrness measures on an $l = m = 2$ QNM perturbed Kerr BH of various perturbation amplitudes ε , with the same mass and spin parameters. The measures are averaged on a 2-sphere of coordinate radius $R = 5 M$, which corresponds to comparable areal radii of $\sim 2.59 M$ in both systems. The measures evaluated on the BBH slices are shown by solid black lines, decaying as a function of time. The Kerrness measures for the perturbed metric are presented as horizontal dashed red lines, one for each ε . The times at which the BBH curves intersect the Kerrness values for a given ε Kerr perturbation give a scale for the BBH Kerrness measures as the post-merger progresses. These times, known as *crossing times* are then mapped onto the waveform, and used to validate the start time of ringdown. Note that the measures have different crossing times. The time axes are shifted to agree with the timestamps of the GW at $R = 128 M$, as explained in Table 4.

the others. Each crossing time has an intrinsic $2M$ spread due to sampling, and not all measures cross each ε due to numerical noise floors, leading to spreads in crossing time.

In Fig. 21, we qualitatively check the spacetime features by comparing Ψ_4 corresponding to $\varepsilon = 7.5 \times 10^{-3}$ and 10^{-3} on the perturbed Kerr metric with the corresponding timeslice during the post-merger simulation. The crossing time spread for a particular ε arises because of the imperfect mapping between an analytically perturbed Kerr BH and the post-merger spacetime. Therefore, unlike in an ideal mapping, the combined crossing times will have a spread. In particular, the difference in the features between the post-merger and the perturbed Kerr slice indicates a difference in symmetry and explains the larger spread in the crossing time between the KV-dependent measures. We see that the spread in the combined crossing times using only algebraic measures is much smaller than when we include the geometric measures.

We next map the inferred perturbation amplitude to the news function, using a procedure similar to the one in the previous section, and present the result in Fig. 23. The top panel of the figure indicates the crossing time for the Speciality Index, the middle panel for the algebraic measures, and the bottom panel shows that for geometric measures. The spread in the crossing time for the algebraic measures decreases from $\sim 6M$ at the start, to our sampling rate, $2M$. This occurs because at the very start of post-merger, the system is not yet in a perturbative regime and therefore, our mapping contains a larger error. Geometric measures are more drastically affected by the imperfections in the mapping, indicating the differences in the symmetries of the two systems. On including the geometric measures, the crossing time spreads to $\sim 8M$. We confirm that the spread of the crossing times calculated using the algebraic measures is always contained within the spread of crossing times calculated using the geometric measures.

As the signal decays from the peak to a barely visible amplitude on a linear scale ($\sim 3 - 4$ cycles) at \mathcal{S}^+ , the corresponding perturbation in the strong-field region decreases by an order of magnitude. The peak of the news function corresponds to a perturbation amplitude of $\sim 7.5 \times 10^{-3}$. Further, it takes about 2 cycles in the wave zone for the perturbation amplitude to decay to half its peak value. Also, by the time the perturbation amplitude decays by an order of magnitude, there is hardly any power left in the signal.

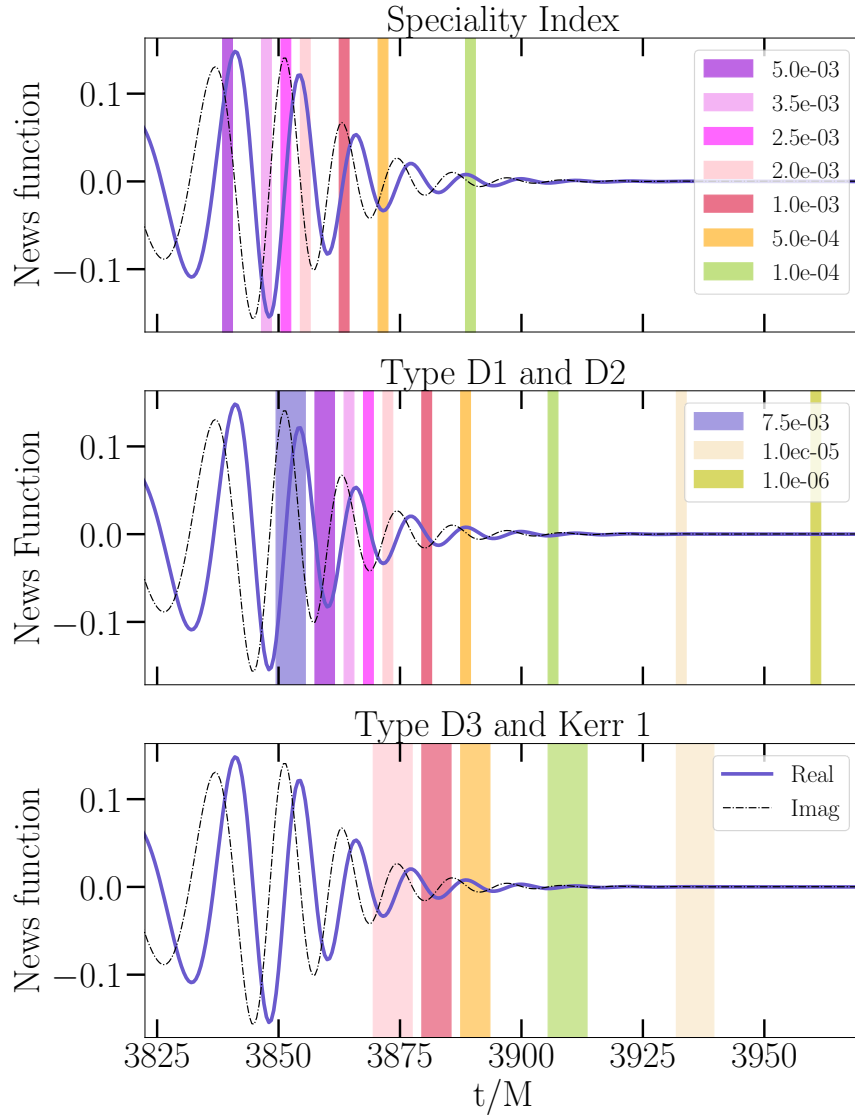


Figure 23: Mapping the inferred perturbation amplitude close to the BH onto the news function. The **top panel** shows the spread in the crossing times computed using just the Speciality Index, the **middle panel** uses only the algebraic measures and the **bottom panel** utilizes only the geometric measures. Notice that amplitudes larger than 2×10^{-3} do cross the post-merger timeslices when computed using the geometric measures and that the crossing time spreads in them are relatively large, suggesting a difference in the symmetry of a perturbed Kerr metric and the post-merger BBH spacetime. However, this does not seem to be reflected when we just consider the algebraic measures as they have a relatively small spread in the crossing time. The spread in the crossing time of the Speciality Index is equal to the sampling rate.

4.4.4 Implication of the start time on data analysis

From news to h

In order to compare the Kerrness measures on the GW to the loss in signal-to-noise ratio (SNR) at the times used in [5], we must first calculate the strain h from the news function, and then calculate the merger time. As outlined in Sec. 4.3.3, h can be calculated by integrating the CCE news function. One can also independently calculate h using the Regge-Wheeler-Zerilli (RWZ) (cf. [146] for details on the method) [147, 148, 90, 149] method and then extrapolating it in powers of the extraction radius (cf. [150] for details). The RWZ method and extrapolation have been implemented and tested in SpEC [150, 151], and the strain calculated by this method was presented in the GW150914 detection chapter [134]. This method, however, has a different retarded time axis [150] than the CCE news function. Thus, we differentiate the RWZ strain to get a news function, and shift it to align in phase with the CCE news function. We check the CCE results by comparing the output of the two methods, presenting the results in Fig. 24.

In the GW150914 testing GR study [5], t_{merger} is defined as the point at which the quadrature sum of the h_{\times} and h_{+} polarizations of the most-probable, or *maximum a posteriori* (MAP) waveform, produced by Effective-One-Body (SEOBNRv4) template [152] is maximal. For this study, we use the $l = m = 2$ spin-weighted spherical harmonic mode of the MAP waveform, as this is the least-damped QNM. In this study, rather than using the EOBNR waveform, we calculate t_{merger} based on the time of maximum amplitude of the time-shifted RWZ strain, as

$$t_{\text{merger}} \equiv \{t | h^2(t) = \max_{t'}(h^2(t'))\}, \quad (4.27)$$

where

$$h^2 \equiv \text{Real}(h)^2 + \text{Imag}(h)^2. \quad (4.28)$$

We find $t_{\text{merger}} = 3839.0 \pm 0.1 M$.

Start time and the SNR

While picking too early a start time for an analysis that relies on being in ringdown gives inaccurate and biased results, picking a start time too late leads to a large statistical error. Since the amplitude of the signal decays exponentially with time, the SNR in ringdown decreases as exponential-squared with the start time. Consequently, the spread in the

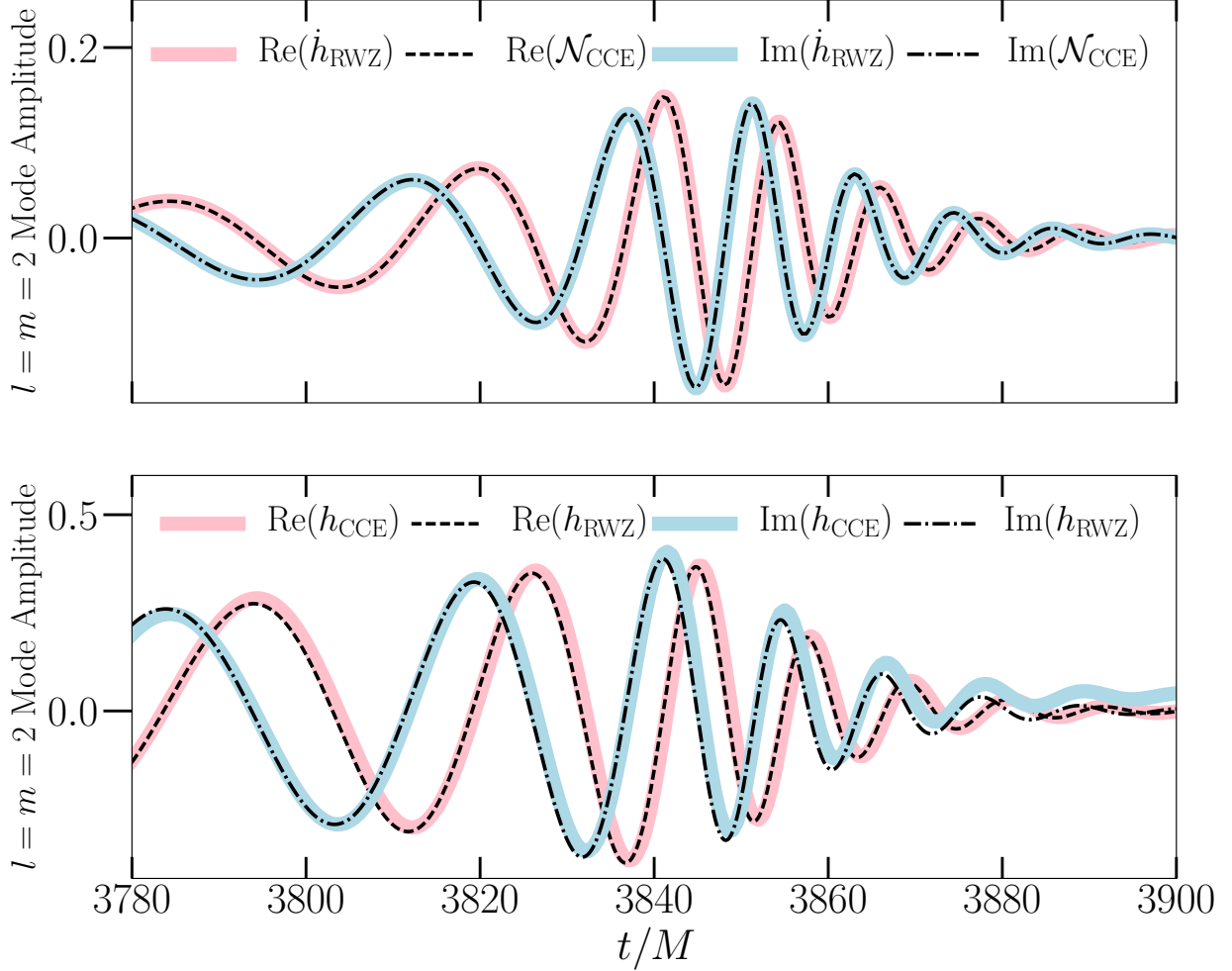


Figure 24: Comparison between the strain h calculated using CCE and RWZ methods. All waveforms are presented in terms of the $l = m = 2$ mode. We use the fact that the strain is the integral of the news function to cross-check the methods. The **top panel** shows the CCE news function \mathcal{N}_{CCE} compared to \dot{h}_{RWZ} , the derivative of the RWZ strain. The **bottom panel** shows h_{CCE} , the integral of the CCE news function, compared to the RWZ strain h_{RWZ} . We find good agreement until late times, when h_{CCE} begins to drift, likely due to the numerical integration scheme used.

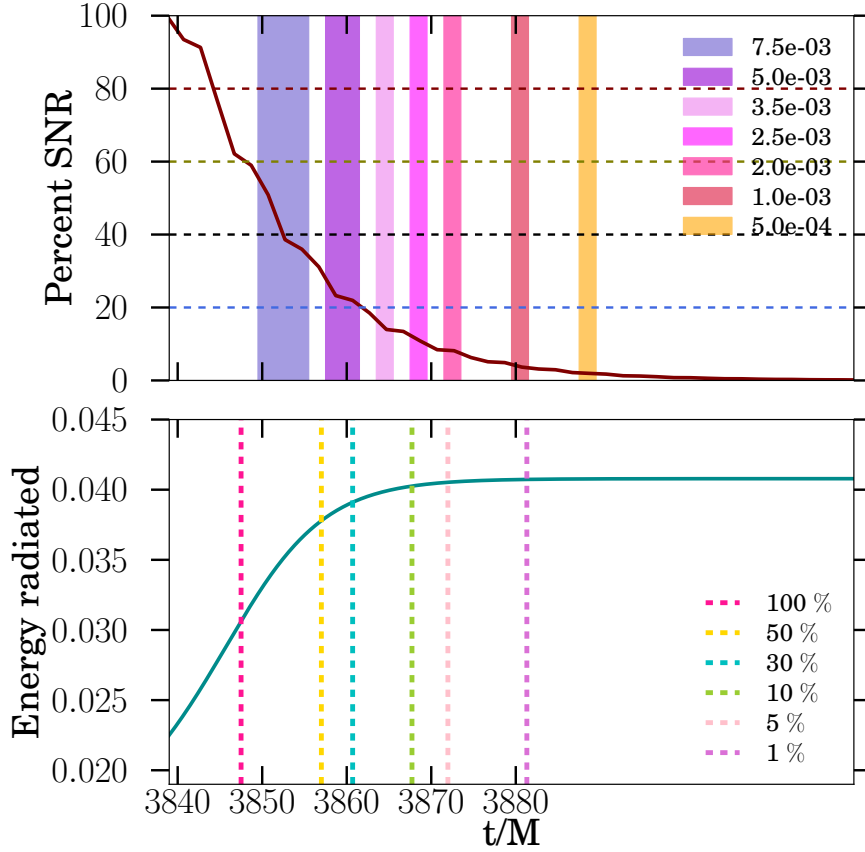


Figure 25: The **top panel** of this figure shows the percentage decrease of SNR from the peak value. The % SNR is set to 100 at t_{merger} . For this plot, we evaluate Eq. (4.29) with varying lower bounds for the integration. The dashed horizontal lines correspond to $\{80, 60, 40, 20\}\%$ SNR. On the same plot, we mark the perturbation amplitude bands for a direct comparison between perturbation amplitude and statistical error. Notice that by the time the perturbation amplitude near the BH decreases by an order of magnitude, there is only a few percent of SNR left in the signal, emphasizing the sharp trade-off between the systematic biases arising from modeling the post-merger as perturbed Kerr and the statistical uncertainty arising due to exponential decay of signal amplitude. The **bottom panel** shows the total energy radiated in units of M during the merger-ringdown. This is calculated by integrating Eq. (4.31). Again, we have plotted the concomitant percentage decrease of the Kerrness measures from their peak values for an easy comparison between the statistical and systematic errors associated with the choice of the start time of ringdown. In particular, the constant settling in the total radiated energy occurs between the time when the Kerrness measures have decayed to 5 – 1% of their peak values, implying that at these times the GW is very weak in amplitude.

No. of cycles	% SNR	% Kernness	$\varepsilon/10^{-3}$
peak	60	100	7.5
$\frac{1}{2}$ cycle	30 - 40	40 - 50	7.5
1 cycle	20 - 25	35 - 30	5
$1 \frac{1}{2}$ cycles	10 - 20	8 - 12	3.5
2 cycles	~ 10	7 - 5	2 - 2.5
$2 \frac{1}{2}$ cycles	< 10	~ 1	1 - 2
3 cycles	< 5	< 1	0.5 - 1

Table 6: Summary of our results. The first column counts the number of cycles from the peak of the news function. The second column presents the drop in SNR with start time chosen in the data analysis. SNR is normalized to have 100% when the data analysis starts at the peak of the waveform ($h(t)$) i.e., at $3839 M$. The third column shows the concomitant percentage decrease in the Kernness measures from the peak value (similar to Fig. 19). Further, in the last column we present the perturbation amplitude inferred by the crossing times computed with Type D 1 and D 2 measures (similar to middle panel of Fig. 23.)

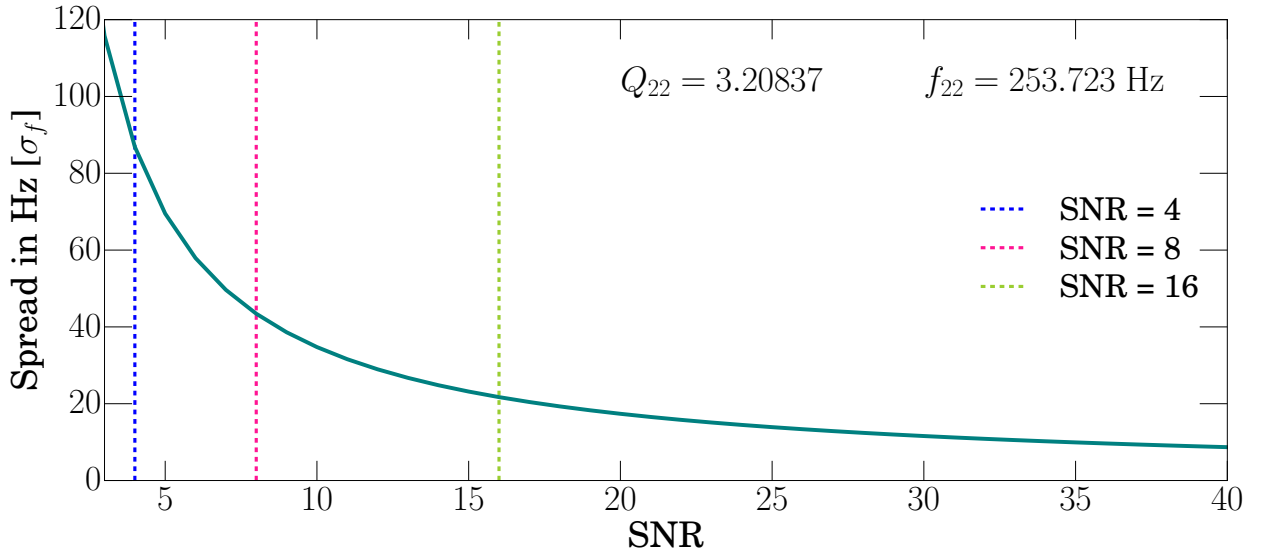


Figure 26: Spread in estimation of dominant mode frequency as a function of SNR. We present the spread, σ_f in the estimation of frequency calculated using Fisher information matrix formalism. We should the increase in spread with decreasing SNR, providing the rough intuition on the implication of Fig. 25 on parameter estimation.

posteriors during estimation of ringdown parameters, which goes inversely proportional to match-filtered SNR, increases and gives rise to large statistical uncertainties. Therefore, one must choose an optimal middle ground considering both these factors.

In the top panel of Fig. 25, we show the percentage decrease in match-filtered SNR with the start time of the ringdown. A match-filtered SNR is a noise-weighted scalar product between the signal and the template and is defined as

$$\text{SNR} = 4 \int_0^\infty \frac{\tilde{h}_1^*(f') \tilde{h}_2(f')}{S_h(f')} df' = \langle h_1 | h_2 \rangle, \quad (4.29)$$

where * denotes complex conjugation for ease of readability. Here, $h_1(t)$ corresponds to a ringdown waveform that is tapered at t_{merger} and acts as a signal. We filter this against the template, $h_2(t)$, which is tapered with varying start time. Further, $S_h(f)$ corresponds to power spectral density (PSD) of aLIGO at design sensitivity [153]. However, since we present our results in terms of ratios, our analysis remains valid to any detector noise curve. Then, a Fourier transform is taken to evaluate Eq. (4.29). Here we use only the $l = m = 2$ spin-weighted spherical harmonic mode of the RWZ strain waveform computed in Sec. 4.4.4. The system is considered to be optimally oriented with respect to the detector for this calculation.

The tapering is done with a tanh window function defined as

$$\mathfrak{W}(t) = \tanh[\alpha_0(t - t_0)]/2. \quad (4.30)$$

t_0 is the time around which the tapering is centered and it is set to the start time of the perturbative regime. α_0 is set to 10 in making the top panel of Fig. 25. Furthermore, we confirm that our results do not change significantly with the tuning parameter α_0 using $\alpha_0 = \{2, 5, 10, 20\} M^{-1}$.

We then present percentage decrease of SNR in the top panel of Fig. 25 by defining 100% for start time at t_{merger} . Further, on this same plot we also indicate the amplitude of perturbation in the strong-field region (as calculated using the algebraic measures) at the start time, giving an insight into how statistical and systematic errors vary with the choice of start time.

The bottom panel of Fig. 25 presents the total energy radiated through the merger-ringdown as a function of time. This indicates the strength of GW signal and is calculated by integrating [154]

$$\frac{dE}{dt} = \lim_{r \rightarrow \infty} \frac{r^2}{16\pi} \oint \left| \int_{-\infty}^t \Psi_4 dt' \right|^2 d\Omega. \quad (4.31)$$

Furthermore, on the same plot we mark the percentage decrease of the Kerrness measures from their peak values, providing a comparison between the strength of the signal left for performing the analysis versus Kerrness evaluated in the strong-field region.

To impress the sharp trade-off in systematic and statistical uncertainties in choosing the start time of the ringdown and, to provide an intuition of implication of Fig. 25, we present the spread in estimation of dominant QNM frequency, f_{22} in Fig. 26. For this, we calculate the spread using the Fisher information matrix formalism similar to that in Eq. 4.1a of [155], for a GW150914-like system. In particular, we set f_{22} to 253.7 Hz and the quality factor, Q_{22} to 3.2. However, we emphasize that this is a rough estimate intended only to provide intuition and, we plan to follow this up by a rigorous Bayesian parameter estimation in the future.

We present the interplay between the systematic and statistical uncertainty concisely in Table 6. Furthermore, we find that by the time the news function peaks, the SNR has already dropped down to 60%. However, at this time the algebraic Kerrness measures are at their peak value. We also observe that by about a cycle of news function, there is less than 20 percent SNR left in the signal. Therefore, there seems to be a sharp trade-off between the systematic modeling error and statistical uncertainties.

4.4.5 Comparison with GW150914 testing GR chapter

The test of consistency of ringdown of the GW150914 signal with the analytically predicted QNM frequency is given in Fig. 5 of [5]. The analysis chooses various start times of ringdown, namely $t_{\text{merger}} + 0, 1, 3, 5, 6.5$ ms. At a start time of $t_{\text{merger}} + 3$ ms (or later), parameter estimation of the dominant QNM in ringdown is consistent with predictions using initial masses and spins.

A time 3 ms for the system corresponds to $9.4 M$ from t_{merger} . In our analysis, $t_{\text{merger}} = 3839 M$ (cf. Eq. (4.27)), while the peak of the news function occurs at $3846 M$. Thus, 3 ms corresponds to $2.4 M$ after the peak of the news function. In this region, as shown in Fig. 27, the perturbation amplitude is $\gtrsim 7.5 \times 10^{-3}$. Our analysis indicates that this corresponds to a relatively large deviation from Kerr. Recall that Fig. 8 suggests that $\varepsilon = 5 \times 10^{-3}$ is the approximate start of the nonlinear regime.

With a start time of $t_{\text{merger}} + 3$ ms, the SNR was about 8.5 and the spread in the estimate of QNM frequency was roughly 40 Hz [5]. Because of this low SNR and high spread, the GW150914 testing GR analysis may not have been sensitive to the large non-Kerrness we see close to the BH. However, in the case of higher SNR, where the analysis is sensitive to the

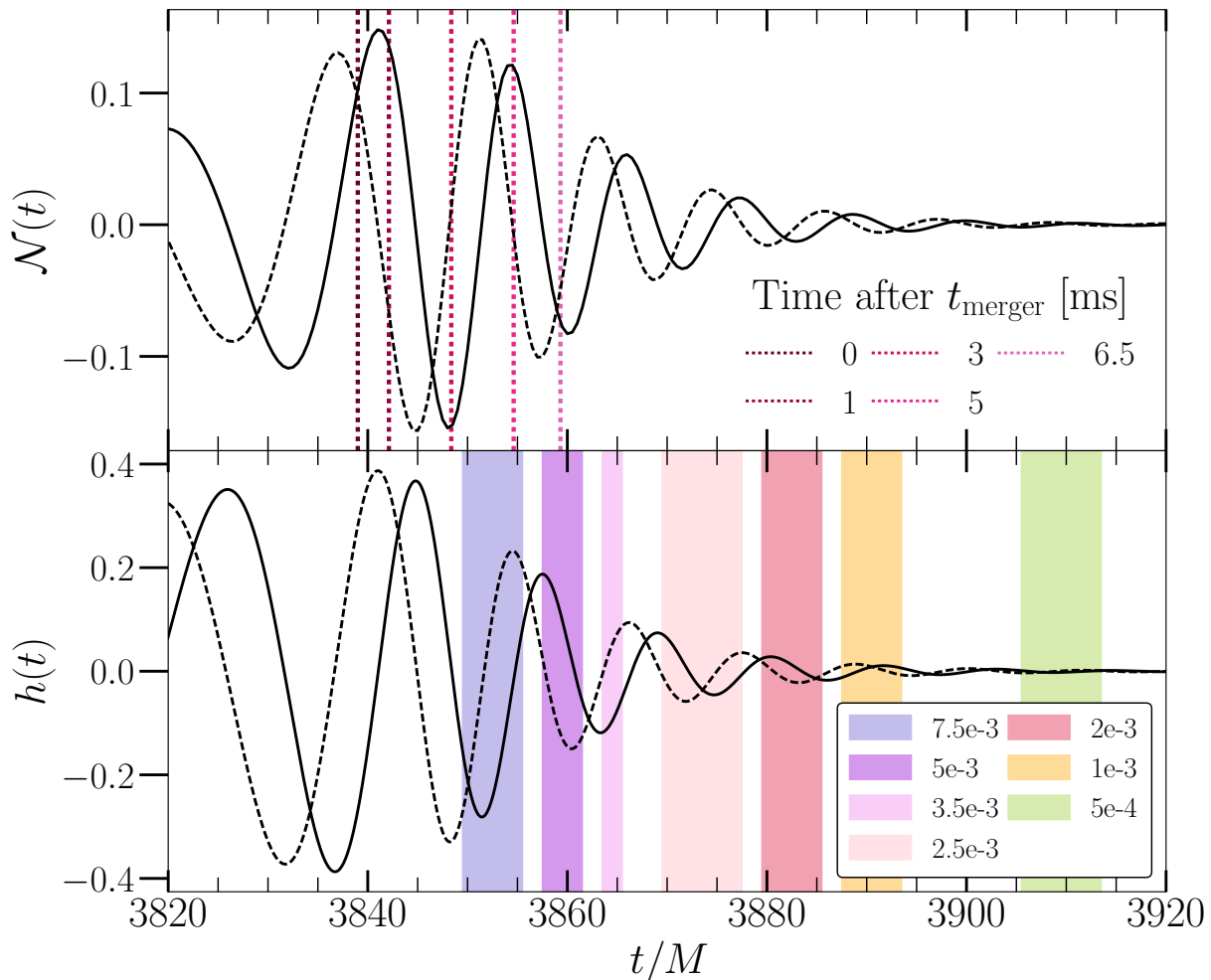


Figure 27: Comparison of the times chosen in the testing GR study of GW150914 [5]. Here, we make statements about their validity to perform tests that rely on the perturbative nature of the BH. Specifically, we propose that a plot of this nature be done for future detections, especially if the SNR is high, to gain an insight into the inferred strong-field perturbation amplitudes corresponding to different choices of ringdown start time. The dotted line in the **top panel** shows different choices of start time for performing tests on the detector data. The **bottom panel** shows what each time choice corresponds to in the simulation gauge. Although a practical choice of start time to perform tests like no-hair theorem tests should be decided based on the interplay between the statistical and systematic uncertainty, a plot of this nature gives significant understanding of the results of such tests. For instance, in the case of GW150914, had the signal been much louder than what we observed, this plot suggests that we *could* get biased results due to large inferred perturbation amplitude in the strong-field leading to errors in modeling the post-merger as a perturbed BH at 3 ms.

systematics of the ringdown model, our study suggests picking a later start time.

Our analysis uses geometric and algebraic conditions to identify isometry to Kerr. However, these conditions do not directly measure the deviation of the curvature BH potential from that of Kerr. Since the QNM are intrinsic tests of the BH potential along with the boundary conditions, deviation of QNM frequencies will depend on details of the BH potential, and thus are not directly quantified in our measures. Additionally, the parameters used in this study correspond to `SXS:BBH:0305` waveform used in the GW150914 detection chapter [97], which are slightly different from those of the MAP waveform used in the testing GR chapter.

4.5 Conclusion

In this study, we present a method for validating choices of the time at which a BBH GW signal can be considered to enter the ringdown stage. This is done by computing algebraic and geometric measures of Kerrness in the strong-field region of an NR simulation of a BBH ringdown, and then associating each point on the asymptotic-frame waveform with a particular value of these Kerrness measures. Thus, for each point on the asymptotic-frame waveform there is an estimate for how close the BH spacetime is to Kerr spacetime. This is the first time this set of measures, proposed in [106], are evaluated in the strong-field region. This is also the first time measures of Kerrness in the strong-field region is mapped onto the waveform. We outline this method in Secs. 4.2 and 4.3, and implement this analysis in Sec. 4.4 on a GW150914-like NR simulation.

We observe that after merger, the Kerrness measures of a BBH ringdown simulation decrease exponentially with coordinate time in the simulation, eventually settling to a numerical noise floor, as shown in Fig. 13. This decay is consistent with measuring Kerrness using multipole moments of the apparent horizon, as in Fig. 12 and [4]. In all cases, the measures on the final slice of the simulation indicate that the final remnant is a Kerr BH, thus providing numerical consistency with the BH uniqueness theorem. Moreover, we find that the final state in the multipolar analysis depends just on mass and spin, which serves as a confirmation of the no-hair theorem in the strong-field region. Additionally, as shown in Fig. 14, the Kerrness measures have a quadrupolar (with $|m| = 2$) structure consistent with the dominant gravitational radiation. The geometric measures, which rely on the existence of a Killing vector field, first decay to zero close to the horizon, then later they decay at larger radii as gravitational radiation propagates out. On the other hand, algebraic measures, which depend on principal null directions, first decay to zero at larger radii, before decaying near the BH. We also see that the NUT parameter remains zero during merger and ringdown, as

shown in Fig. 15.

These gauge-independent Kerrness measures are crucial to the nonlinear stability analysis of Kerr, as they quantify the deviation from being isometric to Kerr. The analytical behavior of these measures with perturbation amplitude is unknown [133, 122]. Through this study we provide insights into their numerical behavior in Fig. 8. We find that all of these measures scale quadratically with ε for low amplitude perturbations, but acquire higher-order nonlinearities for larger perturbation amplitudes. Furthermore, in Figs. 13 and 14, we provide the radial behavior of these measures, up to a large radius of $R = 128 M$. For a BBH simulation, we track these measures starting from merger, where linear perturbation theory is not expected to hold. Despite the large initial excitation, our study shows that the BBH ringdown simulation evolves to a final Kerr state, providing a numerical validation of the nonlinear stability of Kerr.

To connect the Kerrness measures in the strong-field region to the asymptotic waveform at \mathcal{I}^+ , we use CCE, which evolves Einstein's equations on a foliation of outgoing null hypersurfaces. A null characteristic evolution can be done only in a region free from caustics. We demonstrate that CCE results using a worldtube at $R = 5 M$ are consistent with those done from larger radii. This implies that during ringdown, caustics only exist very close to the BH. Furthermore, we show that the map between the strong-field region and the wave zone can be extended all the way in to $R = 5 M$.

Although caustics do not form, we see in Figs. 14, 21 strong features in the curvature quantity Ψ_4 in the region enclosed by $R \sim 10 M$. This implies that our extraction radius choice of $R = 5 M$ lies within the strong-field and within the support of the BH potential.

In Fig. 17, we label each point of the BBH ringdown waveform with the percentage decrease of the Kerrness measures in the strong-field region relative to their maximum values. In order to give a physical interpretation of the values of the Kerrness measures, we compare them throughout the post-merger spacetime to those evaluated on a $l = m = 2$ QNM perturbed Kerr BH of the same final mass and spin. From this we infer the amplitude of BH perturbation during ringdown and map onto a particular point in the BBH ringdown waveform; this is marked on the BBH ringdown waveform in Fig. 23.

As the BBH simulation proceeds after merger, the strong-field region starts looking like Kerr, indicating the validity of perturbative analysis. However, as time progresses, the amplitude of the ringdown decreases, leading to a rapid decay in SNR in a GW detection. We find that by the time the Kerrness measures decrease to 50% of their peak values, there is only about 20% SNR left in the signal. In terms of perturbation amplitude close to the BH,

this maps to an amplitude between $7.5 - 5 \times 10^{-3}$. This occurs after $1 - 1.5$ cycles of the news function, which corresponds to $\sim 16.4 M$ after t_{merger} . Additionally, we find that the start time of ringdown used in [5], $t_{\text{merger}} + 3 \text{ ms}$, corresponds to an amplitude of 7.5×10^{-3} . Our results also agree with the start time proposed in [156]. In future detections with higher SNR, where the statistical noise is significantly smaller, one may need to choose a later start time to perform precision tests of GR such as no-hair theorem tests.

A future extension to this project would be to investigate methods that allow us to perform similar source-asymptotic frame associations for smaller radii. For instance, the light ring would be an interesting region to monitor as it is crucial to the QNM structure. This can perhaps be done numerically through ray-tracing methods such as those used in [157] and [158], to understand the evolution of the peak of the BH potential (if it forms). Another possible technique could be to try performing CCE from smaller radii after the high amplitude of the initial excitation has reduced. Additionally, being able to perform this association at smaller radii would allow one to understand the propagation of perturbations very close to the BH horizon onto the waveform; these are expected to be redshifted and appear on the waveform with a large time delay.

Another avenue of future work would be investigating the effects of implementing a more realistic condition on the initial null hypersurface by relaxing the no-ingoing-waves condition used in performing CCE. In addition, we can study the trade-off involved in choosing an earlier ringdown time, which will decrease the spread in recovered ringdown parameter posterior distributions and increase the systematic errors that arise because of deviations from Kerr in the strong-field region.

The methods used in this chapter can be applied to future BBH detections in order to guide the choice of the start time of ringdown. For the sake of quick reference to the procedure described in this chapter, we concisely enumerated the steps in Sec. 4.2.4. Note that the results of this chapter approximately hold for any equal mass system with an appropriate mass rescaling (cf. footnote 2) and effective spin near zero. The analysis presented, however, is fully generic and holds for all spins and masses. Our method would better allow one to perform precision tests of GR that depend on being in perturbative regime, such as tests of the no-hair theorem and area theorem. With this procedure, we provide an algorithmic way to check whether an unexpected deviation in a QNM analysis is due to not being in the perturbative regime, rather than due to a violation of GR or corresponding theorems.

For future detections, we plan to repeat this analysis using an NR simulation with the MAP waveform parameters.

Chapter 5

On spectroscopic analysis of stellar mass black-hole mergers

5.1 Introduction

The recent detection of gravitational waves from the coalescence of binary black-holes [134, 159] stand as the first stringent test of the validity of the General Theory of Relativity in the regime of strong-field gravity [160, 161, 43]. We investigate whether detections of stellar-mass black-holes can be used to experimentally confirm some fundamental predictions of this theory like the uniqueness theorem and the no-hair theorem [162, 163]. The no-hair theorem states that a space-time dictated by an isolated and stationary black-hole is fully characterized by just three parameters - the mass, the spin and the charge of the black-hole [164, 165]. Verifying the no-hair theorem would place strong constraints on possible alternative theories of gravitation [166, 167]. In a binary black-hole system, the two black-holes orbit around each other eventually merging and settling down to a final stationary Kerr black-hole. This post-merger signal, often called ringdown, contains information about the final Kerr black-hole formed by the coalescence of the progenitor black-holes [168], presenting us with an opportunity to verify the no-hair theorem. In light of these observations, efforts were made to study the ringdown signal. Although the features of the black-hole ringdown were discernible and had frequencies in a favorable regime of the detector's response, the signal-to-noise ratios (SNRs) of the signal in the two Laser Interferometer Gravitational-wave Observatory (LIGO) detectors were inadequate to perform a detailed ringdown analysis to draw firm conclusions about the final black-hole properties [161].

The ringdown signal seen by a distant observer during the coalescence of a binary black-hole system can be modeled as the gravitational waves arising from the perturbations, on the metric, associated with the final Kerr black-hole [169]. At spatial asymptotic infinity, these perturbations on the Kerr background manifest themselves as superpositions of damped sinusoidal oscillating modes, known as quasi-normal-modes (QNMs) [170, 171, 88, 172, 173, 174]. Assuming the General Theory of Relativity is valid, the no-hair theorem necessitates that the spectrum of frequencies and the damping of these modes be dictated entirely by the mass and the spin of the final Kerr black-hole formed. Thus, a spectral analysis of the ringdown part of the signal not only helps us to understand the properties of the final black-hole formed, but also can serve as a test of the no-hair theorem.

We attempt to address the following three questions. What are the prospects of performing black-hole spectroscopy using future ground-based gravitational-wave detectors? Which of the modes contained in the ringdown are likely to be measurable? What is the frequency range that should be targeted to optimize sensitivity of ground-based detectors to test the no-hair theorem with the ringdown signal?

Our study concentrates on stellar mass black-hole mergers in our local universe. We focus our analysis on the measurability of the three largest sub-dominant modes: $l = m = 3$, $l = m = 4$ and $l = 2, m = 1$. We perform a Monte-Carlo injection of 10^6 analytical post-merger gravitational wave signals, which are modeled as damped sinusoids with frequencies and damping times predicted by the linear perturbation theory on the Kerr background [175]. We do a mode-by-mode analysis; we consider each mode separately to assess its detectability and resolvability from the fundamental $l = m = 2$ mode. We calculate the fraction of simulated signals that allow for measurability of at least one sub-dominant mode as well as the the dominant $l = m = 2$ mode. We repeat this study with different proposed ground-based detectors - A+ [44], Einstein Telescope [45] and Cosmic Explorer [6]. A mode is considered detectable if its SNR is greater than 5 and resolvable if it satisfies the Rayleigh resolvability criterion [176, 177] described in Section II. If a mode satisfies both of these conditions, we identify that mode as measurable. A signal with more than one measurable mode is spectroscopically valuable. Using the range of binary black-hole coalescence rates [2] measured by Advanced LIGO [178], we estimate the number of spectroscopically valuable events per year.

Although it is improbable that we detect signals of spectroscopic value with Advanced LIGO, we estimate that hundreds of such signals will be detected by the future ground-based detectors such as Einstein Telescope and Cosmic Explorer every year. We deduce that the

modes with $l = m = 3$ and $l = 2, m = 1$ are the most promising candidates for sub-dominant mode measurability. Further, we find the measurability of the $l = 2, m = 1$ mode is not impeded by the resolvability criterion. We find that sub-dominant mode detectability is a sufficient condition to ensure measurability for all the modes considered in our study. We propose that a detector de-tuning around a frequency range of 300-500 Hz would be optimal for ringdown-oriented searches.

Our work is complimentary to the recent work by Berti et al. [179]. We perform a numerical Monte-Carlo simulation over sky positions and orientations and assume a uniform distribution of component masses of progenitor black-holes, while Berti et al. perform an approximate analytical angle-averaged analysis for different astrophysical black-hole population models. We have used a method of mode-by-mode matched filtering followed by a Fisher matrix analysis [180] to arrive at our results, in contrast to hypothesis testing and generalized likelihood used in [179]. Another novel aspect of our work is that we include the $l = 2, m = 1$ sub-dominant mode. Although the two analyses differ in their methods, we agree on the result that a detector beyond Advanced LIGO is essential for spectroscopic analyses of black-hole mergers.

The remainder of this chapter is structured in the following way. In Section II we provide a detailed description of the analysis methods used in our study. Section III presents our results and highlights their implications to the broader theme of black-hole spectroscopy. We then conclude in Section IV on the prospects of stellar mass black-hole spectroscopy in our local universe with next-generation ground-based gravitational-wave detectors.

5.2 Methods

We perform Monte-Carlo injections of ringdown-only gravitational-wave signals corresponding to stellar mass binary black-hole mergers in our local universe. Specifically, 10^6 binary black-hole merger events are simulated uniformly in a volume defined by a sphere of radius 1500 Mpc around the the detector in question. Focusing our study on stellar mass mergers, we choose the component masses of the progenitor binary systems to be a uniform random distribution between $10 M_{\odot}$ and $60 M_{\odot}$. Our study is limited to systems whose progenitor binaries are non-spinning, although we expect the qualitative results to hold for spinning cases. The sky positions and orientations of progenitor binaries with respect to the detector are also assumed to have a uniform random distribution. The analysis is performed independently for two future generation detectors - Einstein Telescope and Cosmic Explorer, a proposed upgrade to the current Advanced LIGO detector that we refer to as A+ and the design sensitivity of

Advanced LIGO. Further, it is desirable to investigate which part of the detector’s frequency range needs to be tuned for a ringdown-optimized search in addition to discerning which mode is more measurable, independent of the detector’s sensitivity curve. For that reason, we also repeat the entire analysis on an unrealistic flat noise spectrum with a strain amplitude of 10^{-25} per $\sqrt[2]{\text{Hz}}$ and present its results. For comparison, we display the relative sensitivities of all the detector curves used in our study in Figure 28.

We assume the binary black-hole ringdown signals observed by gravitational-wave detectors comprise of linear superpositions of a finite number of QNMs. Despite the mathematical issues, such as the incompleteness of QNMs [181, 58], it is known that for binary black-hole mergers this is a good approximate model [182, 183]. We test each mode independently for its measurability. Since we conduct a mode-by-mode analysis, we model the signal waveform as a single damped sinusoid of the following form:

$$h_{lm}^{(+,\times)}(t) = \frac{M}{r} \left[A_{lm}^{(+,\times)} \sin(2\pi f_{lm}t) e^{\frac{-t}{\tau_{lm}}} \mathcal{Y}_{lm}(\iota, \beta) \right]. \quad (5.1)$$

Here $A_{lm}^{+,\times}$, f_{lm} and τ_{lm} denote the amplitudes associated with the two polarizations, the central frequency and the damping-time, respectively, of the dominant overtone of (l, m) modes in a black-hole ringdown. (ι, β) specify the orientation of the progenitor binary system in the sky. Further, we approximate the spheroidal harmonic function associated to each mode by spin-2 weighted spherical harmonics $\mathcal{Y}_{lm}(\iota, \beta) = \mathcal{Y}_{lm}(f_{lm}; \iota, \beta)$, which is a good first order approximation for Kerr black-holes that are not extremally spinning [184].

We calibrate the central frequency and the decay time of each mode using the fitting functions presented in [8]. Ref. [7] presents mode amplitudes as functions of symmetric-mass-ratios η of the progenitor binary system by fitting 68 numerical relativity waveforms corresponding to non-spinning black-hole binary systems. We have used the corrected formulae from the erratum [185] for our analysis. The start-time of all modes are chosen to be 10 M after the occurrence of the peak in luminosity corresponding to the $l = m = 2$ mode. We use these fitting formulae to determine the mode amplitudes A_{lm} in our waveform model. Figure 33 presents the mode amplitudes of the sub-dominant modes. Dictated by the symmetry of the initial perturbation, the $l = m = 2$ mode is the dominant mode in the ringdown of a Kerr black-hole formed during the merger of a binary black-hole system. Based on the sub-dominant mode amplitudes, we limit the scope of this study to $l = m = 3$, $l = m = 4$ and $l = 2, m = 1$ sub-dominant mode measurability.

The signal $h(t)$ observed at a detector is then given as,

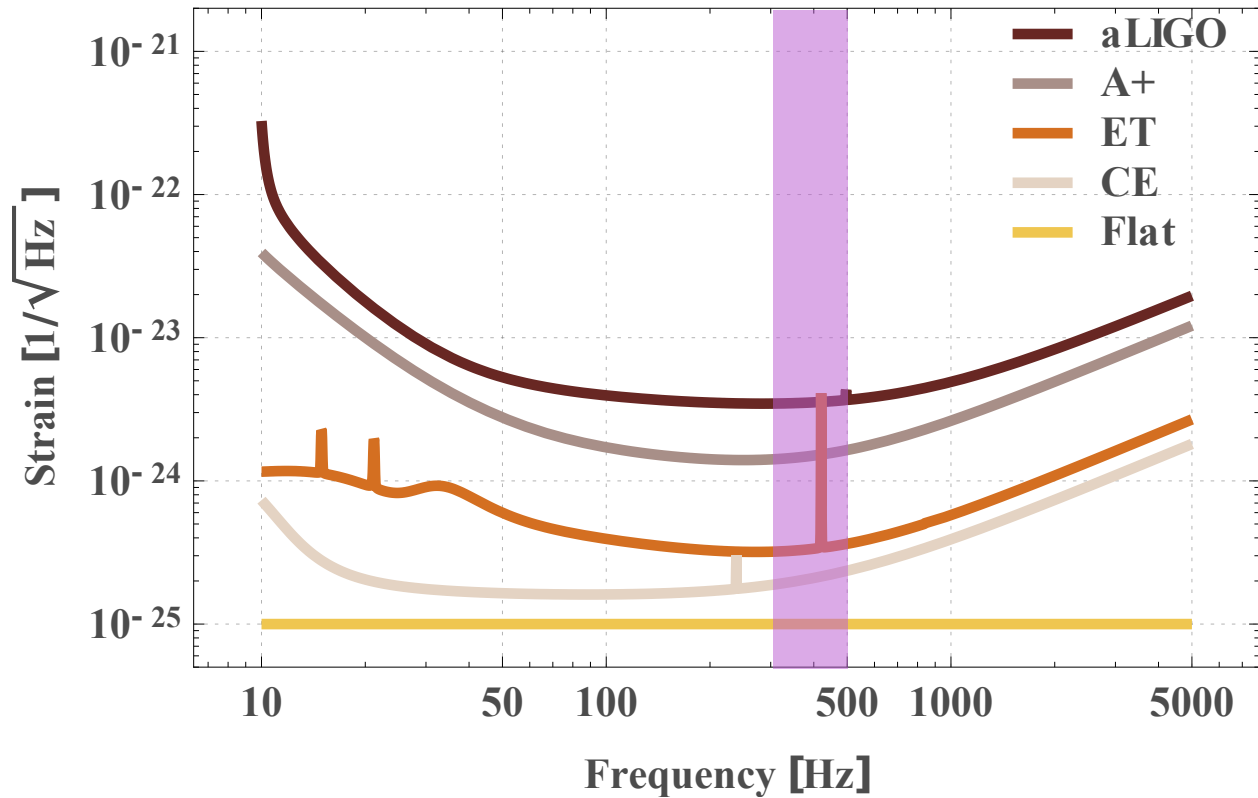


Figure 28: The following are sensitivity models for each detector [6] we consider in our study. The aLIGO curve corresponds to the design sensitivity of Advanced LIGO and the A+ curve to the proposed upgrade to the Advanced LIGO detectors. The Cosmic Explorer (CE) and the Einstein Telescope (ET) are two of the proposed next generation ground-based detectors. We also perform the analysis with a flat noise curve at a strain per $\sqrt{\text{Hz}}$ of 10^{-25} , to infer some conclusions which are independent of the shape of the noise curve. The shaded region shows the frequency band that corresponds to optimal tuning of the detectors for ringdown searches.

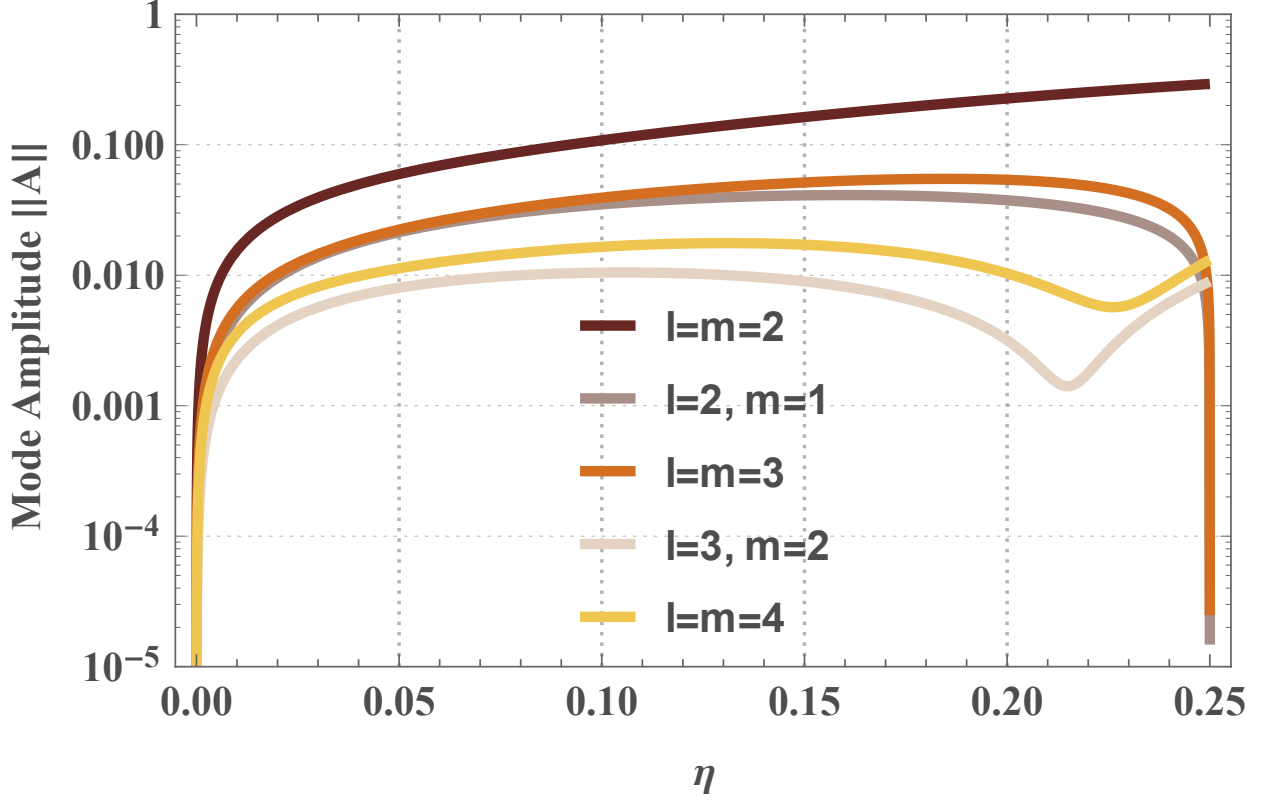


Figure 29: This figure presents the magnitude of mode amplitudes $\|A\|$ predicted by the fitting formulae given in [7] as a function of dimensionless symmetric-mass-ratio η . Comparing the amplitudes of different modes, we infer that the potential candidates for sub-dominant mode measurability correspond to $l = m = 3$, $l = 2, m = 1$ and $l = m = 4$.

$$h(t) = F_+ h_+(t) + F_\times h_\times(t), \quad (5.2)$$

where $F_{+,\times}$ are orientation-dependent detector pattern functions that project the signal on to the detector.

Expressing this in the Fourier domain, we obtain

$$\tilde{h}_+(f) = \frac{M}{r} A_{lm}^+ \left[e^{i\phi_{lm}^+} \mathcal{Y}_{lm} b_+ + e^{-i\phi_{lm}^+} \mathcal{Y}_{lm}^* b_- \right] \quad (5.3)$$

$$\tilde{h}_\times(f) = -i \frac{M}{r} A_{lm}^\times \left[e^{i\phi_{lm}^\times} \mathcal{Y}_{lm} b_+ - e^{-i\phi_{lm}^\times} \mathcal{Y}_{lm}^* b_- \right], \quad (5.4)$$

where

$$b_{\pm} = \frac{2/\tau_{lm}}{(1/\tau_{lm})^2 + 2\pi(f \pm f_{lm})^2} \quad (5.5)$$

and ϕ_{lm}^+ and ϕ_{lm}^{\times} are phase of arrival associated with $\tilde{h}_+(f)$ and $\tilde{h}_{\times}(f)$ respectively. We follow [186] in setting up the framework for our analysis.

We use the standard expression for SNR ρ

$$\rho^2 = 4 \int_0^{\infty} \frac{\tilde{h}^*(f')\tilde{h}(f')}{S_h(f')} df' = \langle h|h \rangle, \quad (5.6)$$

where $\tilde{h}(f)$ is the Fourier transform of the waveform and $S_h(f)$ is the power spectral density of the detector [187]. A mode is considered detectable if the single detector SNR of that mode exceeds a pre-defined threshold for detection. We choose $\rho \geq 5$ as our threshold and each mode is independently checked for this detectability criterion. Once a sub-dominant mode

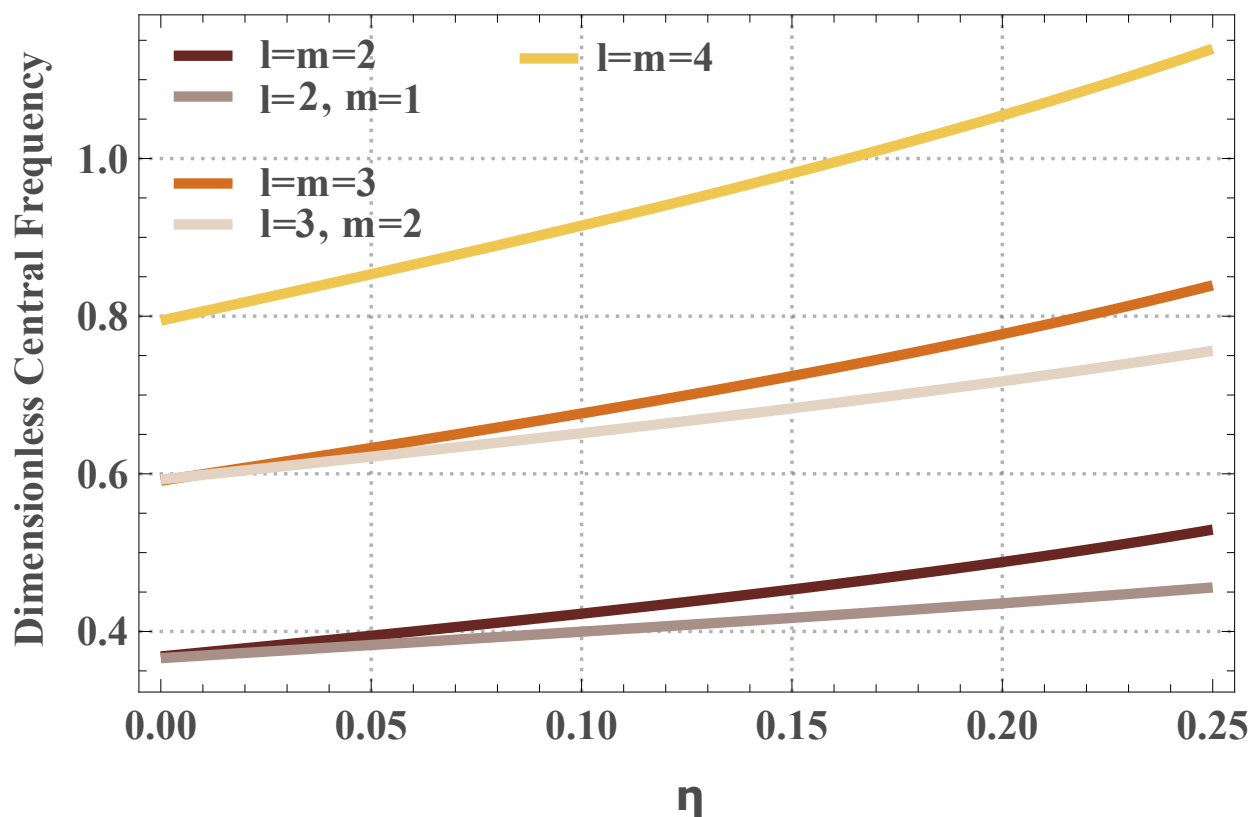
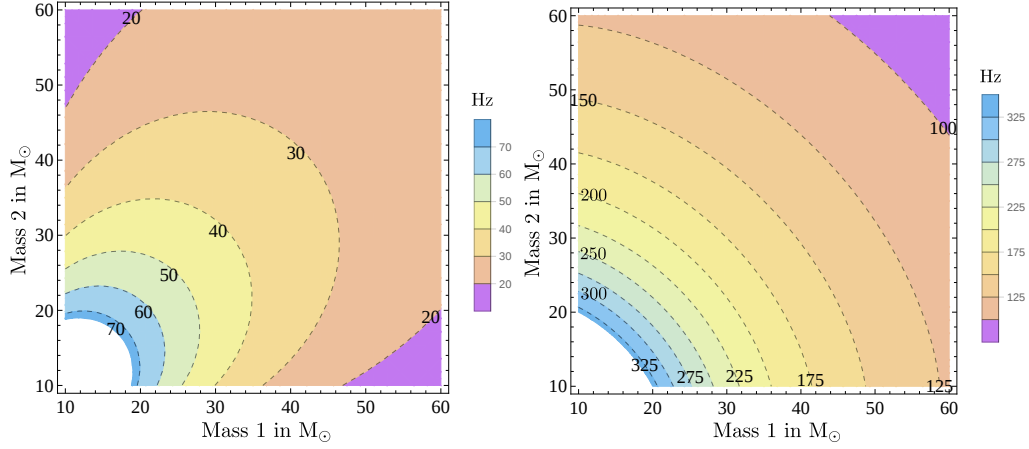
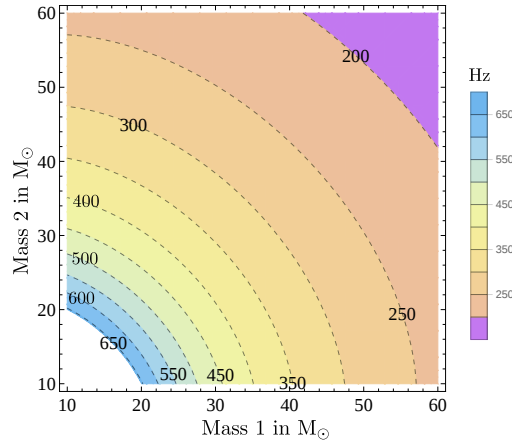


Figure 30: We show the dimensionless central frequency of QNMs as a function of symmetric-mass-ratio η as predicted by [8]. Note that modes with different l have central frequencies that are well separated. One could naively expect that resolving modes with the same l could be challenging. However, for stellar mass black-hole mergers this is not the case.



a) Difference between central frequencies of $l = m = 2$ and $l = 2, m = 1$ modes in Hz. b) Difference between central frequencies of $l = m = 2$ and $l = m = 3$ modes in Hz.



c) Difference between central frequencies of $l = m = 2$ and $l = m = 4$ modes in Hz.

Figure 31: These contour plots show the differences in the central frequencies of the sub-dominant modes: $l = 2, m = 1$, $l = m = 3$ and $l = m = 4$, with the dominant mode. The color bar presents a measure of frequency difference in Hz. Notice that the central frequency of the $l = m = 3$ and $l = m = 4$ sub-dominant mode differs from the dominant mode by hundreds of Hz. It would be right to assume that resolvability of these modes is not challenging. However, it is very interesting to note that even for the $l = 2, m = 1$ sub-dominant mode the central frequency is separated by at least 20 Hz from the central frequency of the dominant mode. This is consistent with the fact that our results indicate that resolvability is not a limiting factor.

passes this criterion for detectability, we then proceed to check that its central frequency is resolvable from that of the dominant mode.

We use an extension of Rayleigh criterion developed in [8, 176, 177] to establish the limits of resolvability. The Rayleigh criterion for diffraction states that to distinguish two points, the diffraction maxima of the second point should lie at least at the minima of the first point [180]. This translates to a condition that the peak of the estimators of QNM frequencies should be separated by at least the largest of their variances. If $\sigma_{f_1}^2$ and $\sigma_{f_2}^2$ are the variances of the maximum likelihood estimators of f_1 and f_2 associated with the modes under investigation, then the minimum criterion for resolvability is given by,

$$\frac{\mathbf{max}[\sigma_{f_1}, \sigma_{f_2}]}{|f_1 - f_2|} = 1. \quad (5.7)$$

In the scheme of Fisher information theory, the spread σ_{f_i} in the estimate of the frequency f_i is given by

$$\sigma_{f_i}^2 = \Gamma_{f_i f_i}^{-1}, \quad (5.8)$$

where Γ is the Fisher matrix [188]. To compute the Fisher matrix, we parametrize the waveform by the mode amplitude, frequency, quality factor, arrival time and phase. The likelihood function has peaks around the central frequency of each of the QNMs. We perform a Fisher matrix analysis around each of these mode frequencies to determine the spread in the estimate of the central frequency of the modes. Then it follows that the critical SNR ρ_c that sets the resolvability limit of these modes is given by,

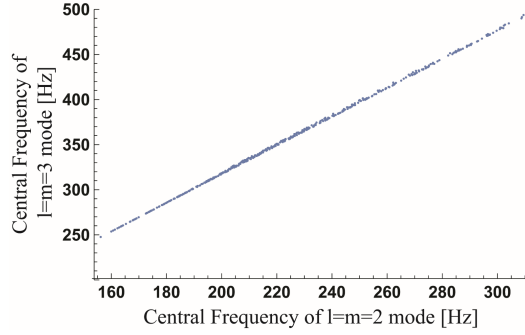
$$\rho_c = \frac{\mathbf{max}[\rho\sigma_{f_1}, \rho\sigma_{f_2}]}{|f_1 - f_2|}. \quad (5.9)$$

A dimensionless ratio \mathcal{R} determines the resolvability of QNMs:

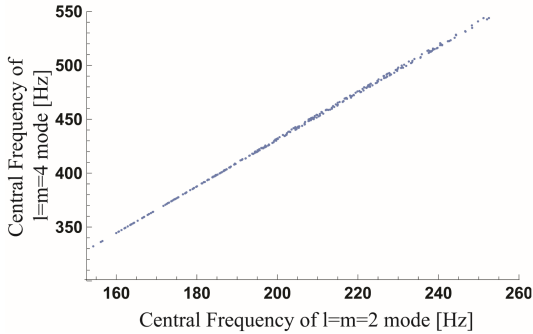
$$\mathcal{R} = \frac{\rho}{\rho_c} = \frac{|f_1 - f_2|}{\mathbf{max}[\sigma_{f_1}, \sigma_{f_2}]}. \quad (5.10)$$

When \mathcal{R} is greater than 1, the central frequency of the sub-dominant mode in the signal can be successfully resolved from the dominant mode.

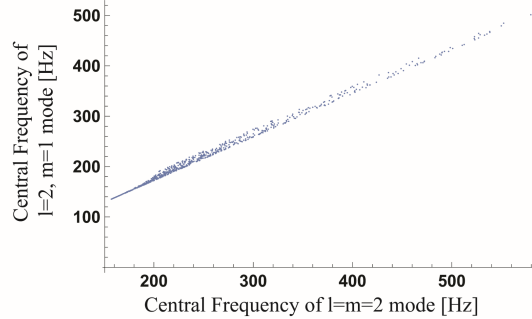
Having established our criteria of detectability and resolvability, we perform a mode-by-mode analysis on each of the injected signals with the detector curves depicted in Figure 28. Equations (6) and (10) are evaluated numerically and for each mode we test if $\rho_{lm} > 5$ and $\mathcal{R} > 1$ to determine their measurability. We then categorize the signals based on their measurability.



a) Central frequencies of modes $l = m = 3$ and $l = m = 2$ in Hz.



b) Central frequencies of modes $l = m = 4$ and $l = m = 2$ in Hz.



c) Central frequencies of modes $l = 2, m = 1$ and $l = m = 2$ in Hz.

Figure 32: Scatter plots of all points that allow for measurability of sub-dominant modes in our analysis using a flat detector sensitivity curve at a strain of $10^{-25} \sqrt[2]{\text{Hz}}^{-1}$. The x and y axes of these plots correspond to the central frequencies of $l = m = 2$ and the measurable sub-dominant modes in Hz respectively. From these plots, we can infer that if one were to perform detector de-tuning optimized towards a spectroscopic analysis of stellar mass black-holes, a frequency band around 300 Hz to 500 Hz would be the best choice for narrow banding.

5.3 Results and Implications

We find that we are able to measure sub-dominant modes during the ringdown of stellar mass Kerr black-holes with the proposed designs for future ground-based gravitational wave detectors. The results are summarized in Tables 1-4. With detectors like Cosmic Explorer and Einstein Telescope, we find that approximately 20-30% of the total detected stellar mass black-hole mergers will be spectroscopically valuable. Our results also indicate that the

design sensitivity of Advanced LIGO might detect signals that would allow for multi-mode measurements if the optimistic rate predictions hold. However, implementing A+ to the detector would increase our odds of sub-dominant mode measurability to a little less than 3% of the total detected black-hole mergers.

The astrophysical rates of stellar mass black-hole mergers have significant uncertainty and hence, in Table 3, we tabulate both the optimistic and pessimistic rates of events that would allow for ringdown spectroscopy of the final Kerr black-hole using various proposed ground-based detectors. With an optimistic rate of $240 \text{ Gpc}^{-3}\text{yr}^{-1}$ merger events [2], we expect about a thousand events per year will be spectroscopically valuable with Einstein Telescope and Cosmic Explorer. It is further encouraging to notice that, with the implementation of the A+ upgrade to the current detectors, an optimistic rate would indicate that about an order of 50 spectroscopically valuable events will be detected every year. Further, even a pessimistic rate of only $13 \text{ Gpc}^{-3}\text{yr}^{-1}$ binary black-hole mergers, leads us to estimate about 40-60 events that allows for multi-mode measurements using Einstein Telescope and Cosmic Explorer.

From our analysis using a flat detector curve depicted in Figure 28 we infer, independent of proposed-detector sensitivities, that the $l = m = 3$ sub-dominant mode has the most measurability, closely followed by the sub-dominant mode with $l = 2, m = 1$. An optimistic rate of $240 \text{ Gpc}^{-3}\text{yr}^{-1}$ merger events suggests that nearly 650-1000 events would allow for measurability of the $l = m = 3$ sub-dominant mode and about a 100-250 would allow for measurability of the $l = m = 4$ mode each year with Cosmic Explorer and Einstein Telescope. Furthermore, analyzing the mode $l = 2, m = 1$, we find that its measurability with Cosmic Explorer is about 1000 events per year and that with Einstein Telescope is about a 500 events per year. A few of the existing literature [189, 179] have not considered the sub-dominant mode corresponding to $l = 2, m = 1$ in their studies. Our study highlights that for the detection of stellar mass black-hole mergers with Cosmic Explorer, the $l = 2, m = 1$ is the most promising mode. From Figure 33, we can see that the $l = 2, m = 1$ sub-dominant mode has a slightly smaller mode amplitude compared to the $l = m = 3$ mode. However it should also be noted that it is the least damped sub-dominant mode. Thus, for noise curves such as that of Cosmic Explorer, where the detector has a favorable sensitivity in lower frequencies, the odds of measuring the $l = 2, m = 1$ sub-dominant mode is markedly elevated.

In contrast to the naive expectation formed by looking at Figure 30, we find that the frequency of the sub-dominant mode corresponding to $l = 2, m = 1$ is well separated from the central frequency of the dominant mode for the case of stellar mass black-hole mergers. For all the sub-dominant modes, including $l = 2, m = 1$ we notice that detectability is the primary

condition that limits mode measurability and that only very few signals fail measurability due to the resolvability criterion. Figure 31 shows that even for $l = 2, m = 1$ mode, the central frequency of the dominant and sub-dominant mode differ by at least 20 Hz for all cases considered in our study. Thus, resolvability does not seem to crucially effect measurability of the modes. This result might be advantageous while developing new data-analysis techniques to measure sub-dominant modes for stellar mass black-hole mergers because it indicates that checking detectability is sufficient and removes an additional layer of complexity of having to check mode resolvability. However, resolvability could indeed become a potential challenge if one were to deal with super-massive black-holes targeted by planned space-based detectors. In such cases a more carefully designed data-analysis technique needs to be developed.

Finally, we address the question of which frequency band should be targeted for a ringdown oriented detector de-tuning. For a spectroscopic analysis of black-hole ringdowns, our focus should be on measuring the sub-dominant modes because their single-mode SNRs are generally much smaller than the dominant mode. The scatter plots in Figure 32 capture the information of mode frequencies corresponding to the population of signals that passed our measurability criterion. Again, this plot is made using a flat sensitivity curve to arrive at a conclusion that is independent of the shape of the detector noise curve. Looking at the central frequencies of sub-dominant modes $l = m = 3$ and $l = m = 4$ of signals that passed out measurability criterion in Figure 30 and Table 2, we propose that an increase in sensitivity around 300 Hz and 500 Hz would enhance the measurability of both $l = m = 3$ and $l = m = 4$. Measurability of $l = 2, m = 1$ sub-dominant mode however would benefit from detector de-tuning around 150-300 Hz. Considering that the joint measurability of sub-dominant modes $l = m = 3$ and $l = m = 4$ seems more promising, it can be inferred that a frequency band between 300 Hz and 500 Hz is the best target for detector tuning optimized for spectroscopic analysis of stellar mass black-holes. This result for frequency tuning relies on the assumption that the the initial black holes are uniformly distributed in the mass range of 10 to 60 M_{\odot} . Using a different astrophysical source distribution will lead to different optimal frequency bands, since the distribution of QNM frequencies depend on the masses of progenitors. Our method can be used to compute this frequency tuning for other mass distributions.

5.4 Conclusion

In this chapter we have investigated the prospects of our ability to perform black-hole spectroscopy using the current and future ground-based gravitational-wave detectors. We find that with a realistic rate of binary black-hole mergers, one could expect to detect several

tens of spectroscopically valuable signals with future ground-based detectors like Einstein Telescope and Cosmic Explorer. Although Advanced LIGO might detect signals that would allow for multi-mode measurements only if the optimistic rates hold, implementing A+ upgrade increases our odds of detecting such signals. From the results of this study, we also conclude that sub-dominant modes corresponding to $l = m = 3$ and $l = 2, m = 1$ offer the most measurability. We emphasize that resolvability is not a limiting factor for stellar mass black-hole mergers for all the modes we have considered in our study. Further, we propose that a detector de-tuning around a frequency band between 300 Hz and 500 Hz is optimal for a ringdown-oriented search.

In this study we have used the choice made in [7] that all modes of ringdown begin 10 M after the peak of luminosity corresponding to the $l = m = 2$ mode. This choice was motivated by the work pioneered in [95]. Although there is no absolute framework to choose the start time of the ringdown, this is a conservative choice. Even with this conservative choice, we find an encouraging rate of detectable spectroscopically valuable signals using the future ground-based detectors. We intend to explore alternative choices, such as in [190] in a future study and we expect this will improve the chances of measuring sub-dominant modes significantly. Further, this study is done in the scheme of the Fisher information theory. Future work will follow this study with a full Bayesian parameter estimation like that in [191] and a comparison of the results.

Detector Curve	Set 1	Set 2	Set 3	Set 4	Set 5	Set 6
Advanced LIGO	0.83	0.16	0.0008	2×10^{-5}	1.6×10^{-5}	0
A+	0.6	0.37	0.01	0.0004	0.0001	0
Einstein Telescope	0.32	0.47	0.18	0.03	0.01	2×10^{-4}
Cosmic Explorer	0.3	0.44	0.3	0.08	0.04	5×10^{-6}
A flat noise curve at $10^{-25} \sqrt[2]{\text{Hz}^{-1}}$	0.17	0.35	0.41	0.06	0.18	0.001

Table 7: The above table shows the results we obtain from a Monte-Carlo simulation of 10^6 stellar mass binary black-hole mergers uniformly distributed in component mass, orientation and in volume defined by a sphere of radius 1500 Mpc. We categorize each event into one of the set defined below and tabulate the fraction of signals that fall into each set. Set 1: $l = m = 2$ mode could not be detected, Set 2: $l = m = 2$ could be detected but no other sub-dominant mode could be detected, Set 3: $l = m = 3$ sub-dominant mode can be measured, Set 4: $l = m = 4$ sub-dominant mode can be measured, Set 5: Both $l = m = 3$ and $l = m = 4$ sub-dominant modes can be measured, Set 6: failed measurability of sub-dominant mode due to resolvability criterion.

Detector Curve	Set 1	Set 2	Set 3	Set 4
Advanced LIGO	0.84	0.15	1.8×10^{-4}	0
A+	0.59	0.4	0.004	0
Einstein Telescope	0.31	0.52	0.16	0
Cosmic Explorer	0.24	0.41	0.34	0
A flat noise curve at $10^{-25} \sqrt[2]{\text{Hz}^{-1}}$	0.14	0.33	0.52	0

Table 8: The above table has information similar to Table 1 but with sets defined differently. Here, Set 1: $l = m = 2$ mode could not be detected, Set 2: $l = m = 2$ could be detected but $l = 2, m = 1$ sub-dominant mode could be detected, Set 3: $l = 2, m = 1$ sub-dominant mode is both detected and resolved, Set 4: $l = 2, m = 1$ sub-dominant mode is detected but not resolved. Here again, we tabulate the number of events out of 10^6 Monte-Carlo simulated binary black-hole mergers that fall in each of these sets.

Detector Curve	Optimistic Rate	Pessimistic Rate
Advanced LIGO	2.9/yr	0.2/yr
A+	47.3/yr	2.6/yr
Einstein Telescope	694.3/yr	37.6/yr
Cosmic Explorer	1130/yr	61.2/yr
A flat noise curve at $10^{-25} \sqrt{\text{Hz}}^{-1}$	1570/yr	85 /yr

Table 9: Using our results in Table 1 and the optimistic (pessimistic) rates of binary black-hole mergers, predicted based on the recent discoveries of binary black-hole mergers [2], at $240 \text{ Gpc}^{-3} \text{ yr}^{-1}$ ($13 \text{ Gpc}^{-3} \text{ yr}^{-1}$), we present the rate of events that would allow measurability of $l = m = 3$ or $l = m = 4$ sub-dominant mode with current and future ground-based detectors. We present this combined ($l = m = 3$ or $l = m = 4$) rate, because de-tuning the detector around the frequency band $300 - 500 \text{ Hz}$ for a ringdown oriented search benefits both of these modes.

For $l = m = 3$	Optimistic Rate	Pessimistic Rate
Advanced LIGO	2.9/yr	0.2/yr
A+	46.4/yr	2.5/yr
Einstein Telescope	645.4/yr	34.9/yr
Cosmic Explorer	1024.3/yr	55.5/yr
A flat noise curve at $10^{-25} \sqrt[2]{\text{Hz}^{-1}}$	1409.2/yr	76.3/yr
For $l = m = 4$	Optimistic Rate	Pessimistic Rate
Advanced LIGO	0.08/yr	0.004/yr
A+	1.4/yr	0.08/yr
Einstein Telescope	96.7/yr	5.2/yr
Cosmic Explorer	263.1/yr	14.2/yr
A flat noise curve at $10^{-25} \sqrt[3]{\text{Hz}^{-1}}$	605.7/yr	32.8/yr
For $l = 2, m = 1$	Optimistic Rate	Pessimistic Rate
Advanced LIGO	0.6/yr	0.03/yr
A+	13.4/yr	0.7/yr
Einstein Telescope	545.6/yr	29.6/yr
Cosmic Explorer	1162.7/yr	63/yr
A flat noise curve at $10^{-25} \sqrt[2]{\text{Hz}^{-1}}$	1772.3/yr	96/yr

Table 10: Using our results in Table 2 and the optimistic (pessimistic) rate of binary black-hole mergers, predicted based on the recent discoveries of binary black-hole mergers [2], at $240 \text{ Gpc}^{-3} \text{ yr}^{-1}$ ($13 \text{ Gpc}^{-3} \text{ yr}^{-1}$), we present the rate of events that would allow measurability of single sub-dominant modes.

Chapter 6

On detectability of the subdominant mode in a binary black hole ringdown

6.1 Introduction

At a sufficiently late time, the post-merger signal emitted during the coalescence of a binary black hole (BH) system can be modelled by linear perturbation theory [88, 91, 162]. We refer to this part of the postmerger as the ‘ringdown’ (RD) in this study. The equation governing the perturbation on a Kerr manifold when cast in form of a radiative boundary-value-problem takes a form similar to the Schrodinger equation with an effective BH potential [85, 86, 87]. The BH quasi-normal modes (QNM) are the solutions to this equation and observing them serves as a probe to understand the linear perturbative dynamics of the strong field gravity [30, 31, 32, 103, 168].

By observing the QNM spectrum, we test the validity of the equation governing the evolution of perturbations, which in turn, is obtained from Einstein’s equation. We also test the shape of effective BH potential which encodes the nature and the geometry of the central compact object. Further, the boundary conditions used to solve this equation is dictated by the presence or absence of an event horizon. Moreover, observing a QNM spectrum consistent with a BH validates that the perturbative dynamics on a Kerr geometry can be parametrised by just two parameters; the mass and spin of the final BH the no-hair theorem [164], thereby, observationally verifying the no-hair theorem.

Since the discovery of gravitational waves (GW) from the binary BH systems, many studies have been performed to understand and infer the nature of BH RDs [79, 94, 199, 156, 93, 61, 42, 179]. In GW1501914 signal, the frequency and damping of the dominant QNM has

been measured and confirmed to be consistent with GR within the error bars of measurement [5]. However, the measurement errors were large; ~ 40 Hz in the frequency and ~ 6 ms in the damping time. No subdominant mode was inferred. Improving the accuracy in the measurement of the dominant mode and measuring at least the second most dominant mode (we refer to this as the sub-dominant mode throughout this text) in the QNM spectrum, will allow us to test GR rigorously.

The prospects of measuring the subdominant mode depend principally on the overall SNR present in the RD ρ_{RD} and the mode excitation amplitude of the subdominant mode. For instance, an nearly equal mass binary system like the GW150914 does not excite the subdominant modes sufficiently and thus, is not ideal for inferring multiple modes in the QNM spectrum. As a rule of thumb, the higher the asymmetry in the progenitor system, the lower is the ρ_{RD} needed to detect the subdominant modes. In this paper, we present a study on the interplay of these two factors to understand what kind of RD signals will enable us to perform a multimode detection in RD.

The inspiral-merger phase sets the initial conditions for the perturbation, thus, deciding the intrinsic amplitude of excitation of different QNMs. There are phenomenological fits that relate the mass ratio q of the progenitor BHs to the ratio of the intrinsic amplitudes of excitation $A_R = \frac{A_{33}}{A_{22}}$ in the framework of GR [155]. However, note that the observed subdominant mode amplitude also depends on the inclination angle (ι) extrinsically through the spherical harmonic function ¹ (see Figure 3 of [155]).

We study the effect of varying A_R and ρ_{RD} on the recovery of intrinsic parameters in RD, with a particular interest in the parameters that describe the subdominant mode i.e., the A_R and the phase of the subdominant mode ϕ_{33} . We perform a full Bayesian Parameter Estimation (PE) on a set of two-mode RD injections. For this study, we fix the mass $M_f = 70M_\odot$ and the dimensionless spin $a_f = 0.65$ of the final BH formed. We assume that the underlying theory of gravity is GR and compute the frequencies (ω_{lm}) and damping times (τ_{lm}) as dictated by linear perturbation theory for a given BH [89, 183].

Furthermore, we argue that even though we fix M_f and a_f for this study, the result should approximately hold true for a general case. We expect this because most of the SNR in the RD comes from the beginning of the signal and therefore, the analysis is not particularly sensitive to the exact value of frequency or damping time. The dominant mode and the subdominant mode are separated sufficiently in frequencies that they are always

¹A natural basis function to decompose ringdown is a weighted spheroidal harmonic functions; however, we approximate it with spin2-weighted spherical harmonic function. For details of mode-mixing due to this approximation, refer to [184].

resolvable [62]. Since the log-likelihood scales as the square of SNR, to first order, we expect the parameter estimation to be sensitive to just ρ_{RD} and A_R .

This chapter is organized in the following way: In section 6.2 we describe the theory of Bayesian PE. In section 6.3, we describe the injections used in this study and the details of the setting we employ for our PE. Next, in section 6.4 we present our results and finally discuss its implication in section 6.5.

6.2 Theory

6.2.1 Parameter Estimation

Given a GW observation in form of a timeseries data \mathcal{D} ², one can use the framework of Bayesian inference to estimate the properties of the BBH system. Let \mathcal{H} be a model that we believe describes the observation and let the model be parameterized by the parameters $\boldsymbol{\vartheta}$. One can use Bayesian inference to compute the posterior probability density function (PDF) and infer the parameters $\boldsymbol{\vartheta}$ given an observation. In this section, we provide a brief introduction to Bayesian inference.

Bayesian inference relies on the philosophy that, given a \mathcal{H} , one has expectations on the distribution of parameter values before performing an observation [193, 194]. These expectations prior to performing the experiment is encoded in a probability density function called *the prior* $\mathcal{P}(\boldsymbol{\vartheta}|\mathcal{H})$. Once the observation is performed and the data set is obtained, one updates their beliefs with information obtained from this observation. This input is encoded in *the Likelihood function* $\mathcal{P}(\mathcal{D}|\boldsymbol{\vartheta}, \mathcal{H})$ and the inferred probability density for $\boldsymbol{\vartheta}$, often called *the posterior probability density function* $\mathcal{P}(\boldsymbol{\vartheta}|\mathcal{D}, \mathcal{H})$, is informed by both the prior and the likelihood function.

The Bayes theorem states that the posterior probability density function $\mathcal{P}(\boldsymbol{\vartheta}|\mathcal{D}, \mathcal{H})$ for the parameters $\boldsymbol{\vartheta}$ is given by [193, 194],

$$\mathcal{P}(\boldsymbol{\vartheta}|\mathcal{D}, \mathcal{H}) = \frac{\mathcal{P}(\boldsymbol{\vartheta}|\mathcal{H})\mathcal{P}(\mathcal{D}|\boldsymbol{\vartheta}, \mathcal{H})}{\mathcal{P}(\mathcal{D}|\mathcal{H})}. \quad (6.1)$$

Here, $\mathcal{P}(\mathcal{D}|\mathcal{H})$ is the *evidence* and serves as a normalization factor.

The likelihood function $\mathcal{P}(\mathcal{D}|\boldsymbol{\vartheta}, \mathcal{H})$ depends on both the signal and the nature of noise present in the data. Let timeseries data from the detector contain a GW signal $\boldsymbol{\mathcal{S}}$ embedded in the detector noise \mathcal{N} , i.e $\mathcal{D} = \boldsymbol{\mathcal{S}} + \mathcal{N}$. If the \mathcal{N} is Gaussian and stationary, the likelihood

²*Convention:* The boldfaced symbols in this section correspond to vectors.

function, $\mathcal{P}(\mathcal{D}|\boldsymbol{\vartheta}, \mathcal{H})$, can be written as

$$\mathcal{P}(\mathcal{D}|\boldsymbol{\vartheta}, \mathcal{H}) \propto e^{-\frac{1}{2}\langle \mathcal{N}|\mathcal{N} \rangle} = e^{-\frac{1}{2}\langle \mathcal{D}-\mathcal{S}|\mathcal{D}-\mathcal{S} \rangle}. \quad (6.2)$$

Here, $\langle \cdot \rangle$ denote the inner product weighted by the power spectral density (PSD) of the detectors. The form of the prior distributions, $\mathcal{P}(\boldsymbol{\vartheta}|\mathcal{H})$ is a choice that one has to make and there is no unique way to pick it. With the intention of extracting maximum information from the data itself, a non-informative prior is used in this study.

All the information about the distribution of the estimated parameters is contained in the landscape of $\mathcal{P}(\boldsymbol{\vartheta}|\mathcal{D}, \mathcal{H})$ and therefore, the goal of a scheme using Bayesian PE is to sample the parameters space of $\boldsymbol{\vartheta}$ and construct the distribution $\mathcal{P}(\boldsymbol{\vartheta}|\mathcal{D}, \mathcal{H})$ ³. In practice, these posterior distributions are computed by sampling [195] the allowed parameter space using routines for sampling employ an algorithm called the Markov Chain Monte Carlo (MCMC) [196, 197, 198]. In our study we employ a parallel tempered sampling algorithm called *emcee - pt*. Once we obtain the posterior distribution for the parameter, we use credible intervals infer the parameters of the model.

6.3 Methods

6.3.1 The Ringdown Injections

The injections used in this study contain only two QNM modes of RD, with the frequencies and the damping times calculated using the linear perturbation theory. Therefore, there is no non-linear merger physics in these injections. The RD injections correspond to a BH with $\{M_f = 70M_\odot, a_f = 0.65\}$. It must be highlighted that the intent of this paper is to investigate the detectability of a subdominant mode in BBH RD assuming that the underlying theory of gravity is GR.

Additionally, we fix the inclination angle ι for each of the injections to 0.7 and the sky position is chosen to be $\{RA = 2.2, Dec = -1.24\}$. The polarization angle ψ is set to 0.3. Note that these extrinsic parameters are chosen arbitrarily. Figure 3 of [155] presents the effect of the choice of ι on the observed amplitudes of QNM; we note that our choice of $\iota = 0.7$ is fairly favourable for viewing the subdominant mode $l = m = 3$. Therefore, it should be highlighted that the statements in this study are optimistic. The initial phase of

³In most cases where one is just interested in estimating the parameter values for $\boldsymbol{\vartheta}$, $\mathcal{P}(\boldsymbol{\vartheta}|\mathcal{D}, \mathcal{H})$ is calculated up to a normalization factor. Typically, one need not compute the evidence to estimate the parameters of the model. Moreover, calculating the evidence is computation challenging, especially when the parameter space spanned by $\boldsymbol{\vartheta}$ is large.

the dominant mode is set to 0 and that of the subdominant mode is set to 1. These choices are again arbitrary and we hold them fixed for all the injections used in this study. Further, this study is performed considering only the two LIGO detectors at their design sensitivity.

We then systematically vary the amplitude of the dominant mode such that the injections correspond to an optimal RD SNR of $\{15, 20, 25, 30\}$. Figure 33 plots the amplitude of QNMs in RD of the nonspinning BBH systems as a function of progenitor mass ratio η using the fitting formulae presented in [7]. For all the non-spinning BBH systems, $l = m = 3$ is the loudest subdominant mode. In our injections the dominant mode corresponds to $l = m = 2$ mode and the subdominant mode is $l = m = 3$. We study RDs with varying $A_R = A_{220}/A_{330} \in \{0.1, 0.2, 0.3\}$.

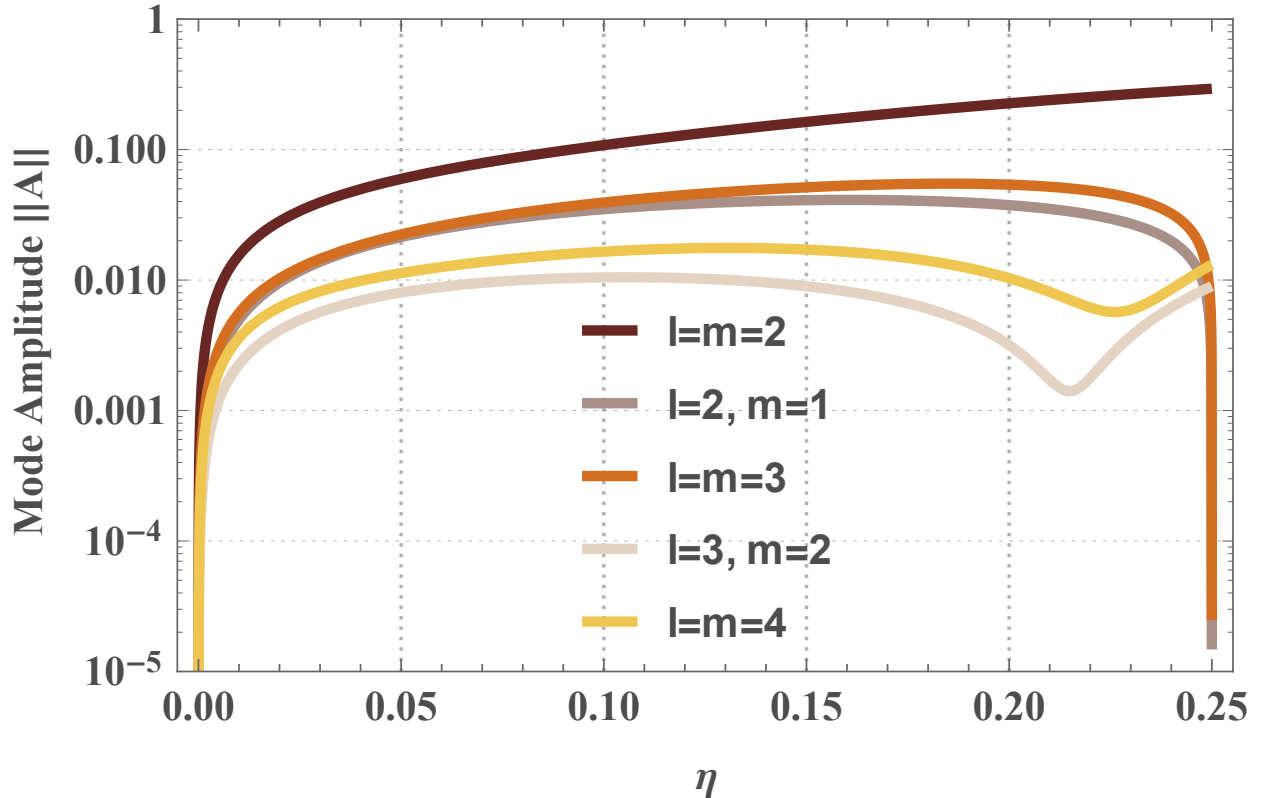


Figure 33: This figure presents the magnitude of mode amplitudes $\|A\|$ predicted by the fitting formulae given in [7] as a function of dimensionless symmetric-mass-ratio η . This figure is taken from [62]

For simplicity, we perform these injections in zero noise. Note that zero noise is a realisation of Gaussian noise and therefore any assumptions during the PE that rely on the nature of noise being Gaussian still remains valid. A more detailed work of similar nature needs to be performed in the presence of detector noise to understand how it influences the

analysis in a realistic case, but this is beyond the scope of our current study.

6.3.2 Details on Parameter Estimation

We perform a full Bayesian PE using the code package *PyCBC* to produce the posterior distribution of intrinsic parameters for all the cases considered in our study. We use the *emcee-pt* ensemble sampler to perform the parallel tempered Markov chain Monte Carlo (MCMC) operation. The technical details of this algorithm are presented in [?]. We use 38 inverse-temperatures chains to sample the parameter space. For each temperature chain, we use 200 walkers to explore the space. We use an analytical model of the advanced LIGO sensitivity curve, named Zero-detuned high power (ZDHP) noise curve, for calculating the likelihood function at each sampled point. Further, a Gaussian likelihood model is used; thereby, we assume the nature of the noise to be Gaussian.

The waveform model used to perform the PE consists of $l = m = 2$ and $l = m = 3$ QNMs as a function of $\{M_f, a_f\}$ of the final BH. Analytical expression for the waveform can be written down as,

$$\begin{aligned} h_+ &= A_{22} \left\{ e^{-\frac{t}{\tau_{22}}} \cos(2\pi f_{22} t) Y_+^{22}(\iota) \right. \\ &\quad \left. + A_R (e^{-\frac{t}{\tau_{33}}} \cos(2\pi f_{33} t) Y_+^{33}(\iota)) \right\} \\ h_\times &= A_{22} \left\{ e^{-\frac{t}{\tau_{22}}} \sin(2\pi f_{22} t) Y_\times^{22}(\iota) \right. \\ &\quad \left. + A_R (e^{-\frac{t}{\tau_{33}}} \sin(2\pi f_{33} t) Y_+^{33}(\iota)) \right\}. \end{aligned} \tag{6.3}$$

Here $\{f_{lm}, \tau_{lm}\} = \{f_{lm}(M_f, a_f), \tau_{lm}(M_f, a_f)\}$ are the QNM frequencies and damping time of $l = m \in 2, 3$ modes.

There are 6 intrinsic parameters in this RD model $\vartheta = \{M_f, a_f, A_{22}, A_R, \phi_{22}, \phi_{33}\}$. We fix the extrinsic parameters and estimate only these 6 intrinsic parameters of the injections. In a more realistic case, one can do this if the PE on the full IMR waveform provides a reasonably well-constrained inference of the extrinsic parameters.

Further, we use non-informative prior summarised in Table 11 to avoid any bias. However, in reality, when one has the parameter inference from a full IMR PE, using a more informative prior, particularly on the M_f, a_f, A_{22} might help to better infer the parameters of RD.

Parameters	Minimum	Maximum	Description
Final mass	50	100	Uniform
Final Spin	-0.99	0.99	Uniform
Amplitude of dominant mode	10^{-25}	5×10^{-20}	Uniform in Log_{10}
Amplitude Ratio	0	0.5	Uniform
Phase of dominant mode			Uniform in angles
Phase of second mode			Uniform in angles

Table 11: The list of prior used to perform two mode RD PE. In this Table, we list the choice of priors used in our study. Note that these priors are non-informative in the sense that we do not favour any particular configuration. However, the bounds of the parameter space contain some information in itself. Further, the prior on A_{22} is set to be log-uniform and not uniform to ensure a better sampling of the smaller amplitudes.

6.4 Results

	$A_R=0.1$	$A_R=0.2$	$A_R=0.3$
SNR = 15	No	No	Yes
SNR = 20	No	Yes	Yes
SNR = 25	No	Yes	Yes
SNR = 30	Yes	Yes	Yes

Table 12: Testing the presence of the second mode. From looking at the posterior plots present in Figures 34, 35, 36 and 37, we infer the cases in which we can detect the presence of the second mode.

We perform PE on 16 systems, with injection corresponding to varying ρ_{RD} and A_R and present the results in Figure 34, 35, 36 and 37. Although the PE has been performed to

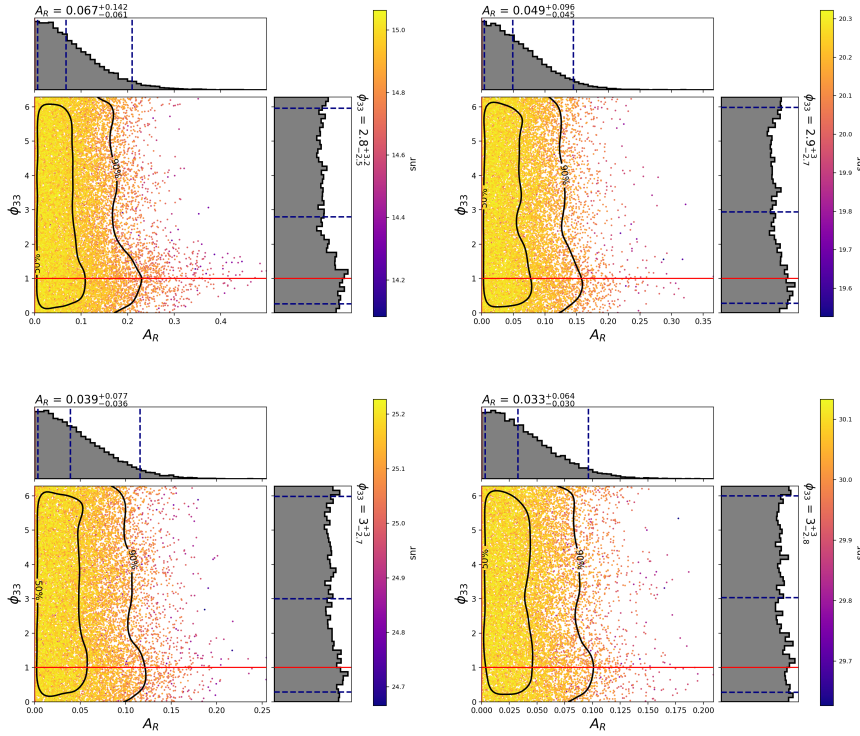


Figure 34: This is a null result test. Above are the posterior plots for the recovery of mode amplitude ratio and phase of the subdominant mode. The injected waveform has ringdown corresponding to only the dominant mode but it is recovered by a template family that has two modes of ringdown. The top panel corresponds to an injection of an optimal injected SNR = 15, the top right to SNR = 20, the bottom left to SNR = 25 and that in bottom right to SNR = 30.

infer all the intrinsic parameters of the ringdown i.e., $\{M_f, a_f, A_{22}, A_R, \phi_{22}, \phi_{33}\}$ we present only the results for the inference of $\{A_R, \phi_{22}\}$ in the figures for readability. However, for each case we confirm that the 90 % confidence interval contains the injected values for all the parameters.

The Figure 34 corresponds to ‘the null test’, where the injections contains only one mode i.e., $A_R = 0$. The Figures 35, 36 and 37 correspond to $A_R = 0.1, 0.2$ and 0.3 respectively. In all the four figures, the top left panel corresponds to $\rho_{RD} = 15$, the top right panel corresponds to $\rho_{RD} = 20$, the bottom left panel corresponds to $\rho_{RD} = 25$ and the bottom right panel corresponds to $\rho_{RD} = 30$. In each of these cases, we find that the injected value of parameters (indicated by red line in the figures) lie within 50 % (and thus, 90 %) credible interval. Further, the null test in Figure 34 is consistent with what is expected; the marginalized

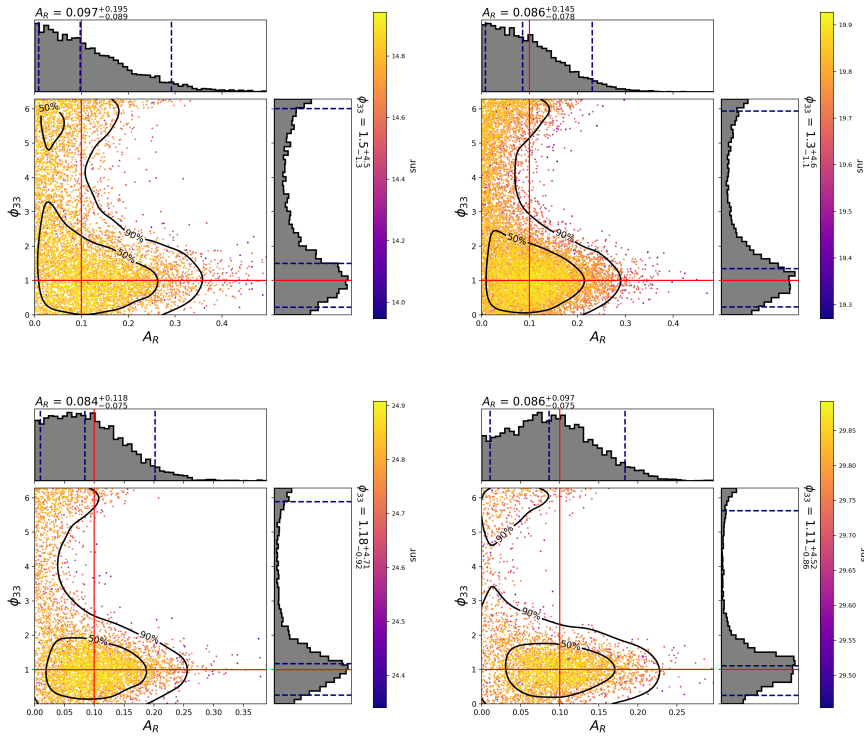


Figure 35: Above are the posterior plots for the recovery of mode amplitude ratio and phase of the subdominant mode. The mode amplitude ratio of the injection is 0.1 and the phase of the subdominant mode is 1. The top panel corresponds to an injection of an optimal injected SNR = 15, the top right to SNR = 20, the bottom left to SNR = 25 and that in bottom right to SNR = 30.

posterior for A_R rails against $A_R = 0$, thereby, indicating the absence of the second mode. Also, there is no information on the phase of $l = m = 3$ mode that can be inferred from the PE results for this case.

Among the injections we have studied, the most unlikely candidate to allow for detection of the subdominant mode is $A_R = 0.1$ and $\rho_{RD} = 15$ (panel 1 of Figure 35). Here we see that posterior distribution for A_R still rails against $A_R = 0$, thereby, not allowing us to assert the presence of the subdominant mode. Nevertheless, we notice that the posterior for A_R has more support for higher values of A_R compared to the null test case. As we increase the ρ_{RD} , the posterior distribution for A_R shifts towards $A_R = 0.1$. Since the population studies of BBH favours nearly equal mass BBH systems [?], studying the RDs for smaller A_R is crucial. We therefore perform an injection with $\rho_{RD} = 40$ for the $A_R = 0.1$ and show that we can indeed infer the presence of the subdominant mode for a higher ρ_{RD} system even with

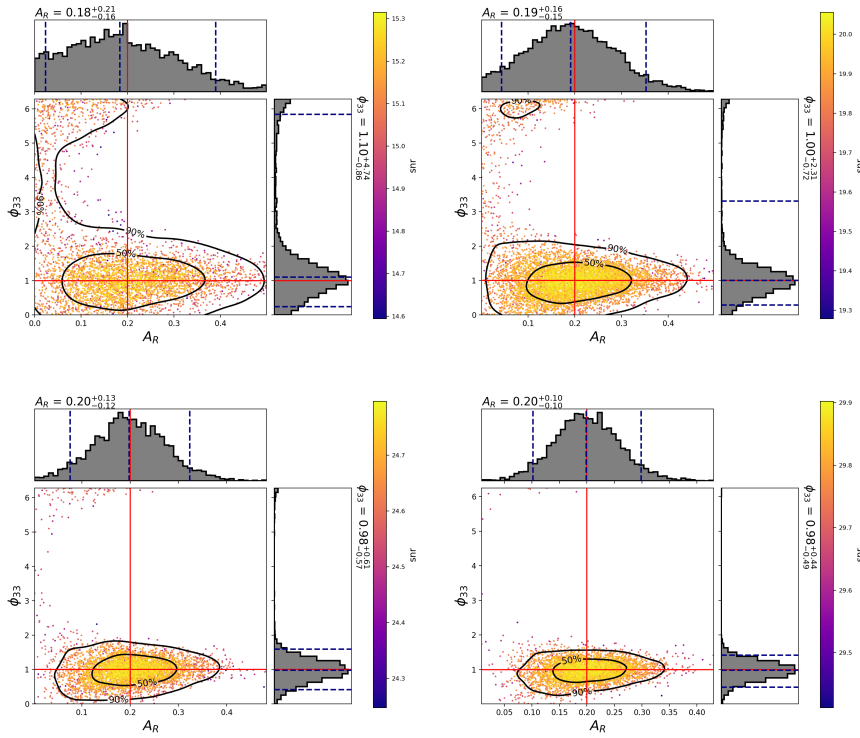


Figure 36: Above are the posterior plots for the recovery of mode amplitude ratio and phase of the subdominant mode. The mode amplitude ratio of the injection is 0.2 and the phase of the subdominant mode is 1. The top panel corresponds to an injection of an optimal injected SNR = 15, the top right to SNR = 20, the bottom left to SNR = 25 and that in bottom right to SNR = 30.

a $A_R = 0.1$. The PE result for this case is presented in Figure 38.

However, it is striking that the posterior distribution for the phase of $l = m = 3$ mode ϕ_{33} , peaks around the corrected injection value even for $A_R = 0.1$ and $\rho_{RD} = 15$ case. This provides strong hints favouring the presence of the subdominant mode even for $A_R = 0.1$ with smaller values of ρ_{RD} . In fact, in all the case we have studied, we see that the ringdown PE performs remarkably good for the recovery of the phase of the subdominant mode.

For this study, the criteria for a confident inference of the presence of the subdominant mode is that the 90 % credible interval should not have support for $A_R = 0$. With this criterion, we see that for $A_R = 0.1$ we cannot claim the detection of the subdominant mode at least up to an $\rho_{RD} = 30$. But for $A_R = 0.2$, we can infer the presence of the second mode for a signal with $\rho_{RD} \geq 20$. When A_R is increased to $A_R = 0.3$, we can infer the presence of the second mode for the injections we use in this study, including $\rho_{RD} = 15$. We tabulate

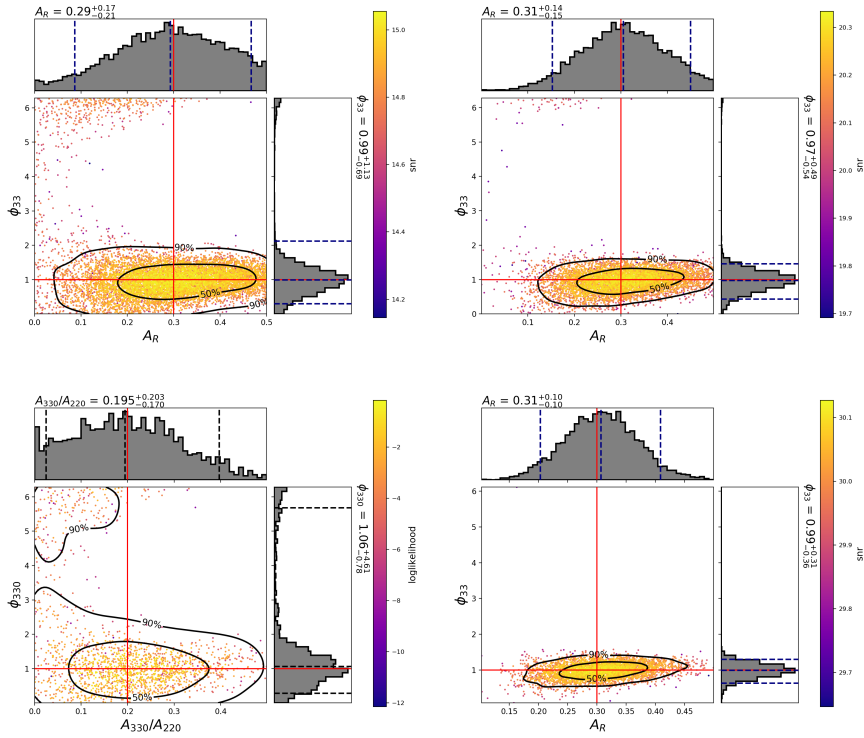


Figure 37: Above are the posterior plots for the recovery of mode amplitude ratio and phase of the subdominant mode. The mode amplitude ratio of the injection is 0.3 and the phase of the subdominant mode is 1. The top panel corresponds to an injection of SNR = 15, the top right to SNR = 20, the bottom left to SNR = 15, the bottom right to SNR = 20.

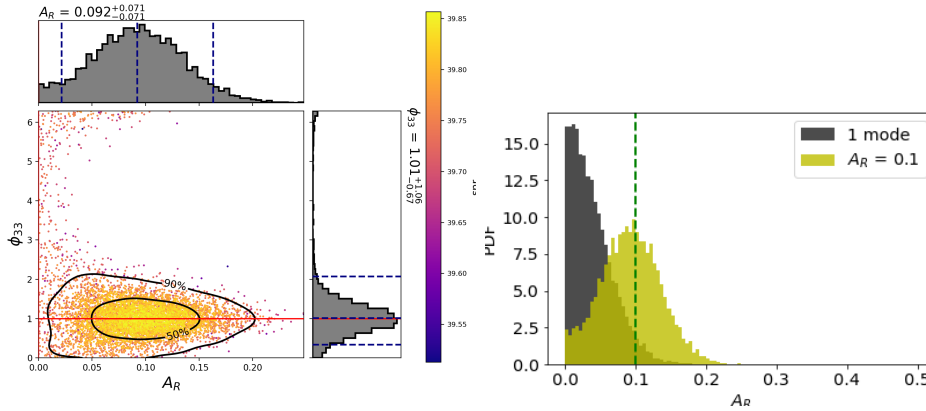


Figure 38: Mode amplitude ratio of 0.1 at an SNR of 40. In this figure, we show the result of parameter estimation when the optimal SNR of ringdown injection with amplitude ratio of 0.1 is increased to 40. Panel on the left shows the posterior recovered and can be compared with Figure 35. Panel on the right compares the normalized histogram for amplitude ratio for $A_R = 0$ (single mode) and $A_R = 0.1$ and can be compared to Figure 39. In this case we see that the second mode can be inferred.

this result in Table 12.

Next, we compare the marginalized posteriors distribution for A_R for different SNR with the null case (this will allow us to get an intuition for the false alarm probability for the inferred presence of subdominant mode). More the overlap of the posteriors distribution for $A_R \neq 0$ with that for $A_R = 0$, more is the false alarm probability in the claim of presence of the subdominant mode. This comparison is presented in Figure 39 where the panels are arranged top to bottom for $\rho_{RD} = 15, 20, 25, 30$ respectively. If the posterior distribution for A_R clearly separates from the posterior distribution for the case with $A_R = 0$, the presence of the second mode can be inferred confidently. We note that the posterior distribution corresponding to $A_R = 0.3$ (the pink histogram) always separates from $A_R = 0$ (the black histogram), even for $\rho_{RD} = 15$, whereas that which corresponds to $A_R = 0.2$ (the blue histogram) separates out after $\rho_{RD} = 20$. Although in none of the cases the posterior corresponding to $A_R = 0.1$ (the green histogram) clearly separates out from $A_R = 0$, we see that it shifts away from $A_R = 0$. In the left panel of Figure 38 however, we do see that for $\rho_{RD} = 40$, we can infer the presence of subdominant mode in case of $A_R = 0.1$ confidently.

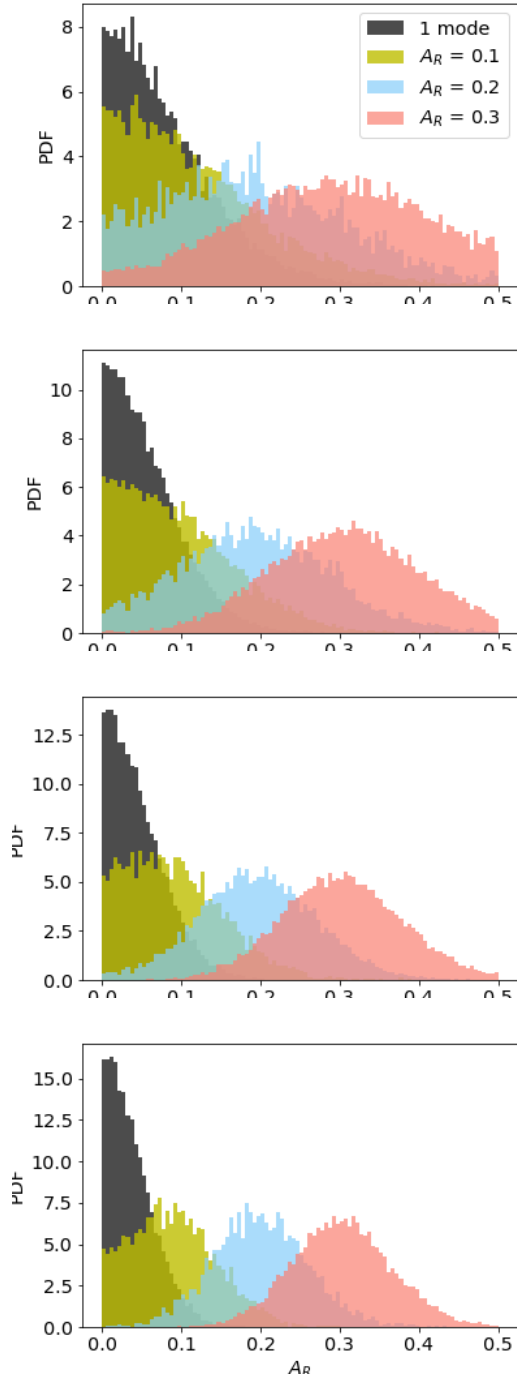


Figure 39: Marginalized posteriors for amplitude ratio for all the injection in this study. The panels corresponds to normalized histogram for amplitude ratio for ringdown injections corresponding to an optimal $\text{SNR} = \{15, 20, 25, 30\}$ from top to bottom. In each of these panels, the black histogram corresponds to the null case, where the injected signal has only one mode. The green, blue and red histogram correspondes to an injection with amplitude ratio of 0.1, 0.2 and 0.3 respectively. When the colored histograms (corresponding to a non-zero amplitude ratio) separate clearly from the black histogram (corresponding to single mode injection), one can claim the detection of the second mode.

6.5 Discussions and Implications

For a BBH RD signal, the excitation amplitude of the different modes depends on the perturbation conditions set up by the inspiral-merger phase. This, in turn, is dictated by the asymmetry of the initial binary system i.e., mass ratio and the spin of the progenitor. An equal mass system does not excite the $l = m = 3$. To get a mode amplitude ratio of 0.1, a nonspinning progenitor binary would have to have a mass ratio of ~ 1.5 and a BBH with a mass ratio of little more than $q = 2$ produces an RD with a mode amplitude ratio ~ 0.2 . Although we see that there is larger support for nearly equal mass BBH systems from the population studies, LIGO has already detected some asymmetric mass ratio system; for example, GW151012 and GW151226 have a $q \sim 1.7$ and GW170729 and GW170104 have a $q \sim 1.5$. Unfortunately, these signals did not have enough SNR in the RD to allow for inference of the subdominant mode even though the amplitude ratio of modes were favourable. However, with the coming of advanced LIGO operating at its design sensitivity, one expects the SNR to increase by nearly threefolds, thereby making the prospect of detecting the subdominant mode of RD quite promising. Furthermore, the number of events to increase giving us statistically better chances of observing asymmetrical BBH.

Higher the value of relative amplitudes between the modes, one can do spectroscopy of BBH RD with a smaller SNR. In particular, from our study we note that, while a system with $A_R = 0.1$ requires an optimal RD SNR of ~ 40 for detection of the subdominant mode, a system with $A_R = 0.3$ needs just an SNR of 15. Putting this in perspective, the GW150914 event has an RD SNR of ~ 8 . However, if the GW150914 were seen using aLIGO at its design sensitivity the RD SNR would be around ~ 24 . At the same RD SNR, had we detected a mass ratio $q = 2$ system, it would have been a particularly promising candidate to perform tests with ringdown that requires the detection of the second mode. This is to emphasise the fact that we have already seen a system that is close enough in distance to have a loud SNR in RD and that although the requirement of RD SNR seems challenging, it is not impossible to observe such events in the upcoming era of GW astronomy.

Note that for a non-spinning progenitor binary system, the $l = m = 3$ mode is always the second most dominant mode (intrinsically, without considering the effects of the inclination angle) and hence, we used it as the subdominant mode in our study. However, it should be noted that for a sufficiently spinning progenitor BBH system the $l = 2, m = 1$ mode can be stronger than the $l = m = 3$ mode for some parameter space of BBHs (c.f Figure 1 and 2 of [95]). Therefore, if the IMR parameter inferences indicate the presence of significant total spin magnitude for the progenitors, the RD PE should also include the $l = 2, m = 1$ mode

multimodal analysis.

A follow-up study to investigate the effects of the presence of the detector noise is underway and will soon be concluded. Furthermore, performing the RD analysis on a full inspiral-merger-ringdown (IMR) signal has additional complications of identifying the start time of the perturbation regime; one needs to pick a time carefully such that it optimises the systematic error arising from starting the RD too early and statistical error that arises from starting the ringdown too late in the signal. This complication has been circumvented in this study since we assume the RD to be composed of only QNMs. We are also performing a follow-up study to understand this effect. Also, a careful astrophysical population study has to be done to understand the realist probability of seeing signals that will allow for multimodal RD detection. In this study, we provide preliminary studies on what kind of signals would allow us to detect two modes in RD and set a stage for the upcoming work.

Chapter 7

Conclusion

This era of GW astronomy provides an unprecedented opportunity to probe and understand the nature of gravity, thereby, testing the regime of validity of the general theory of relativity. Understanding the regimes of validity of GR is one of the flagship challenges that will help to resolve many challenges in today's physics. In this thesis, we have primarily focused on using BBH RD to design the tests that probe the nature of strong field gravity. The three broad themes that we have discussed here are the following: When does the RD start in the post-merger GW signal from a BBH merger event? How realistic is it to expect that we would be able to perform a multimodal RD test in the near future? How should the data analysis be carried out to extract multimodal RD information using a Bayesian framework from a BBH GW signal present in the detector data?

GR is an elegant theory that has diffeomorphism as well as non-linearity at the heart of it. As a consequence, associating an event that is close to the BH horizon to an event at future null infinity is extremely hard. Diffeomorphism brings in the complication of the gauge choices, i.e., different observers will see the event happening at a different time in their reference frames. Further, the non-linearity in the theory does not allow for a strict localization of the source; GWs can source and back react on themselves especially in the strong field region. Therefore, in the framework of GR, localization of the source can only be done approximately, both spatially and temporally. In Chapter 4, we investigate this issue and present a technique to approximately connect events close to the BH to its effect at asymptotic future null infinity. The techniques presented in Chapter 4, although developed in the context of mapping the source frame perturbation amplitudes to the GW observed at asymptotic infinity, they can in principle be used to map the evolution of any quantity in the source frame to the asymptotic frame. Note that the map is based on the cause-effect

relationship. It should also be noted that our procedures rely on the construction of the outgoing null characteristics and therefore, has the limitation that these techniques fail in the region of spacetime that forms strong caustics (intersecting null-rays).

From the studies presented in Chapter 3 and 4, we understand the start time of RD as seen in the source frame close to the BH. We then connect this to the observation seen by GW detectors, to predict the start time of RD in the waveform. If an analysis of RD starts at a point where the perturbative description is not yet valid, one might run into false inferences that are inconsistent with GR. In practice, while performing an RD based test, the start time should be chosen, keeping in mind the trade-off between the systematic modelling errors and the statistical error from the detector noise. On one hand, one would like to maximize the SNR in the RD by starting the analysis as early as possible (statistical errors) but on the other hand, starting the analysis too early, when the perturbative description is not yet valid, might lead to erroneous inferences of the RD parameters (systematic errors). For the current sensitivity of the LIGO detectors, our study in Chapter 4 indicates that the statistical errors from the detector's noise dominate over the systematic effects. However, in the future, with the next-generation detectors, one would need to carefully pick the start time of RD in such a way that the errors arising from both these independent sources are minimized.

In Chapter 5 and 6, we study the prospects of a multimodal RD test with the signals that will be observed by LIGO and other proposed next-generation detectors in the near future. While Chapter 5 relies on a Fisher Matrix formalism, in Chapter 6 we provide a demonstration of carrying out a multimode detection in RD using a full Bayesian PE setup.

In Chapter 5, we present a study that shows that the prospects of multimodal RD analysis are optimistic with the upgrades to the current LIGO facilities and with any of the proposed future GW detectors. Also, we propose that if a frequency dependent sensitivity increase can be achieved in the detectors, then an improvement in the band between 300 - 500 Hz will be optimal for ringdown based analysis.

In Chapter 6, we present a soon-to-be-published study where we develop a framework to perform a multimodal RD analysis using a full Bayesian inference. The study aims at developing an intuition on what should be the minimum SNR in the RD for detection of the subdominant mode given an amplitude ratio between the dominant and the subdominant mode. This is a preliminary study that is performed in a simplified setting of QNM only injections in zero noise, with the aim of setting a stage for future followup work in more realistic scenarios with real detector noise. In this study, we infer that for an amplitude ratio of 0.1, one needs an RD SNR of ~ 40 for a multimodal detection while for an amplitude ratio

of 0.3 an RD SNR of ~ 15 is sufficient. From the preliminary results of this study, we see that there is an optimistic chance of detecting the presence of the sub-dominant mode in the RD with aLIGO running at its design sensitivity.

With the promise of the upcoming GW detectors, probing the strong field gravity using RD seems quite encouraging. Understanding the spacetime dynamics during the transition from the merger to RD might prove to be challenging and yet essential. Furthermore, excitation of higher QNM overtones and tail effects might start playing a significant role if the SNR of RD is high. In order to perform these tests of GR, we need to develop tools that would allow us to perform robust data analysis on RD as well as understand the details of the morphology of RD signals for modelling them accurately.

**

Appendix A

On KERR-NUT spacetime

A.1 Kerr-NUT parameters

In this appendix, we provide a review of the parameters of the Kerr-NUT solution. The Kerr family of vacuum solutions is unique when one imposes axisymmetry, stationarity and regularity on the BH horizon along with asymptotic flatness. However, if one allows for generalization by relaxing the asymptotic flatness condition, one arrives at a family of solutions called Kerr-NUT. This solution is a part of the broader family of Einstein-Maxwell type D solutions. This generalized family of spacetimes is parameterized by 6 parameters (potentially 7 if one includes the cosmological constant Λ). In Table A.1, we summarize the parameters, as well as their physical meaning and symbols used in various texts.

The general Einstein-Maxwell Type D solution (including cosmological constant Λ) has the form given in Eq. 21.11 of [120], with parameters m , l , γ , ε , e , and g . m refers to the mass parameter (closely related to the mass of the BH), γ is related to the angular momentum parameter a (closely related to the spin of the BH), ε is related to the acceleration b , e is the electric charge, g is the magnetic charge, and l is known as the NUT parameter. As outlined in [203], the mass and the NUT parameter form a complex quantity, as do the angular momentum and the acceleration, similarly to the electric and magnetic charges. In [203], ε and γ do not appear in the curvature quantities, and are called kinematical parameters, while the others are dynamical parameters.

As shown in Table 21.1 of [120], setting all of the parameters to zero except for m , a (and hence γ and ε), and e yields the Kerr-Newman solution, while also setting $a = 0$ yields the Reissner-Nordstrom solution. Kerr-Taub-NUT metrics, meanwhile, are parametrized by mass, spin, and l , with $l \neq 0$, and are thought to be unphysical [204]. The vacuum BBH case considered in this study, meanwhile, sets $e = 0$ and $g = 0$, since there are no electric

or magnetic charges at the start of the simulation, and no sourcing of them during the simulation.

An accelerating and rotating BH with a NUT charge will have non-zero m , l , a , and b , with $a > l$. A Kerr solution with a NUT charge will then have $b = 0$. An accelerating and rotating BH, meanwhile, will have $l = 0$. Finally, the Kerr solution has both $l = 0$ and $b = 0$. An illustration of this is provided in Fig. 1 of [205]. The condition $l = 0$ gives the Kerr 2 condition considered in this paper, given in Eq. (4.16).

After setting $l = 0$, the parameters m , ε and γ are related to the mass and spin of a BH are as follows,

$$\text{mass} = \frac{m}{\varepsilon^{\frac{3}{2}}} \quad \text{and} \quad \text{spin} = \frac{2\sqrt{|\gamma|}}{\varepsilon}. \quad (\text{A.1})$$

Since, $\varepsilon > 0$ and $m > 0$ for a Kerr BH, the condition that $b = 0$ gives $\varepsilon > 0$, which corresponds to the Kerr 3 condition given in Eq. (4.17).

	Stephani [120]	García-Parrado [106]	Plebanski [203]	Griffiths [205]
ntable[h] Cosmological constant	Λ	λ		
Mass parameter	m	μ	m	m
NUT parameter	l	λ	n	n
Angular momentum parameter	γ	γ	γ	k
Acceleration parameter	ε	ϵ	ϵ	ϵ
Electric charge	e		e	e
Magnetic charge	g		g	g

Bibliography

- [1] B. P. Abbott, R. Abbott, T. D. Abbott, M. R. Abernathy, F. Acernese, K. Ackley, C. Adams, T. Adams, P. Addesso, R. X. Adhikari, and et al. Improved Analysis of GW150914 Using a Fully Spin-Precessing Waveform Model. *Physical Review X*, 6(4):041014, October 2016.
- [2] The Virgo Collaboration The LIGO Scientific Collaboration. Binary black hole mergers in the first advanced ligo observing run. www.dcc.ligo.org/P1600088, 2016.
- [3] B. P. Abbott et al. Observation of gravitational waves from a binary black hole merger. *Phys. Rev. Lett.*, 116:061102, Feb 2016.
- [4] Robert Owen. The Final Remnant of Binary Black Hole Mergers: Multipolar Analysis. *Phys. Rev.*, D80:084012, 2009.
- [5] B. P. Abbott et al. Tests of general relativity with GW150914. *Phys. Rev. Lett.*, 116(22):221101, 2016.
- [6] M. Evans et al. Exploring the sensitivity of next generation gravitational wave detectors. www.dcc.ligo.org/P16000143, 2016.
- [7] L. London, D. Shoemaker, and J. Healy. Modeling ringdown: Beyond the fundamental quasinormal modes. *Phys. Rev. D*, 90(12):124032, December 2014.
- [8] Emanuele Berti, Vitor Cardoso, and Clifford M. Will. Gravitational-wave spectroscopy of massive black holes with the space interferometer lisa. *Phys. Rev. D*, 73:064030, Mar 2006.
- [9] D. Wallace. The quantization of gravity - an introduction. *ArXiv General Relativity and Quantum Cosmology e-prints*, April 2000.
- [10] B. Schulz. Review on the quantization of gravity. *ArXiv e-prints*, September 2014.

- [11] R. P. Woodard. How far are we from the quantum theory of gravity? *Reports on Progress in Physics*, 72(12):126002, December 2009.
- [12] S. Mukhi. String theory: a perspective over the last 25 years. *Classical and Quantum Gravity*, 28(15):153001, August 2011.
- [13] J. Polchinski. The Black Hole Information Problem. In J. Polchinski and et al., editors, *New Frontiers in Fields and Strings (TASI 2015) - Proceedings of the 2015 Theoretical Advanced Study Institute in Elementary Particle Physics. Edited by POLCHINSKI JOSEPH ET AL. Published by World Scientific Publishing Co. Pte. Ltd., 2017. ISBN #9789813149441, pp. 353-397*, pages 353–397, 2017.
- [14] W. G. Unruh and R. M. Wald. Information loss. *Reports on Progress in Physics*, 80(9):092002, September 2017.
- [15] S. D. Mathur. The information paradox: a pedagogical introduction. *Classical and Quantum Gravity*, 26(22):224001, November 2009.
- [16] R. Brout, S. Massar, R. Parentani, and P. Spindel. A primer for black hole quantum physics. , 260:329–446, September 1995.
- [17] I. Bena and N. P. Warner. Resolving the Structure of Black Holes: Philosophizing with a Hammer. *ArXiv e-prints*, November 2013.
- [18] W. de Boer. Grand unified theories and supersymmetry in particle physics and cosmology. *Progress in Particle and Nuclear Physics*, 33:201–301, 1994.
- [19] S. M. Carroll, W. H. Press, and E. L. Turner. The cosmological constant. , 30:499–542, 1992.
- [20] V. Sahni. The cosmological constant problem and quintessence. *Classical and Quantum Gravity*, 19:3435–3448, July 2002.
- [21] T. Padmanabhan. Dark Energy: Mystery of the Millennium. In J.-M. Alimi and A. Füzfa, editors, *Albert Einstein Century International Conference*, volume 861 of *American Institute of Physics Conference Series*, pages 179–196, November 2006.
- [22] A. Ashtekar, B. K. Berger, J. Isenberg, and M. A. H. MacCallum. General Relativity and Gravitation: A Centennial Perspective. *ArXiv e-prints*, September 2014.

- [23] Clifford M. Will. The confrontation between general relativity and experiment. *Living Reviews in Relativity*, 17(1):4, Jun 2014.
- [24] J. B. Hartle. Spacetime Quantum Mechanics and the Quantum Mechanics of Spacetime. *ArXiv General Relativity and Quantum Cosmology e-prints*, April 1993.
- [25] T. Padmanabhan. Combining general relativity and quantum theory: points of conflict and contact. *Classical and Quantum Gravity*, 19:3551–3566, July 2002.
- [26] R. P. Woodard. How far are we from the quantum theory of gravity? *Reports on Progress in Physics*, 72(12):126002, December 2009.
- [27] N. Yunes and X. Siemens. Gravitational-Wave Tests of General Relativity with Ground-Based Detectors and Pulsar-Timing Arrays. *Living Reviews in Relativity*, 16:9, November 2013.
- [28] S. Nojiri, S. D. Odintsov, and V. K. Oikonomou. Modified gravity theories on a nutshell: Inflation, bounce and late-time evolution. , 692:1–104, June 2017.
- [29] T. Clifton, P. G. Ferreira, A. Padilla, and C. Skordis. Modified gravity and cosmology. , 513:1–189, March 2012.
- [30] K. S. Thorne and C. M. Will. Theoretical Frameworks for Testing Relativistic Gravity. I. Foundations. *Astrophysical J.*, 163:595, February 1971.
- [31] C. M. Will. Theoretical Frameworks for Testing Relativistic Gravity. II. Parametrized Post-Newtonian Hydrodynamics, and the Nordtvedt Effect. *Astrophysical J.*, 163:611, February 1971.
- [32] C. M. Will. Theoretical Frameworks for Testing Relativistic Gravity. III. Conservation Laws, Lorentz Invariance, and Values of the PPN Parameters. *Astrophysical J.*, 169:125, October 1971.
- [33] Jeremy Sakstein. Tests of gravity with future space-based experiments. *Phys. Rev. D*, 97:064028, Mar 2018.
- [34] Kip S. Thorne. Gravitational-wave research: Current status and future prospects. *Rev. Mod. Phys.*, 52:285–297, Apr 1980.

- [35] Curt Cutler, Theocharis A. Apostolatos, Lars Bildsten, Lee Smauel Finn, Eanna E. Flanagan, Daniel Kennefick, Dragoljub M. Markovic, Amos Ori, Eric Poisson, Gerald Jay Sussman, and Kip S. Thorne. The last three minutes: Issues in gravitational-wave measurements of coalescing compact binaries. *Phys. Rev. Lett.*, 70:2984–2987, May 1993.
- [36] B F Schutz. Gravitational wave sources and their detectability. *Classical and Quantum Gravity*, 6(12):1761, 1989.
- [37] B. P. Abbott et al. Binary Black Hole Mergers in the first Advanced LIGO Observing Run. *Phys. Rev.*, X6(4):041015, 2016.
- [38] B. P. Abbott, R. Abbott, T. D. Abbott, F. Acernese, K. Ackley, C. Adams, T. Adams, P. Addesso, R. X. Adhikari, V. B. Adya, and et al. GW170608: Observation of a 19 Solar-mass Binary Black Hole Coalescence. *Astrophysical J.*, 851:L35, December 2017.
- [39] B. P. Abbott, R. Abbott, T. D. Abbott, F. Acernese, K. Ackley, C. Adams, T. Adams, P. Addesso, R. X. Adhikari, V. B. Adya, and et al. GW170814: A Three-Detector Observation of Gravitational Waves from a Binary Black Hole Coalescence. *Physical Review Letters*, 119(14):141101, October 2017.
- [40] B. P. Abbott, R. Abbott, T. D. Abbott, F. Acernese, K. Ackley, C. Adams, T. Adams, P. Addesso, R. X. Adhikari, V. B. Adya, and et al. GW170104: Observation of a 50-Solar-Mass Binary Black Hole Coalescence at Redshift 0.2. *Physical Review Letters*, 118(22):221101, June 2017.
- [41] B. P. Abbott, R. Abbott, T. D. Abbott, F. Acernese, K. Ackley, C. Adams, T. Adams, P. Addesso, R. X. Adhikari, V. B. Adya, and et al. GW170817: Observation of Gravitational Waves from a Binary Neutron Star Inspiral. *Physical Review Letters*, 119(16):161101, October 2017.
- [42] Nicolas Yunes, Kent Yagi, and Frans Pretorius. Theoretical Physics Implications of the Binary Black-Hole Mergers GW150914 and GW151226. *Phys. Rev.*, D94(8):084002, 2016.
- [43] N. Yunes, K. Yagi, and F. Pretorius. Theoretical Physics Implications of the Binary Black-Hole Merger GW150914. *ArXiv e-prints*, March 2016.

- [44] J. Miller, L. Barsotti, S. Vitale, P. Fritschel, M. Evans, and D. Sigg. Prospects for doubling the range of Advanced LIGO. *Phys. Rev. D*, 91(6):062005, March 2015.
- [45] S Hild, M Abernathy, F Acernese, P Amaro-Seoane, N Andersson, K Arun, F Barone, B Barr, M Barsuglia, M Beker, N Beveridge, S Birindelli, S Bose, L Bosi, S Braccini, C Bradaschia, T Bulik, E Calloni, G Cella, E Chassande Mottin, S Chelkowski, A Chincarini, J Clark, E Coccia, C Colacino, J Colas, A Cumming, L Cunningham, E Cuoco, S Danilishin, K Danzmann, R De Salvo, T Dent, R De Rosa, L Di Fiore, A Di Virgilio, M Doets, V Fafone, P Falferi, R Flaminio, J Franc, F Frasconi, A Freise, D Friedrich, P Fulda, J Gair, G Gemme, E Genin, A Gennai, A Giazotto, K Glampedakis, C Grf, M Granata, H Grote, G Guidi, A Gurkovsky, G Hammond, M Hannam, J Harms, D Heinert, M Hendry, I Heng, E Hennes, J Hough, S Husa, S Huttner, G Jones, F Khalili, K Kokeyama, K Kokkotas, B Krishnan, T G F Li, M Lorenzini, H Lck, E Majorana, I Mandel, V Mandic, M Mantovani, I Martin, C Michel, Y Minenkov, N Morgado, S Mosca, B Mours, H MllerEbhardt, P Murray, R Nawrodt, J Nelson, R Oshaughnessy, C D Ott, C Palomba, A Paoli, G Parguez, A Pasqualetti, R Passaquieti, D Passuello, L Pinard, W Plastino, R Poggiani, P Popolizio, M Prato, M Punturo, P Puppò, D Rabeling, P Rapagnani, J Read, T Regimbau, H Rehbein, S Reid, F Ricci, F Richard, A Rocchi, S Rowan, A Rdiger, L Santamara, B Sassolas, B Sathyaprakash, R Schnabel, C Schwarz, P Seidel, A Sintes, K Somiya, F Speirits, K Strain, S Strigin, P Sutton, S Tarabrin, A Thring, J van den Brand, M van Veggel, C van den Broeck, A Vecchio, J Veitch, F Vetrano, A Vicere, S Vyatchanin, B Willke, G Woan, and K Yamamoto. Sensitivity studies for third-generation gravitational wave observatories. *Classical and Quantum Gravity*, 28(9):094013, 2011.
- [46] P. Amaro-Seoane, S. Aoudia, S. Babak, P. Binétruy, E. Berti, A. Bohé, C. Caprini, M. Colpi, N. J. Cornish, K. Danzmann, J.-F. Dufaux, J. Gair, O. Jennrich, P. Jetzer, A. Klein, R. N. Lang, A. Lobo, T. Littenberg, S. T. McWilliams, G. Nelemans, A. Petiteau, E. K. Porter, B. F. Schutz, A. Sesana, R. Stebbins, T. Sumner, M. Vallisneri, S. Vitale, M. Volonteri, and H. Ward. Low-frequency gravitational-wave science with eLISA/NGO. *Classical and Quantum Gravity*, 29(12):124016, June 2012.
- [47] J. Creighton and W. Anderson. *Gravitational-Wave Physics and Astronomy: An Introduction to Theory, Experiment and Data Analysis*. November 2011.
- [48] C. M. Will. *Theory and Experiment in Gravitational Physics*. March 1993.

- [49] Pawel O. Mazur. Black hole uniqueness theorems. 2000.
- [50] C.W. Misner, K.S. Thorne, and J.A. Wheeler. *Gravitation*. Number pt. 3 in Gravitation. W. H. Freeman, 1973.
- [51] O. Dreyer, B. Kelly, B. Krishnan, L. S. Finn, D. Garrison, and R. Lopez-Aleman. Black-hole spectroscopy: testing general relativity through gravitational-wave observations. *Classical and Quantum Gravity*, 21:787–803, February 2004.
- [52] S. Gossan, J. Veitch, and B. S. Sathyaprakash. Bayesian model selection for testing the no-hair theorem with black hole ringdowns. *Phys. Rev. D*, 85(12):124056, June 2012.
- [53] I. Kamaretsos, M. Hannam, S. Husa, and B. S. Sathyaprakash. Black-hole hair loss: Learning about binary progenitors from ringdown signals. *Phys. Rev. D*, 85(2):024018, January 2012.
- [54] Norman Gürlebeck. No-hair theorem for black holes in astrophysical environments. *Phys. Rev. Lett.*, 114:151102, Apr 2015.
- [55] M. Heusler. No-hair theorems and black holes with hair. *Helvetica Physica Acta*, 69:501–528, November 1996.
- [56] S. W. Hawking. Gravitational radiation from colliding black holes. *Phys. Rev. Lett.*, 26:1344–1346, May 1971.
- [57] S. W. Hawking. Black holes in general relativity. *Communications in Mathematical Physics*, 25(2):152–166, Jun 1972.
- [58] Kostas D. Kokkotas and Bernd G. Schmidt. Quasi-normal modes of stars and black holes. *Living Reviews in Relativity*, 2(2), 1999.
- [59] V. Cardoso, E. Franzin, and P. Pani. Is the Gravitational-Wave Ringdown a Probe of the Event Horizon? *Physical Review Letters*, 116(17):171101, April 2016.
- [60] H. Nakano, N. Sago, H. Tagoshi, and T. Tanaka. Black hole ringdown echoes and howls. *Progress of Theoretical and Experimental Physics*, 2017(7):071E01, July 2017.
- [61] S. Bhagwat, M. Okounkova, S. W. Ballmer, D. A. Brown, M. Giesler, M. A. Scheel, and S. A. Teukolsky. On choosing the start time of binary black hole ringdown. *ArXiv e-prints*, November 2017.

- [62] S. Bhagwat, D. A. Brown, and S. W. Ballmer. Spectroscopic analysis of stellar mass black-hole mergers in our local universe with ground-based gravitational wave detectors. *Phys. Rev. D*, 94(8):084024, October 2016.
- [63] Tito Dal Canton et al. Implementing a search for aligned-spin neutron star-black hole systems with advanced ground based gravitational wave detectors. *Phys. Rev.*, D90(8):082004, 2014.
- [64] Samantha A. Usman et al. The PyCBC search for gravitational waves from compact binary coalescence. *Class. Quant. Grav.*, 33(21):215004, 2016.
- [65] Alexander H. Nitz, Thomas Dent, Tito Dal Canton, Stephen Fairhurst, and Duncan A. Brown. Detecting binary compact-object mergers with gravitational waves: Understanding and Improving the sensitivity of the PyCBC search. *Astrophys. J.*, 849(2):118, 2017.
- [66] S. Klimenko, G. Vedovato, M. Drago, F. Salemi, V. Tiwari, G. A. Prodi, C. Lazzaro, K. Ackley, S. Tiwari, C. F. Da Silva, and G. Mitselmakher. Method for detection and reconstruction of gravitational wave transients with networks of advanced detectors. *Phys. Rev. D*, 93:042004, Feb 2016.
- [67] Kipp Cannon, Romain Cariou, Adrian Chapman, Mireia Crispin-Ortuzar, Nickolas Fotopoulos, Melissa Frei, Chad Hanna, Erin Kara, Drew Keppel, Laura Liao, Stephen Privitera, Antony Searle, Leo Singer, and Alan Weinstein. Toward early-warning detection of gravitational waves from compact binary coalescence. *The Astrophysical Journal*, 748(2):136, 2012.
- [68] Stephen Privitera, Satyanarayan R. P. Mohapatra, Parameswaran Ajith, Kipp Cannon, Nickolas Fotopoulos, Melissa A. Frei, Chad Hanna, Alan J. Weinstein, and John T. Whelan. Improving the sensitivity of a search for coalescing binary black holes with nonprecessing spins in gravitational wave data. *Phys. Rev. D*, 89:024003, Jan 2014.
- [69] B. F. Schutz. Gravitational wave astronomy. *Classical and Quantum Gravity*, 16:A131–A156, December 1999.
- [70] J. Centrella, J. G. Baker, B. J. Kelly, and J. R. van Meter. Black-hole binaries, gravitational waves, and numerical relativity. *Reviews of Modern Physics*, 82:3069–3119, October 2010.

- [71] S. Babak, R. Biswas, P. R. Brady, D. A. Brown, K. Cannon, C. D. Capano, J. H. Clayton, T. Cokelaer, J. D. E. Creighton, T. Dent, A. Dietz, S. Fairhurst, N. Fotopoulos, G. González, C. Hanna, I. W. Harry, G. Jones, D. Keppel, D. J. A. McKechnan, L. Pekowsky, S. Privitera, C. Robinson, A. C. Rodriguez, B. S. Sathyaprakash, A. S. Sengupta, M. Vallisneri, R. Vaulin, and A. J. Weinstein. Searching for gravitational waves from binary coalescence. *Phys. Rev. D*, 87:024033, Jan 2013.
- [72] J. Abadie, B. P. Abbott, R. Abbott, T. D. Abbott, M. Abernathy, T. Accadia, F. Acernese, C. Adams, R. Adhikari, C. Affeldt, and et al. Search for gravitational waves from low mass compact binary coalescence in LIGO’s sixth science run and Virgo’s science runs 2 and 3. *Phys. Rev. D*, 85(8):082002, April 2012.
- [73] B. Allen, W. G. Anderson, P. R. Brady, D. A. Brown, and J. D. E. Creighton. FINDCHIRP: An algorithm for detection of gravitational waves from inspiraling compact binaries. *Phys. Rev. D*, 85(12):122006, June 2012.
- [74] B. P. Abbott, R. Abbott, T. D. Abbott, M. R. Abernathy, F. Acernese, K. Ackley, C. Adams, T. Adams, P. Addesso, R. X. Adhikari, and et al. GW150914: First results from the search for binary black hole coalescence with Advanced LIGO. *Phys. Rev. D*, 93(12):122003, June 2016.
- [75] S Klimenko, I Yakushin, A Mercer, and G Mitselmakher. A coherent method for detection of gravitational wave bursts. *Classical and Quantum Gravity*, 25(11):114029, 2008.
- [76] B. P. Abbott, R. Abbott, T. D. Abbott, M. R. Abernathy, F. Acernese, K. Ackley, M. Adamo, C. Adams, T. Adams, P. Addesso, and et al. Characterization of transient noise in Advanced LIGO relevant to gravitational wave signal GW150914. *Classical and Quantum Gravity*, 33(13):134001, July 2016.
- [77] B. P. Abbott, R. Abbott, T. D. Abbott, M. R. Abernathy, F. Acernese, K. Ackley, C. Adams, T. Adams, P. Addesso, R. X. Adhikari, and et al. Effects of data quality vetoes on a search for compact binary coalescences in Advanced LIGOs first observing run. *Classical and Quantum Gravity*, 35(6):065010, March 2018.
- [78] B. P. Abbott et al. Search for gravitational waves from low mass compact binary coalescence in ligo’s sixth science run and virgo’s science runs 2 and 3. *Phys. Rev. D*, 85:082002, Apr 2012.

- [79] B. P. Abbott, R. Abbott, T. D. Abbott, M. R. Abernathy, F. Acernese, K. Ackley, C. Adams, T. Adams, P. Addesso, R. X. Adhikari, and et al. Properties of the Binary Black Hole Merger GW150914. *Physical Review Letters*, 116(24):241102, June 2016.
- [80] Andrea Taracchini, Alessandra Buonanno, Yi Pan, Tanja Hinderer, Michael Boyle, Daniel A. Hemberger, Lawrence E. Kidder, Geoffrey Lovelace, Abdul H. Mroué, Harald P. Pfeiffer, Mark A. Scheel, Béla Szilágyi, Nicholas W. Taylor, and Anil Zenginoglu. Effective-one-body model for black-hole binaries with generic mass ratios and spins. *Phys. Rev. D*, 89:061502, Mar 2014.
- [81] Mark Hannam, Patricia Schmidt, Alejandro Bohé, Leïla Haegel, Sascha Husa, Frank Ohme, Geraint Pratten, and Michael Pürrer. Simple model of complete precessing black-hole-binary gravitational waveforms. *Phys. Rev. Lett.*, 113:151101, Oct 2014.
- [82] Y. Pan, A. Buonanno, A. Taracchini, L. E. Kidder, A. H. Mroué, H. P. Pfeiffer, M. A. Scheel, and B. Szilágyi. Inspiral-merger-ringdown waveforms of spinning, precessing black-hole binaries in the effective-one-body formalism. *Phys. Rev. D*, 89(8):084006, April 2014.
- [83] Saul A. Teukolsky. The Kerr Metric. *Class. Quant. Grav.*, 32(12):124006, 2015.
- [84] T. Damour, A. Nagar, and L. Villain. Merger states and final states of black hole coalescences: Comparing effective-one-body and numerical-relativity. *Phys. Rev. D*, 89(2):024031, January 2014.
- [85] S. A. Teukolsky. Perturbations of a Rotating Black Hole. I. Fundamental Equations for Gravitational, Electromagnetic, and Neutrino-Field Perturbations. *Astrophysical J.*, 185:635–648, October 1973.
- [86] W. H. Press and S. A. Teukolsky. Perturbations of a Rotating Black Hole. II. Dynamical Stability of the Kerr Metric. *Astrophysical J.*, 185:649–674, October 1973.
- [87] S. A. Teukolsky and W. H. Press. Perturbations of a rotating black hole. III - Interaction of the hole with gravitational and electromagnetic radiation. *Astrophysical J.*, 193:443–461, October 1974.
- [88] S. Detweiler S. Chandrasekhar. The quasi-normal modes of the schwarzschild black hole. *Proceedings of the Royal Society of London. Series A, Mathematical and Physical Sciences*, 344(1639):441–452, 1975.

- [89] E. W. Leaver. An analytic representation for the quasi-normal modes of Kerr black holes. *Proceedings of the Royal Society of London Series A*, 402:285–298, December 1985.
- [90] Frank J. Zerilli. Gravitational field of a particle falling in a schwarzschild geometry analyzed in tensor harmonics. *Phys. Rev. D*, 2:2141–2160, Nov 1970.
- [91] S. Chandrasekhar. On the equations governing the perturbations of the schwarzschild black hole. *Proceedings of the Royal Society of London. Series A, Mathematical and Physical Sciences*, 343(1634):289–298, 1975.
- [92] E. Berti, V. Cardoso, J. A. Gonzalez, U. Sperhake, M. Hannam, S. Husa, and B. Brügmann. Inspiral, merger, and ringdown of unequal mass black hole binaries: A multipolar analysis. *Phys. Rev. D*, 76(6):064034, September 2007.
- [93] Vishal Baibhav, Emanuele Berti, Vitor Cardoso, and Gaurav Khanna. Black Hole Spectroscopy: Systematic Errors and Ringdown Energy Estimates. 2017.
- [94] L. London, D. Shoemaker, and J. Healy. Modeling ringdown: Beyond the fundamental quasinormal modes. *Phys. Rev. D*, 90(12):124032, December 2014.
- [95] I. Kamaretsos, M. Hannam, and B. S. Sathyaprakash. Is Black-Hole Ringdown a Memory of Its Progenitor? *Physical Review Letters*, 109(14):141102, October 2012.
- [96] Y. Pan, A. Buonanno, M. Boyle, L. T. Buchman, L. E. Kidder, H. P. Pfeiffer, and M. A. Scheel. Inspiral-merger-ringdown multipolar waveforms of nonspinning black-hole binaries using the effective-one-body formalism. *Phys. Rev. D*, 84(12):124052, December 2011.
- [97] B. P. Abbott et al. Observation of Gravitational Waves from a Binary Black Hole Merger. *Phys. Rev. Lett.*, 116(6):061102, 2016.
- [98] B. P. Abbott et al. GW151226: Observation of Gravitational Waves from a 22-Solar-Mass Binary Black Hole Coalescence. *Phys. Rev. Lett.*, 116(24):241103, 2016.
- [99] Benjamin P. Abbott et al. GW170104: Observation of a 50-Solar-Mass Binary Black Hole Coalescence at Redshift 0.2. *Phys. Rev. Lett.*, 118(22):221101, 2017.
- [100] B. P. Abbott et al. Gw170814: A three-detector observation of gravitational waves from a binary black hole coalescence. *Phys. Rev. Lett.*, 119:141101, Oct 2017.

- [101] Emanuele Berti et al. Testing General Relativity with Present and Future Astrophysical Observations. *Class. Quant. Grav.*, 32:243001, 2015.
- [102] Marc Mars. A Space-time characterization of the Kerr metric. *Class. Quant. Grav.*, 16:2507–2523, 1999.
- [103] Hans-Peter Nollert. About the significance of quasinormal modes of black holes. *Phys. Rev. D*, 53:4397–4402, Apr 1996.
- [104] D. W. Tufts and R. Kumaresan. Estimation of frequencies of multiple sinusoids: Making linear prediction perform like maximum likelihood. *Proceedings of the IEEE*, 70(9):975–989, Sept 1982.
- [105] E. Thrane, P. Lasky, and Y. Levin. Challenges testing the no-hair theorem with gravitational waves. *ArXiv e-prints*, June 2017.
- [106] Alfonso Garca-Parrado Gómez-Lobo. Vacuum type D initial data. *Class. Quant. Grav.*, 33(17):175005, 2016.
- [107] Mark A. Scheel, Michael Boyle, Tony Chu, Lawrence E. Kidder, Keith D. Matthews, and Harald P. Pfeiffer. High-accuracy waveforms for binary black hole inspiral, merger, and ringdown. *Phys. Rev.*, D79:024003, 2009.
- [108] J. Baker and M. Campanelli. Making use of geometrical invariants in black hole collisions. *Phys. Rev. D*, 62(12):127501, December 2000.
- [109] Manuela Campanelli, Carlos O. Lousto, and Yosef Zlochower. Algebraic Classification of Numerical Spacetimes and Black-Hole-Binary Remnants. *Phys. Rev.*, D79:084012, 2009.
- [110] Robert Owen. Degeneracy measures for the algebraic classification of numerical spacetimes. *Phys. Rev.*, D81:124042, 2010.
- [111] Casey J. Handmer and B. Szilágyi. Spectral Characteristic Evolution: A New Algorithm for Gravitational Wave Propagation. *Class. Quant. Grav.*, 32(2):025008, 2015.
- [112] Casey J. Handmer, Bla Szilágyi, and Jeffrey Winicour. Gauge Invariant Spectral Cauchy Characteristic Extraction. *Class. Quant. Grav.*, 32(23):235018, 2015.

- [113] C. J. Handmer, B. Szilágyi, and J. Winicour. Spectral Cauchy characteristic extraction of strain, news and gravitational radiation flux. *Classical and Quantum Gravity*, 33(22):225007, November 2016.
- [114] R. H. Price, S. Nampalliwar, and G. Khanna. Black hole binary inspiral: Analysis of the plunge. *Phys. Rev. D*, 93(4):044060, February 2016.
- [115] V. Cardoso, E. Franzin, and P. Pani. Is the Gravitational-Wave Ringdown a Probe of the Event Horizon? *Physical Review Letters*, 116(17):171101, April 2016.
- [116] Thomas W. Baumgarte and Stuart L. Shapiro. *Numerical Relativity: Solving Einstein's Equations on the Computer*. Cambridge University Press, New York, 2010.
- [117] Thomas Backdahl and Juan A. Valiente Kroon. A geometric invariant measuring the deviation from Kerr data. *Phys. Rev. Lett.*, 104:231102, 2010.
- [118] Thomas Backdahl and Juan A. Valiente Kroon. On the construction of a geometric invariant measuring the deviation from Kerr data. *Annales Henri Poincaré*, 11:1225–1271, 2010.
- [119] Thomas Backdahl and Juan A. Valiente Kroon. Constructing 'non-Kerrness' on compact domains. *J. Math. Phys.*, 53:042503, 2012.
- [120] H. Stephani, D. Kramer, M. MacCallum, C. Hoenselaers, and E. Herlt. *Exact Solutions of Einstein's Field Equations*. Cambridge Monographs on Mathematical Physics. Cambridge University Press, 2009.
- [121] Joan Josep Ferrando, Juan Antonio Morales, and Juan Antonio Sez. Covariant determination of the weyl tensor geometry. *Classical and Quantum Gravity*, 18(22):4939, 2001.
- [122] Alfonso Garca-Parrado Gómez-Lobo. Private communication.
- [123] G. Khanna and R. H. Price. Black hole ringing, quasinormal modes, and light rings. *Phys. Rev. D*, 95(8):081501, April 2017.
- [124] John Baker, Manuela Campanelli, and Carlos O. Lousto. The lazarus project: A pragmatic approach to binary black hole evolutions. *Phys. Rev. D*, 65:044001, Jan 2002.

- [125] Manuela Campanelli, Carlos O. Lousto, John Baker, Gaurav Khanna, and Jorge Pullin. Imposition of cauchy data to the teukolsky equation. iii. the rotating case. *Phys. Rev. D*, 58:084019, Sep 1998.
- [126] N. Bishop, R. Gomez, L. Lehner, and J. Winicour. Cauchy-characteristic extraction in numerical relativity. *ArXiv General Relativity and Quantum Cosmology e-prints*, May 1997.
- [127] H. Bondi, M. G. J. van der Burg, and A. W. K. Metzner. Gravitational waves in general relativity. vii. waves from axi-symmetric isolated systems. *Proceedings of the Royal Society of London. Series A, Mathematical and Physical Sciences*, 269(1336):21–52, 1962.
- [128] Bernardo Araneda and Gustavo Dotti. Petrov type of linearly perturbed type D spacetimes. *Class. Quant. Grav.*, 32(19):195013, 2015.
- [129] Huan Yang, Aaron Zimmerman, and Luis Lehner. Turbulent Black Holes. *Phys. Rev. Lett.*, 114:081101, 2015.
- [130] Carlos O. Lousto and Bernard F. Whiting. Reconstruction of black hole metric perturbations from Weyl curvature. *Phys. Rev.*, D66:024026, 2002.
- [131] Amos Ori. Reconstruction of inhomogeneous metric perturbations and electromagnetic four potential in Kerr space-time. *Phys. Rev.*, D67:124010, 2003.
- [132] William E. East, Fethi M. Ramazanolu, and Frans Pretorius. Black Hole Superradiance in Dynamical Spacetime. *Phys. Rev.*, D89(6):061503, 2014.
- [133] A. D. Ionescu and S. Klainerman. On the global stability of the wave-map equation in Kerr spaces with small angular momentum. 2014.
- [134] B. P. Abbott et al. Observation of gravitational waves from a binary black hole merger. *Phys. Rev. Lett.*, 116:061102, Feb 2016.
- [135] <http://www.black-holes.org/waveforms>.
- [136] Béla Szilágyi, Lee Lindblom, and Mark A. Scheel. Simulations of binary black hole mergers using spectral methods. 80:124010, 2009.
- [137] Lee Lindblom and Béla Szilágyi. An improved gauge driver for the GH Einstein system. 80:084019, 2009.

- [138] Daniel A. Hemberger, Mark A. Scheel, Lawrence E. Kidder, Béla Szilágyi, Geoffrey Lovelace, Nicholas W. Taylor, and Saul A. Teukolsky. Dynamical excision boundaries in spectral evolutions of binary black hole spacetimes. *30(11):115001*, 2013.
- [139] M. A. Scheel, M. Giesler, G. Hemberger, D. A. and Lovelace, K. Kuper, M. Boyle, and L. E. Szilágyi, B. and Kidder. Improved methods for simulating nearly extremal binary black holes. *32(10):105009*, May 2015.
- [140] Oliver Rinne, Lee Lindblom, and Mark A. Scheel. Testing outer boundary treatments for the Einstein equations. *24:4053–4078*, 2007.
- [141] Geoffrey Lovelace et al. Modeling the source of GW150914 with targeted numerical-relativity simulations. *Class. Quant. Grav.*, *33(24):244002*, 2016.
- [142] William H. Press, Saul A. Teukolsky, William T. Vetterling, and Brian P. Flannery. *Numerical Recipes 3rd Edition: The Art of Scientific Computing*. Cambridge University Press, New York, NY, USA, 3 edition, 2007.
- [143] Lee Lindblom, Mark A. Scheel, Lawrence E. Kidder, Robert Owen, and Oliver Rinne. A New generalized harmonic evolution system. *Class. Quant. Grav.*, *23:S447–S462*, 2006.
- [144] Kevin Barkett and Mark Scheel. 2017. Forthcoming.
- [145] Theocharis A. Apostolatos. Search templates for gravitational waves from precessing, inspiraling binaries. *Phys. Rev. D*, *52:605–620*, Jul 1995.
- [146] Oliver Rinne, Luisa T Buchman, Mark A Scheel, and Harald P Pfeiffer. Implementation of higher-order absorbing boundary conditions for the einstein equations. *Classical and Quantum Gravity*, *26(7):075009*, 2009.
- [147] Tullio Regge and John A. Wheeler. Stability of a schwarzschild singularity. *Phys. Rev.*, *108:1063–1069*, Nov 1957.
- [148] Frank J. Zerilli. Effective potential for even-parity regge-wheeler gravitational perturbation equations. *Phys. Rev. Lett.*, *24:737–738*, Mar 1970.
- [149] V. Moncrief. Gravitational perturbations of spherically symmetric systems. I. The exterior problem. *Annals Phys.*, *88:323–342*, 1974.

- [150] Michael Boyle and Abdul H. Mroue. Extrapolating gravitational-wave data from numerical simulations. *Phys. Rev.*, D80:124045, 2009.
- [151] Nicholas W. Taylor, Michael Boyle, Christian Reisswig, Mark A. Scheel, Tony Chu, Lawrence E. Kidder, and Bla Szilágyi. Comparing Gravitational Waveform Extrapolation to Cauchy-Characteristic Extraction in Binary Black Hole Simulations. *Phys. Rev.*, D88(12):124010, 2013.
- [152] Michael Pürrer. Frequency domain reduced order model of aligned-spin effective-one-body waveforms with generic mass-ratios and spins. *Phys. Rev.*, D93(6):064041, 2016.
- [153] J. Aasi et al. Advanced LIGO. *Class. Quant. Grav.*, 32:074001, 2015.
- [154] Milton Ruiz, Ryoji Takahashi, Miguel Alcubierre, and Dario Nunez. Multipole expansions for energy and momenta carried by gravitational waves. *Gen. Rel. Grav.*, 40:2467, 2008.
- [155] Emanuele Berti, Jaime Cardoso, Vitor Cardoso, and Marco Cavaglia. Matched-filtering and parameter estimation of ringdown waveforms. *Phys. Rev.*, D76:104044, 2007.
- [156] Kazuki Sakai, Ken-ichi Oohara, Hiroyuki Nakano, Masato Kaneyama, and Hirotaka Takahashi. Estimation of starting times of quasinormal modes in ringdown gravitational waves with the hilbert-huang transform. *Phys. Rev. D*, 96:044047, Aug 2017.
- [157] Andy Bohn, Lawrence E. Kidder, and Saul A. Teukolsky. Parallel adaptive event horizon finder for numerical relativity. *Phys. Rev.*, D94(6):064008, 2016.
- [158] Andy Bohn, William Throwe, Fran Hébert, Katherine Henriksson, Darius Bunandar, Mark A. Scheel, and Nicholas W. Taylor. What does a binary black hole merger look like? *Class. Quant. Grav.*, 32(6):065002, 2015.
- [159] B. P. Abbott et al. Gw151226: Observation of gravitational waves from a 22-solar-mass binary black hole coalescence. *Phys. Rev. Lett.*, 116:241103, Jun 2016.
- [160] N. Yunes and X. Siemens. Gravitational-Wave Tests of General Relativity with Ground-Based Detectors and Pulsar-Timing Arrays. *Living Reviews in Relativity*, 16, November 2013.

- [161] B. P. Abbott, R. Abbott, T. D. Abbott, M. R. Abernathy, F. Acernese, K. Ackley, C. Adams, T. Adams, P. Addesso, R. X. Adhikari, and et al. Tests of General Relativity with GW150914. *Physical Review Letters*, 116(22):221101, June 2016.
- [162] C.W. Misner, K.S. Thorne, and J.A. Wheeler. *Gravitation*. W.H. Freeman and Company, 1973.
- [163] Jacob D. Bekenstein. Nonexistence of baryon number for static black holes. *Phys. Rev. D*, 5:1239–1246, Mar 1972.
- [164] Jacob D. Bekenstein. Novel “no-scalar-hair” theorem for black holes. *Phys. Rev. D*, 51:R6608–R6611, Jun 1995.
- [165] B. Carter. Axisymmetric black hole has only two degrees of freedom. *Phys. Rev. Lett.*, 26:331–333, Feb 1971.
- [166] Kent Yagi and Leo C Stein. Black hole based tests of general relativity. *Classical and Quantum Gravity*, 33(5):054001, 2016.
- [167] Thomas P Sotiriou. Black holes and scalar fields. *Classical and Quantum Gravity*, 32(21):214002, 2015.
- [168] Olaf Dreyer, Bernard Kelly, Badri Krishnan, Lee Samuel Finn, David Garrison, and Ramon Lopez-Aleman. Black-hole spectroscopy: testing general relativity through gravitational-wave observations. *Classical and Quantum Gravity*, 21(4):787, 2004.
- [169] Richard H. Price and Jorge Pullin. Colliding black holes: The close limit. *Phys. Rev. Lett.*, 72:3297–3300, May 1994.
- [170] C. V. Vishveshwara. Scattering of gravitational radiation by a schwarzschild black-hole. *Nature*, 227:936–938, 1970.
- [171] S. A. Teukolsky. Perturbations of a Rotating Black Hole. I. Fundamental Equations for Gravitational, Electromagnetic, and Neutrino-Field Perturbations. *Astrophysical J.*, 185:635–648, October 1973.
- [172] Fernando Echeverria. Gravitational-wave measurements of the mass and angular momentum of a black hole. *Phys. Rev. D*, 40:3194–3203, Nov 1989.
- [173] Hans-Peter Nollert. TOPICAL REVIEW: Quasinormal modes: the characteristic ‘sound’ of black holes and neutron stars. *Class. Quant. Grav.*, 16:R159–R216, 1999.

- [174] Jolien D. E. Creighton. Search techniques for gravitational waves from black-hole ringdowns. *Phys. Rev. D*, 60:022001, Jun 1999.
- [175] E. W. Leaver. An analytic representation for the quasi-normal modes of kerr black holes. *Proceedings of the Royal Society of London A: Mathematical, Physical and Engineering Sciences*, 402(1823):285–298, 1985.
- [176] M. Shahram and P. Milanfar. On the resolvability of sinusoids with nearby frequencies in the presence of noise. *IEEE Transactions on Signal Processing*, 53(7):2579–2588, July 2005.
- [177] P. Milanfar and A. Shakouri. A statistical analysis of diffraction-limited imaging. In *Image Processing. 2002. Proceedings. 2002 International Conference on*, volume 1, pages I–864–I–867 vol.1, 2002.
- [178] LIGO Scientific Collaboration, J. Aasi, B. P. Abbott, R. Abbott, T. Abbott, M. R. Abernathy, K. Ackley, C. Adams, T. Adams, P. Addesso, and et al. Advanced LIGO. *Classical and Quantum Gravity*, 32(7):074001, April 2015.
- [179] E. Berti, A. Sesana, E. Barausse, V. Cardoso, and K. Belczynski. Spectroscopy of Kerr black holes with Earth- and space-based interferometers. *ArXiv e-prints*, May 2016.
- [180] Harry L Van Trees. *Detection, estimation, and modulation theory*. John Wiley & Sons, 2004.
- [181] H. R. Beyer. On the Completeness of the Quasinormal Modes of the Pöschl-Teller Potential. *Communications in Mathematical Physics*, 204:397–423, 1999.
- [182] M. Ruiz, M. Alcubierre, D. Núñez, and R. Takahashi. Multiple expansions for energy and momenta carried by gravitational waves. *General Relativity and Gravitation*, 40:1705–1729, August 2008.
- [183] E. Berti and V. Cardoso. Quasinormal ringing of Kerr black holes: The excitation factors. *Phys. Rev. D*, 74(10):104020, November 2006.
- [184] E. Berti and A. Klein. Mixing of spherical and spheroidal modes in perturbed Kerr black holes. *Phys. Rev. D*, 90(6):064012, September 2014.
- [185] L. T. London, James Healy, and Deirdre Shoemaker. Erratum: Modeling ringdown: Beyond the fundamental quasinormal modes [phys. rev. d **90** , 124032 (2014)]. *Phys. Rev. D*, 94:069902, Sep 2016.

- [186] E. Berti, V. Cardoso, and C. M. Will. Gravitational-wave spectroscopy of massive black holes with the space interferometer LISA. *Phys. Rev. D*, 73(6):064030, March 2006.
- [187] Curt Cutler and Éanna E. Flanagan. Gravitational waves from merging compact binaries: How accurately can one extract the binary’s parameters from the inspiral waveform? *Phys. Rev. D*, 49:2658–2697, Mar 1994.
- [188] Lee S. Finn. Detection, measurement, and gravitational radiation. *Phys. Rev. D*, 46:5236–5249, Dec 1992.
- [189] O. Dreyer, B. Kelly, B. Krishnan, L. S. Finn, D. Garrison, and R. Lopez-Aleman. Black-hole spectroscopy: testing general relativity through gravitational-wave observations. *Classical and Quantum Gravity*, 21:787–803, February 2004.
- [190] E. Berti, V. Cardoso, J. A. Gonzalez, U. Sperhake, M. Hannam, S. Husa, and B. Brügmann. Inspiral, merger, and ringdown of unequal mass black hole binaries: A multipolar analysis. *Phys. Rev. D*, 76(6):064034, September 2007.
- [191] S. Gossan, J. Veitch, and B. S. Sathyaprakash. Bayesian model selection for testing the no-hair theorem with black hole ringdowns. *Phys. Rev. D*, 85:124056, Jun 2012.
- [192] M. Vallisneri. Use and abuse of the Fisher information matrix in the assessment of gravitational-wave parameter-estimation prospects. *Phys. Rev. D*, 77(4):042001, February 2008.
- [193] Liming Xiang. A review of: introduction to bayesian statistics. *IIE Transactions*, 39(8):829–829, 2007.
- [194] Andrew Gelman, John Carlin, Hal Stern, David Dunson, Aki Vehtari, and Donald Rubin. *Bayesian Data Analysis, Third Edition (Chapman & Hall/CRC Texts in Statistical Science)*. Chapman and Hall/CRC, London, third edition, November 2014.
- [195] William G. Cochran. *Sampling Techniques, 3rd Edition*. John Wiley, 1977.
- [196] Don van Ravenzwaaij, Pete Cassey, and Scott D. Brown. A simple introduction to markov chain monte-carlo sampling. *Psychonomic Bulletin & Review*, 25(1):143–154, Feb 2018.
- [197] D. W. Hogg and D. Foreman-Mackey. Data Analysis Recipes: Using Markov Chain Monte Carlo. , 236:11, May 2018.

- [198] James M. Flegal, Murali Haran, and Galin L. Jones. Markov chain monte carlo: Can we trust the third significant figure? *Statist. Sci.*, 23(2):250–260, 05 2008.
- [199] L. T. London. Modeling ringdown II: non-precessing binary black holes. *ArXiv e-prints*, January 2018.
- [200] M. Boyle. How should spin-weighted spherical functions be defined? *Journal of Mathematical Physics*, 57(9):092504, September 2016.
- [201] B. P. Abbott, R. Abbott, T. D. Abbott, M. R. Abernathy, F. Acernese, K. Ackley, C. Adams, T. Adams, P. Addesso, R. X. Adhikari, and et al. Localization and Broadband Follow-up of the Gravitational-wave Transient GW150914. *Astrophysical J.*, 826:L13, July 2016.
- [202] Siddhartha Chib and Edward Greenberg. Understanding the metropolis-hastings algorithm. *The American Statistician*, 49(4):327–335, 1995.
- [203] J.F Plebanski and M Demianski. Rotating, charged, and uniformly accelerating mass in general relativity. *Annals of Physics*, 98(1):98 – 127, 1976.
- [204] Alikram N. Aliev, Hakan Cebeci, and Tekin Dereli. Kerr-taub-nut spacetime with maxwell and dilaton fields. *Phys. Rev. D*, 77:124022, Jun 2008.
- [205] J. B. Griffiths and Jiri Podolsky. Accelerating and rotating black holes. *Class. Quant. Grav.*, 22:3467–3480, 2005.

Curriculum Vitae

Title of Dissertation

Towards Probing The Strong Field Gravity With Black Hole Ringdown.

Full Name

Swetha Bhagwat

Place and Date of Birth

Karnataka, India

May 28, 1991

Colleges and Universities,

IISER- Pune

Syracuse University

Years attended and degrees

2008–2013, B.S. - M.S.

2013–2019, Ph.D.

Major Department

Physics